2003

# Electron paramagnetic resonance and optical studies of chromium-doped cadmium-gallium-sulfur.

Melinda Frances Byrd Johnson
*University of Alabama at Birmingham*

# NOTE TO USERS

Duplicate page number(s); text follows.

The manuscript was scanned as received.

101-102

This reproduction is the best copy available.

UMI®

# ELECTRON PARAMAGNETIC RESONANCE AND OPTICAL STUDIES OF $CdGa_2S_4:Cr^{++}$

by

MELINDA BYRD JOHNSON

A DISSERTATION

Submitted to the graduate faculty of The University of Alabama at Birmingham,
in partial fulfillment of the requirements for the degree of
Doctor of Philosophy

BIRMINGHAM, ALABAMA

2003

ABSTRACT OF DISSERTATION
GRADUATE SCHOOL, UNIVERSITY OF ALABAMA AT BIRMINGHAM

Degree Ph.D. Program Physics

Name of Candidate Melinda Byrd Johnson

Committee Chair Mary Ellen Zvanut

Title Electron Paramagnetic Resonance and Optical Studies of $CdGa_2S_4$:Cr

Solid state lasers are often based on paramagnetic ions that are imbedded in a crystal host. Recently work has focused on utilizing transition metal ions, particularly chromium, to create a laser capable of emitting light in the middle infrared wavelengths. We investigated crystals of chromium doped $CdGa_2S_4$ with X-ray diffraction (XRD), energy dispersive X-ray spectroscopy (EDXS), electron paramagnetic resonance (EPR), optically induced EPR, absorption and photoluminescnence (PL) measurements to characterize the crystals.

## DEDICATION

I dedicate this dissertation to Jesus Christ, through whom all things are possible.

ACKNOWLEDGEMENTS

The first acknowledgement goes to my mother, Frances Byrd Currie. She provided not only enormous amounts of emotional support but also vast amounts of support to keep my life running. She made time to pick up Matthew from school, sit with him when he was ill, and babysit Emily. I could not have finished this degree without her. She has always provided a gentle guidance. My family, of course, deserves a huge thanks for staying with me through all the many years. David has gone through all the bad and good times with me. I appreciate the love that he provides. Matt has grown from stating that his Mom was "getting a Masterate," to understanding there are both a Masters and a Doctorate degree. Emily is too little to understand but will explain that all good things, such as the circus, reside in Birmingham when they are not in Decatur. My sister, Adair, gets thanks for helping with babysitting and providing technical writing for the dissertation.

I consider myself lucky to have attended a department filled with so many pleasant and talented people. Dr. Zvanut, of course, gets much acknowledgement. She has been infinitely patient and supportive. I realize that it was difficult to work with me as a graduate student. Not only did I live an hour and a half away, but I started with one child and ended with two. She deserves much credit for the long telephone calls, emails, and general ability to work with people. She is an excellent advisor.

Dr. Mirov has also been a wonderful mentor in guiding me through the optics portion of this work. Dr. Mirov is always enthusiastic and an impressive physicist. Dr.

Harrison has been very helpful in talking to me about the theoretical aspects of the work. I must also take time to acknowledge Dr. Wills, who guided me through the process of achieving a Masters degree. Jerry Sewell, who keeps all things in the department working, receives many thanks for helping me to keep my equipment running and for building whatever apparatus I needed for the experiments.

TABLE OF CONTENTS

*Page*

ABSTRACT ..... ii

DEDICATION ..... iii

ACKNOWLEDGEMENTS ..... iv

LIST OF TABLES ..... ix

LIST OF FIGURES ..... x

LIST OF ABBREVIATIONS ..... xii

CHAPTER

1 INTRODUCTION ..... 1

2 EXPERIMENTAL DETAILS ..... 9

A. EDXS ..... 9
B. XRD ..... 11
C. EPR ..... 12
D. Absorption and Fluorescence ..... 14

3 SAMPLE CHARACTERIZATION ..... 16

A. XRD ..... 16
B. EDXS ..... 20

4 EPR ..... 25

A. EPR of noninteracting centers ..... 27
1. EPR of defects ..... 27
2. EPR of shallow effective mass acceptors ..... 30
B. EPR of exchange coupled system ..... 31
1. Exchange Interaction ..... 33
2. Exchange Hamiltonian ..... 35
3. Effects of exchange interactions on EPR spectra ..... 36
4. Exchange narrowing ..... 38

5. Temperature effects on exchange spectra ..... 43

TABLE OF CONTENTS (Continued)

CHAPTER *Page*

C. EPR of results ..... 44
1. $CdGa_2S_4$ and $CdGa_2S_4$:Cr EPR spectra ..... 44
2. Angular variation of $CdGa_2S_4$ and $CdGa_2S_4$:Cr EPR spectra rotated about (1,1,2) ..... 46
3. Angular variation of $CdGa_2S_4$:Cr EPR spectra rotated about different axis ..... 49
4. Angular dependence of line width of $CdGa_2S_4$:Cr EPR spectra ..... 51
5. Line shape analysis of $CdGa_2S_4$:Cr EPR spectra ..... 52
6. Line shape analysis of $CdGa_2S_4$:Cr EPR spectra ..... 53
7. Temperature dependence of $CdGa_2S_4$:Cr EPR spectra ..... 53
8. Signal Intensity ..... 58
D. Discussion ..... 59

5 OPTICAL INTERACTIONS ..... 63

A. Absorption mechanisms ..... 64
1. Crystal lattice vibrations ..... 64
2. Vibronic, direct, and indirect transitions ..... 65
3. Donors and Acceptors ..... 68
4. DA pairs ..... 69
5. Transition metal dopant atoms ..... 70
6. Polarized absorption ..... 74
B. Luminescence of solids ..... 74
C. Exchange systems in absorption and luminescence ..... 75
D. Experimental results ..... 77
1. Absorption ..... 77
2. Polarized absorption ..... 84
3. PL ..... 84
E. Discussion ..... 89

6 SUMMARY ..... 91

7 FUTURE WORK ..... 95

LIST OF REFERENCES ..... 97

APPENDIX

A ANALYSIS OF EPR RESONANCE LINE SHAPE ..... 101
B CALIBRATION OF FLUORESCENCE INSTRUMENT ..... 107

LIST OF TABLES

*Table* *Page*

1 Sample description.....10

2 Crystal orientations in tetragonal Miller coordinates.....21

3 EDXS results for $Cd_wGa_xS_y:Cr_z$.....23

4 Relative number of centers in EPR resonance.....58

5 Relative number of centers in EPR resonance and absorption coefficient. .....94

LIST OF FIGURES


*Figure* *Page*

1 CdGa2S4 unit cell. Cadmium is the largest sphere (salmon), sulfur is the smallest sphere (yellow), and gallium is the medium sphere (green). ..... 5

2 Proposed energy structure of doped CdGa2S4. This structure was based on TSL, TSC and Hall effect measurements [22]. ..... 6

3 Typical sample dimensions. ..... 9

4 XRD experiment. ..... 11

5 Two theta XRD data for unpolished face of crystal K4A. ..... 18

6 Omega-rocking scan XRD data for the diffraction peak of (2,2,0) on the unpolished face of crystal K4A. ..... 19

7 Energy diagram for weak and strong exchange limits. The energy of the applied microwave radiation in the EPR experiment is hv. ..... 37

9 EPR first derivative spectra at 12 Kof (a) undoped CdGa2S4, (b) un-annealed CdGa2S4:Cr from Kuban State University, (c) unannealed CdGa2S4:Cr from The BAE Corporation, (d) and annealed CdGa2S4:Cr. ..... 45

11 Zero crossings of a CdGa2S4:Cr crystal from BAE Corporation rotated about the (3,2,3) axis. Angles are from the (3,-1,6) – 300 ..... 49

12 Zero crossings of CdGa2S4:Cr crystal K4 rotated about the (2,2,-7) axis. Angles are from the (1,-1,4) – 750. ..... 50

13 Zero crossings of a CdGa2S4:Cr crystal K4 rotated about the (0,0,1) axes. Angles are from the (1,-1,0) - 750. ..... 51

14 EPR resonance line width variation with angle about rotation axis (1,1,2) for crystal K4A. ..... 52

15 EPR resonance spectra at (a) 200 K, (b) 150 K, (c) 100 K, (d) 50 K. (e) 20 K, and (f) 12 K normalized for Boltzmann factor to 12 K for crystal K4. ..... 54

*Figure* *Page*

16 Intensity of EPR signal determined by double integration of first derivative spectra Boltzmann normalized to 12 K for CdGa2S4:Cr crystal K4. The g=3 center is denoted by •, and the g=6 center is denoted by ▲. ....55

17 Temperature dependence of the ratio of resonance intensity for unannealed CdGa2S4:Cr. ....56

18 EPR spectra at 12K (a), and 4K (b) for crystal K4 rotated about (1,1,2) axis. ....57

19 Idealized vibronic fluorescence of a crystal with phonon energy of p. ....66

20 Direct and indirect transitions between the conduction and valence bands of a crystal. ....67

21 Octohedral symmetry. Dopant atom is black oval. Host ions are unfilled ovals. ....72

22 Absorption of CdGa2S4:Cr crystal K3A in unpolarized light. ....78

23 Tanabe-Sugano diagram for d6 ions in an octahedral environment, or d4 ions in a tetrahedral environment. ....81

24 Tanabe-Sugano diagram for d7 ions in an octahedral environment, or d3 ions in a tetrahedral environment. ....82

25 CdGa2S4:Cr crystal K3A unpolarized absorption. ....83

26 Absorption of (a) CdGa2S4:Cr and (b) CdGa2S4 in light linearly polarized in the (1,-1,0) direction. ....85

27 Absorption of (a) CdGa2S4:Cr and (b) CdGa2S4 in light linearly polarized in the (1,1,2) direction. ....85

28 Polarized absorption of band centered at 1288 nm in CdGa2S4:Cr and CdGa2S4. ....86

30 PL of CdGa2S4:Cr with excitation of 2500 nm and with a diffraction grating of 150 grooves /mm at 77 K. ....87

31 Fluorescence at 605nmof CdGa2S4:Cr at 77K. ....88

## LIST OF ABBREVIATIONS

| | |
|---|---|
| EPR | Electron paramagnetic resonance |
| IR | Infrared |
| PL | Photoluminescence |
| ODP | Ordered defect pairs |
| ODC | Ordered defect compound |
| DA | donor acceptor |
| TSL | Thermally stimulated luminescence |
| TSC | Thermally stimulated conductivity |
| EDXS | Energy dispersive X-ray spectroscopy |
| XRD | X-ray Diffraction |
| mid IR | Middle infrared |
| FWHM | Full width at half maximum |

# CHAPTER 1

## INTRODUCTION

In 1960 Theodore Maiman created the first laser using a ruby crystal. The ruby laser system is based on paramagnetic chromium ions, $Cr^{3+}$, imbedded in an $Al_2O_3$ crystal matrix. When a dopant ion is incorporated into a lattice site, the energy levels of the dopant ion depend on the site symmetry and which type of atoms surround the dopant ion. Ruby crystals were investigated with Electron Paramagnetic Resonance (EPR) to determine the site symmetry and ground level spin state prior to the creation of the laser. Ruby was anticipated to be a useful compound for a three level solid state maser. After EPR determined chromium in $Al_2O_3$ has a spin state of 3/2 and a symmetry condition of $C_3$, Theodore Maiman used absorption experiments to confirmed the energy levels of chromium in $Al_2O_3$ could be used for a three level laser system [1]. Since the creation of the ruby laser scientists and engineers have created lasers by using dyes, gasses, and semiconductor p-n junctions. While these other types of media have greatly extended the range of wavelengths available and the ability to move the laser, solid state lasers based on doped crystals, such as the Nd:YAG, are capable of yielding better spatial beam profile, better beam quality, and sometimes higher power than other types of lasers. An interesting hybrid that has developed is a diode pumped solid state laser. Recently, work has been done with transition metal ions in chalcogenides that demonstrates the suitability of these crystals for generating middle infrared (mid IR) laser wavelengths at room temperature [2-5].

The mid IR wavelength range is generally considered to consist of radiation with wavelengths on the order of 1 to 10 μm. In this region there exist several ranges of wavelengths that are not absorbed by water or carbon dioxide. Often these ranges are referred to as optical windows. A few of these windows are 1.5-1.75 μm, 2-2.4 μm, 3.4-4.2 μm, 4.6-4.8 μm, 8-13 μm, and 16-18 μm [6]. Solid state lasers that can operate in an optical window would have many commercial applications. Defense applications would include infrared (IR) countermeasures. Industrial applications of mid IR lasers may include the creation of sensors offering better control of solution strengths during manufacturing processes, as well as more accurate and economical methods of monitoring environmental contamination levels in steam and wastewater from manufacturing plant environments.

Laser materials have been investigated by correlating optical and paramagnetic resonance data since the early 1960s. Comparing optical absorption data with EPR measurements may allow an optical absorption band to be assigned to specific defects within the material. By using a standard to determine the number of defects in the sample, it is also possible to determine lifetime and quantum efficiency of the absorption band as a function of the number of defects within the sample [7]. Scientists may use this type of data to optimize solid state laser designs.

Most of the undoped III-V and II-VI semiconductors were characterized by using optical and EPR techniques in the 1960s, when many of the absorption bands were assigned to defects [8]. There is still work to be done with effects of dopants in these III-V and II-VI materials, and current research is addressing these issues. For example, in

1994 Dziesiaty, and coworkers, by using EPR and optical data, associated Ti+ with absorption bands at 2.76 μm, 2.22 μm, 2.00 μm, and 0.77 μm in ZnSe:Ti [9].

Although most of the research on doped chalcogenides has involved the binary II-VI semiconductors such as ZnS, doped ternary chalcogenides show much potential for providing room temperature mid-IR gain media for lasers. The ternary chalcogenides are compounds that contain three different types of atoms, one of which is from column VI in the periodic chart. These compounds have defects that have been detected by EPR, and these defects have been linked to specific absorption bands. By comparing EPR and optical absorption, Kaufman associated the $Ni^{+}$ dopant to absorption bands near 1.93 μm in $AgGaS_2$ [10]. Haliburton and Giles have shown that $Ni^{+}$ causes room temperature absorption near 2.2 μm in $AgGaSe_2$ [11]. Teranishi and coworkers have linked $Fe^{3+}$ dopant in $CuGaS_2$ to absorption bands near 0.16 μm and 0.10 μm [12]. H. Von Bardeleben and coauthors have demonstrated that $Fe^{2+}$ in $AgGaS_2$ is associated with an absorption band at 5 μm and that $Fe^{3+}$ is related to one at 0.8 μm [13].

Chalcopyrites, substances having the general formula I-III-$VI_2$ or II-IV-$V_2$ ($ABC_2$), are ternary chalcogenides. Chalcopyrites have a very precise arrangement of atoms wherein each A and B atom is tetrahedrally bonded to the four C atoms and the C atom is tetrahedrally bonded to two A and two B atoms in an ordered manner. It has been shown that ternary chalcopyrites generally have high levels of defects. In the chalcopyrite $CuInSe_2$, it has been theoretically shown that this high number of defects is tolerated through the spontaneous formation of defect pairs, which exist as ordered defect pairs (ODP), and defect pair arrays [14]. Essentially these ODP exist in a "supercell", that consists of four to nine unit cells of $CuInSe_2$. The supercell is repeated through the

material in the same manner as the conventional unit cell. By utilizing ODP it is possible to predict several deviances in stoichiometry for $CuInSe_2$. These compounds with stoichiometric deviations are referred to as ordered defect compounds (ODC). Utilizing ODP several unusual properties of $CuInSe_2$ may be explained: (1) tolerances to stoichiometric deviations, (2) the ability to change properties by self doping the material, and (3) the electrically benign nature of the defects [15].

Another example of ternary chalcogenides is the defect chalcopyrites, or thiogallates, if the materials contain gallium and sulfur. The defect chalcopyrites, illustrated in Fig. 1, also have tetrahedrally coordinated atoms that follow the general formula II-$III_2$-$VI_4$ ($AB_2C_4$), where the A and B atoms bond to four C atoms and the C atoms bond to two B atoms and one A atom. The defect chalcopyrite material essentially has a chalcopyrite structure with an ordered vacancy for a quarter of the B cations. The space group for defect chalcopyrites is $S_4$. These materials also show the same promise as the chalcopyrites for providing room temperature mid IR semiconductor lasers.

$CdGa_2S_4$ is the defect chalcopyrite being studied in the current work. This compound should be colorless but is mostly reported to be slightly yellow. Generally the color is attributed to deviations from stoichiometry, particularly by increased gallium [16]. In this compound gallium is the only atom with two nonequivalent positions, and the sulfur atom has a coordination number of 3. The crystal lattice parameters are a=5.56Å, c=10.05Å [17]. The interatomic distances for the two inequivalent gallium sites have bond lengths of 2.33 Å and 2.25 Å. The Cd-S distance of 2.52 Å is the largest. Calculation of bond ionicity has shown that the Cd-S bond is significantly more covalent than the Ga-S bond [17]. The X-ray K spectrum of the sulfur in $CdGa_2S_4$ is consistent with a Dirac–Hara energy dependent exchange energy [18].

The band gap of $CdGa_2S_4$ is approximately 3.4 eV [19]. Measurements of the Hall mobility of carriers versus temperature have determined the compound has a high

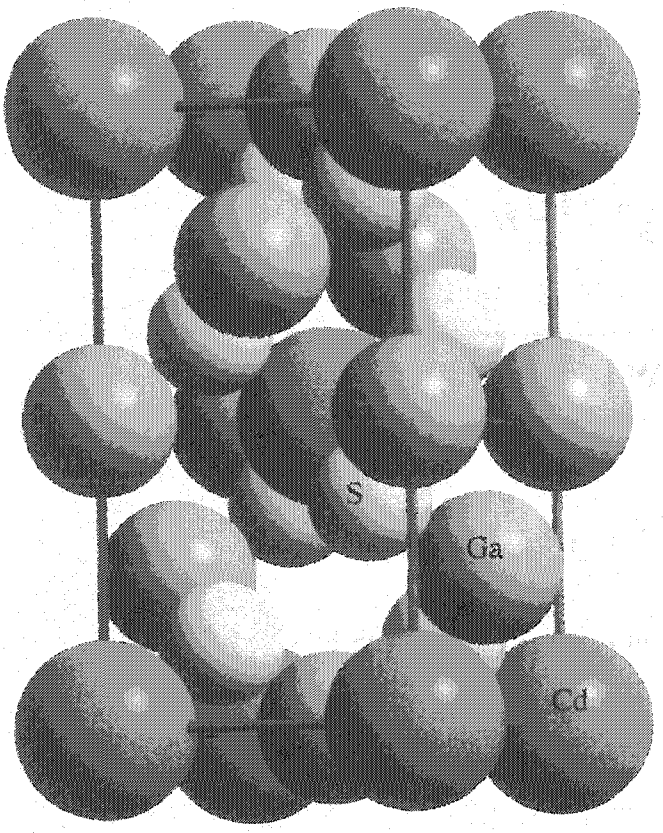


FIG. 1. $CdGa_2S_4$ unit cell. Cadmium is the largest sphere (salmon), sulfur is the smallest sphere (yellow), and gallium is the medium sphere (green).

native defect concentration (about $10^{-21}$ $cm^{-3}$ or 2.5 mole percent) [20]. The majority of the centers found were believed to be ionized native defects, which exist as compensated donor–acceptor (DA) pairs. Only 10% of the centers are believed to exist as dipoles or neutral centers [20]. Two electron traps, which are both thermally emptied at 200 K, have been found at 0.55 and 0.65 eV below the conduction band. Photoconductivity measurements showed both of the traps have broadly distributed energy levels. Some of the results from thermally stimulated luminescence (TSL) and thermally stimulated

conductivity (TSC) measurements required an assumption of a continuous distribution of trapping levels [21].

Studies of $CdGa_2S_4$, $CdGa_2S_4$:In, and $CdGa_2S_4$:Ag have suggested the energy diagram in Fig. 2. TSL, TSC, and PL studies of $CdGa_2S_4$ doped with an acceptor, Ag, and a donor, In, showed these dopants formed short range complexes with the native defects. The fluorescence of $CdGa_2S_4$:Ag was essentially the same as undoped $CdGa_2S_4$ [21]. Thus, fluorescence of $CdGa_2S_4$:Ag is dominated by native defects. The energy diagram of $CdGa_2S_4$:In, and $CdGa_2S_4$:Ag, is essentially the same as the energy diagram for $CdGa_2S_4$ with additional donor and acceptor levels [22].

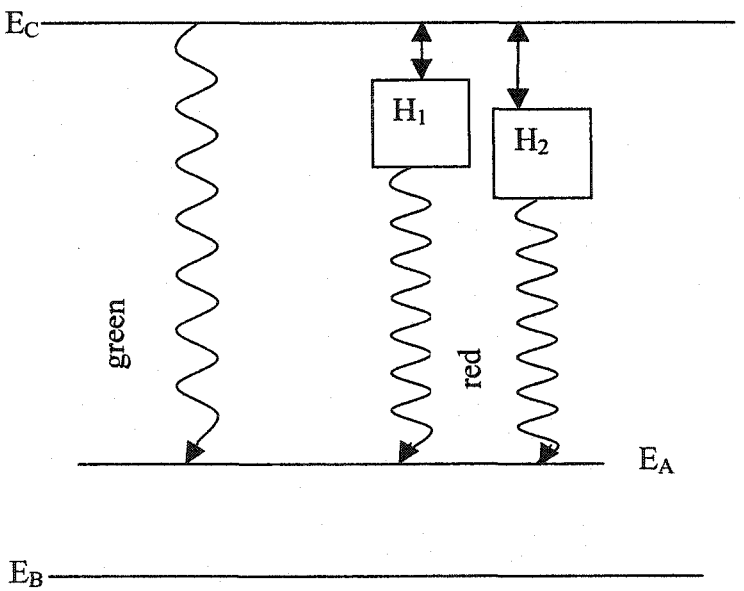


FIG. 2. Proposed energy structure of doped $CdGa_2S_4$. This structure was based on TSL, TSC and Hall effect measurements [22].

$CdGa_2S_4$ has a wide region of transparency, from 450 to 13,000 nm, and it is a nonlinear optical material with a large nonlinear coefficient [23]. However, the birefringence is very small, $\Delta n \approx 0.006$ for light of wavelength 450-487 nm [24]. For light

of 490 nm the birefringence changes sign. A crystal field splitting of 3640 $cm^{-1}$ has been estimated for $CdGa_2S_4:Co^{2+}$ through absorption studies [25].

Several authors have reported luminescence from undoped and doped $CdGa_2S_4$. After being excited with light at 365 nm or 425 nm, $CdGa_2S_4$ emitted red light with wavelength 620 nm at low temperature (80 K). The emitted light changed to yellow-green light with wavelength 563 nm upon heating to 360 K. Both bands were broad and did not contain phonon structure. When the same excitation was used on $CdGa_2S_4$:Ag, red luminescence was observed and the green band was absent [21]. $CdGa_2S_4$ :In emitted at higher wavelengths (650 nm) after excitation with 365 nm or 425 nm light and showed a peak in luminescence at 118 K [21]. Additional studies showed blue luminescence, probably caused by interstitial cadmium, consisting of two bands at 450 nm and 425 nm [26].

$CdGa_2S_4$ has previously been investigated in a limited capacity. There are not many articles to reference about the material. The change of sign in birefringence has led to some optical investigation, but no absorption data have been reported for 2.5 μ. To my knowledge, $CdGa_2S_4$ has not been investigated with electron paramagnetic resonance (EPR). There are no reported data on $CdGa_2S_4$:Cr. In order to extend the knowledge of the defect chalcopyrite $CdGa_2S_4$:Cr and characterize the samples, energy dispersive X-ray spectroscopy (EDXS), X-ray diffraction (XRD), optical absorption, PL, and EPR were used to investigate the samples.

This dissertation will discuss the samples used for the investigation and the details of the experiments in Chapter 2. Chapter 3 will review XRD and EDXS characterization of the crystal samples. Chapter 4 will discuss EPR theory and the results of the EPR experiments. Chapter 5 will focus on optical interactions of the crystals and the results of

absorption and PL experiments on $CdGa_2S_4$:Cr. Chapter 6 will summarize the experimental results. Chapter 7 is a discussion of work that would benefit future research in this field.

# CHAPTER 2

## EXPERIMENTAL DETAILS

This chapter will discuss the experimental details used to investigate the crystals. Samples of $CdGa_2S_4$ (1) and $CdGa_2S_4$:Cr (6) were obtained from Kuban State University in Russia and The BAE Corporation. Samples were doped during growth. Two of the doped samples were annealed. Two samples were annealed at 900 K for 12 hours. The rest of the samples were unannealed. All samples had one face optically polished. Sample color varied from pale yellow to topaz. Table 1 summarizes the characteristics noted in the crystals and assigns designations for each crystal. Figure 3 illustrates a typical sample.

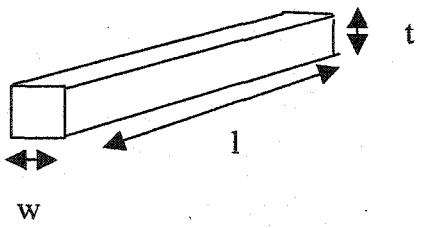


FIG. 3. Typical sample dimensions.

### A. EDXS

A JEOL-820 scanning electron microscope is used to provide X-ray radiation for the EDXS experiments. A Kevex detector system interfaced to a Macintosh computer was used for the EDXS measurements. The software contained information for doing a

TABLE 1 Sample description; *assumes a density of $10^{22}$ atoms/cm$^{-3}$.

| Manufacturer | Name | Size (mm) lXtXw | Color | *Cr doping in melt ($10^{19}$atoms/cm$^3$) | Anneal |
|---|---|---|---|---|---|
| Kuban State | K1 | 7X4X2 | Topaz | 6.0 | None |
| Kuban State | K2 | 9X7X3 | Topaz | 6.0 | None |
| Kuban State | K3A | 9X4X2 | Pale yellow | 6.0 | 12 h in vacuum at 900 K |
| Kuban State | KUn | 10X5X1 | Pale yellow | None | None |
| Kuban State | K4 | 10X5X1 | Pale yellow | <6.0 | None |
| Kuban State | K4A | 10X5X1 | Pale yellow | <6.0 | 12 h in vacuum at 900 K |
| Kuban State | K5 | 13X4X4 | Pale yellow | <6.0 | None |
| Kuban State | K6 | 10X4X4 | Pale yellow | <6.0 | None |
| Kuban State | K7 | 13X4X4 | Pale yellow | <6.0 | None |
| BAE | B1 | 5X5X3 | Pale yellow | 1.0 | None |
| BAE | B2 | 5X5X3 | Pale yellow | None | None |

standardless analysis. Peaks were seen consistent with the L shells of Ga and Cd, as well as the K shell of S. Samples K1 and K2 appeared to have a small peak consistent with the Cr K shell. These two samples were analyzed for composition both with and without Cr being included. The spot size was approximately 5X4 $\mu m^2$. The maximum acceleration voltage for this machine is 30 KeV. A working voltage of 20 KeV was used for all samples.

B. XRD

A Phillips X'PERT MPD system was used to conduct the XRD investigations. The output radiation was from a Cu anode that provided X-rays with wavelength of 0.154184 nm. Figure 4 illustrates the experimental setup for a XRD scan. The angle between the incident X-rays and the sample is theta. The angle between the sample and the detector is omega. Sample faces were determined with XRD using two types of scans, two theta and omega-rocking scans. Two theta scans have equal angles for theta and omega. In omega-rocking scans, theta is set to a constant value and omega is varied. By using omega-rocking scans it is possible to determine whether the crystal planes

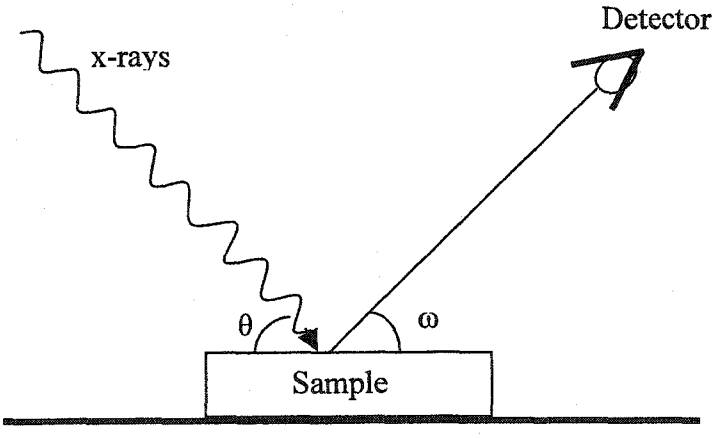


FIG. 4. XRD experiment.

are at an angle to the cut face of the crystal. A crystal cut exactly on a crystal plane will have an XRD peak in the omega-rocking scan at the angle theta determined from the two theta scan. When the crystal is cut at an angle alpha with respect to the plane determined by the diffraction peak, the omega-rocking scan diffraction peak will be at angle equal to omega plus alpha.

Because the stage is flat and the samples are mounted with double-sided tape, only small deviations on the order of 0.1° could be attributed to experimental error in sample mounting. The width of the omega-rocking scan peaks can be used to determine the crystalline quality of the material.

## C. EPR

A Bruker 200 X-band (9.6 GHz) spectrometer was used to conduct the EPR experiments. This system is equipped with a Varian model 3609 electromagnet, which is capable of supplying magnetic fields from 0.1 to 10,000 G. In practice the magnet overheats at high magnetic fields, so the scans used 7,500 G as the upper limit.

Phase sensitive detection is utilized to increase the signal to noise ratio. In phase sensitive detection the applied magnetic field is modulated. The detector and amplifier are locked onto the modulation frequency and only amplify this portion of the signal. The first Fourier harmonic of the magnetic field contains the EPR signal; therefore, the signal observed in this system is the first derivative of the EPR absorption spectra. The actual resonance signal will occur at the zero crossing of the first derivative resonance absorption. A g value of the zero crossing is obtained by dividing the energy of the microwave radiation, hν, by the value of the magnetic field at the zero crossing point $B_0$ and $\beta_e$, where h is the Planck constant and $\beta_e$ is the Bohr magneton.

The total number of centers represented by a resonance line can be determined by comparison with a known standard. Silicon doped with phosphorus to a resistivity level of 0.014 ohm-cm in an amount equal to 25.9 mg was used as a standard. A double integral of the first derivative resonance line for the known sample was performed to find the total intensity of the signal. The total intensity of the known signal at 13 K

corresponds to 5.18 $10^{15}$ centers. A ratio between the total intensities of the sample and known resonances can be found by performing a double integral on resonance peaks in an EPR spectra. The ratio of the sample and known signal intensity is multiplied by the number of centers in the sample to give us the number of centers contained in the EPR signal.

In general, the symmetry of the defect may be determined by rotating the sample about three different fixed axes. The EPR system contains a goniometer attached to the central rod where samples are affixed. The samples may be rotated on this central rod and the angle of rotation calculated from the difference between the initial angle, usually with the magnetic field parallel to a crystal face, and the angle after rotation.

Low temperature EPR experiments utilized either an Air Products closed cycle helium refrigerator connected to a Lakeshore temperature controller or an Oxford Instruments ESR 900 cryostat unit. In the closed cycle system the samples were mounted on a copper rod. The copper rod had been tested and did not give any EPR signals. In the Oxford Instruments liquid helium system, the samples were mounted in a quartz tube. The quartz tube was found to produce an EPR signal, which is identified in the EPR chapter. Next the samples were placed in the EPR cavity. For the measurements of the crystals from Kuban State a rectangular cavity was used; for the EPR measurements of the crystals from BAE a cylindrical cavity was used.

As the temperature is changed the number of centers in the excited state will change according to Boltzmann statistics. The total number of centers is compared to determine whether the number of centers changes with temperature. To compare intensity of resonances from different temperatures, the intensity changes from the Boltzmann statistics must first be normalized to a single temperature. By expanding the

Boltzmann equation about temperature, T, the temperature change because of the Boltzmann statistics can be approximated as $T^{-1}$. The EPR spectra are Boltzmann normalized by dividing the experimental temperature by the normalization temperature and multiplying the spectrum by this constant. For example, a spectrum taken at 200K would be Boltzmann normalized to 12 K by multiplication of the constant equal to 200/12.

It was noted early in the present study that EPR centers varied over time. This variation was most likely caused by exposure to heat and light. An IR lamp was used to dry the mounting glue. In all the EPR spectra reported the EPR cavity was covered to provide a dark environment for a minimum of 12 hours. This procedure was found to remove any EPR centers from exposure to the heat lamp. The samples were not always completely covered during measurement. A GaN light emitting device of 380 nm wavelength provided excitation for the EPR spectra.

### D. Absorption and Fluorescence

The spectra were taken with a Shimadzu spectrophotometer as a percentage of transmission of light intensity. The transmission data were converted to absorption by the computer. The Bouger-Lambert-Beer law of absorption relates the optical density, $D$, to the ratio of the measured transmitted intensity of the light, $I$, to the initial intensity of the incident light, $I_0$ [27].

$$D = \log_{10}(I/I_0). \tag{1}$$

The Shimadzu spectrophotometer splits the beam of light into two beams of equal intensity, one of which is then used as a reference beam to provide the incident intensity. The

macroscopic quantity generally reported for absorption is the absorption coefficient, $\alpha$, which is related to the beam intensity and length of the crystal, $l$, through an exponential [28].

$$I = I_0 \exp(\alpha l) . \quad (2)$$

To report the data in these units the raw data must be multiplied by a constant, C, equal to

$$C = \ln(10)/l . \quad (3)$$

A Melles Griot linear polarizer, model number 03-FPI-005, was used to analyze the polarization of absorption in the 500 to 2,500 nm range.

PL measurements were attempted in both the visible and IR regions of the electromagnetic spectrum. PL measurements utilized a SpectraPhysics JCR230 Nd:yttrium aluminum garnet Laser for excitation at 354 nm, a 300 mW Erbium diode laser for excitation at 1500 nm, a 50 mW $ZnS:Cr^{2+}$ laser for excitation at 2.5 μ, and a frequency doubled LiF $F^{2+}$ Color center laser for excitation at 450 nm. Detection of fluorescence used the 0.75 m and 0.3 m nitrogen purged Acton Research "SpectraPro" spectrometer and thermo-electrically cooled PbS or a liquid nitrogen cooled InSb fast (0.7 μs) detector. When the fluorescence peak is very small there is not much change in the instrument's efficiency over the spectral region. However, as will be demonstrated later, $CdGa_2S_4$:Cr fluoresces over a large region. Appendix B describes how to calibrate the instrument so that the data reported do not represent changes in the instrument's efficiency across the spectral range of the fluorescence.

# CHAPTER 3

## SAMPLE CHARACTERIZATION

This chapter will discuss XRD and EDXS techniques used to characterize the sample. XRD was primarily used to orient the crystals for EPR analysis. EDXS was performed to study the uniformity of crystal stoichiometry.

### A. XRD

For a two-dimensional treatment of solids the Bragg diffraction law [29],

$$n\lambda = 2d\sin\Theta, \tag{4}$$

is sufficient for determining where the constructive interference peaks will occur. The distance, $d$, in the Bragg law written in terms the Miller indices ($h$, $k$, $l$) for a tetragonal crystal is

$$d = \frac{a}{\sqrt{\left(h^2 + k^2 + \left(la/c\right)^2\right)}}. \tag{5}$$

Miller indices are related to the crystal through a reciprocal relationship. For a crystal with axes of length ($a$, $b$, $c$) the plane with the Miller indices ($h$, $k$, $l$) will intercept the axis of a crystal at ($a/h$, $b/k$, $c/l$). Tetragonal crystals have three right angle axes, two of the same length, $a$, and one of unequal length, $c$. Once the angle of diffraction and the length of a crystal's axis are known, the Miller indices associated with the diffraction peak can be determined. Because the distance depends on the square of the Miller indices, there is an uncertainty in the sign of the Miller indices associated with crystal

faces determined from XRD. Not all planes will have a diffraction peak associated with XRD. Certain combinations of Miller indices yield destructive interference. A structure factor may be calculated for crystals to determine which planes yield constructive interference and therefore diffract X-rays. For $CdGa_2S_4$ the condition for constructive interference is that

$$h+k+l=2n, \tag{6}$$

for n=integer [30]. This interference equation means that if the Miller indices of a plane do not sum to an even number, $CdGa_2S_4$ will not have a diffraction peak for the plane. All planes reported in this dissertation are Miller indices for the tetragonal $CdGa_2S_4$ system.

The two theta scan is often used in XRD to determine the Miller indices of a crystal with unknown orientation. The two theta values were varied from 10° to 80° to search for diffraction peaks in the samples. The angular values for the diffraction peaks were compared with the Miller planes determined by Hahn and coworkers [31]. Figure 5 is a two theta scan performed on crystal K4A, a doped, annealed sample from Kuban State. The stage used in XRD analysis was found to contribute peaks to some of the spectra because of the diffraction of the aluminum stage. These peaks are labeled with (Al) on the graph.

For samples from Kuban State that were EPR active, an omega rocking curve was also performed. Figure 6 shows the omega-rocking scan for crystal K4A that corresponds to the diffraction peaks shown in the two theta scan of 46.2°. From reference sources it can be determined that a two theta value of 46.2° corresponds to the Miller indices (2,2,0). If crystal K4A is cut directly on the (2,2,0) plane, it is expected that the

omega scan will peak at 23.1°. The omega scan peaks at approximately 23.5°, which means the crystal face is cut at an angle of 0.4° from the (2,2,0) plane.

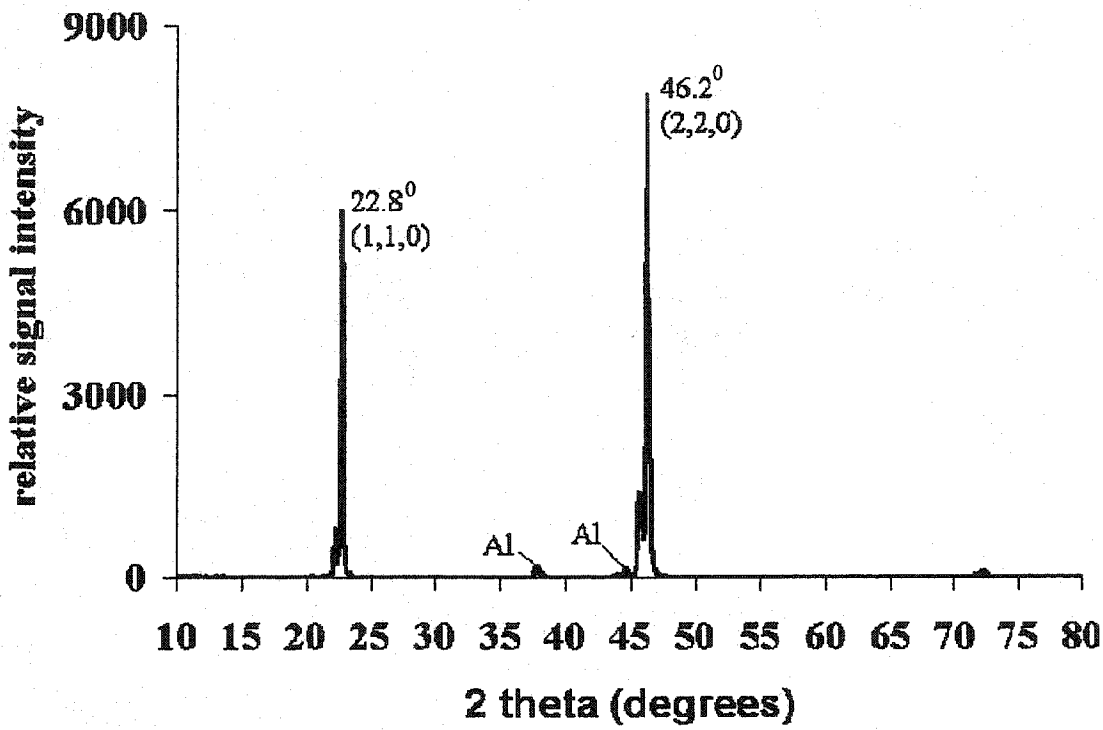


FIG. 5. Two theta XRD data for unpolished face of crystal K4A.

The quality of the crystal can be described by measuring the the full width at half maximum (FWHM) value of the omega scan. The theory of XRD assumes a perfect crystalline lattice, which produces delta function peaks. Real crystals may have defects that affect the width of the XRD peaks. The most notable defect that affects the width of the XRD peaks is polycrystalline structure. Previous work on chalcopyrites and defect chalcopyrites has shown XRD diffraction peaks with widths on the order of 0.1° [32]. Table 2 shows that most of the crystals have FWHM of similar magnitude.

The two theta scan for crystal K4A also illustrates how diffraction can occur for multiples of a plane. The two peaks arising from $CdGa_2S_4$:Cr are at 22.8° and 46.3°. The Miller indices for these peaks are (1,1,0) and (2,2,0). From the Bragg equation, Eq. (4), it can be noted that the diffraction peaks may occur at integer multiples of the wavelength. Usually, the Miller difraction planes are only computed for n=1. For diffractions resulting from higher multiples of wavelength, the Miller indices will equal a multiple of the plane for n=1. For example, from a crystal face cut on the (1,1,0) plane it is also possible to obtain diffraction peaks from n equal to two that are consistent with (2,2,0) diffraction peaks.

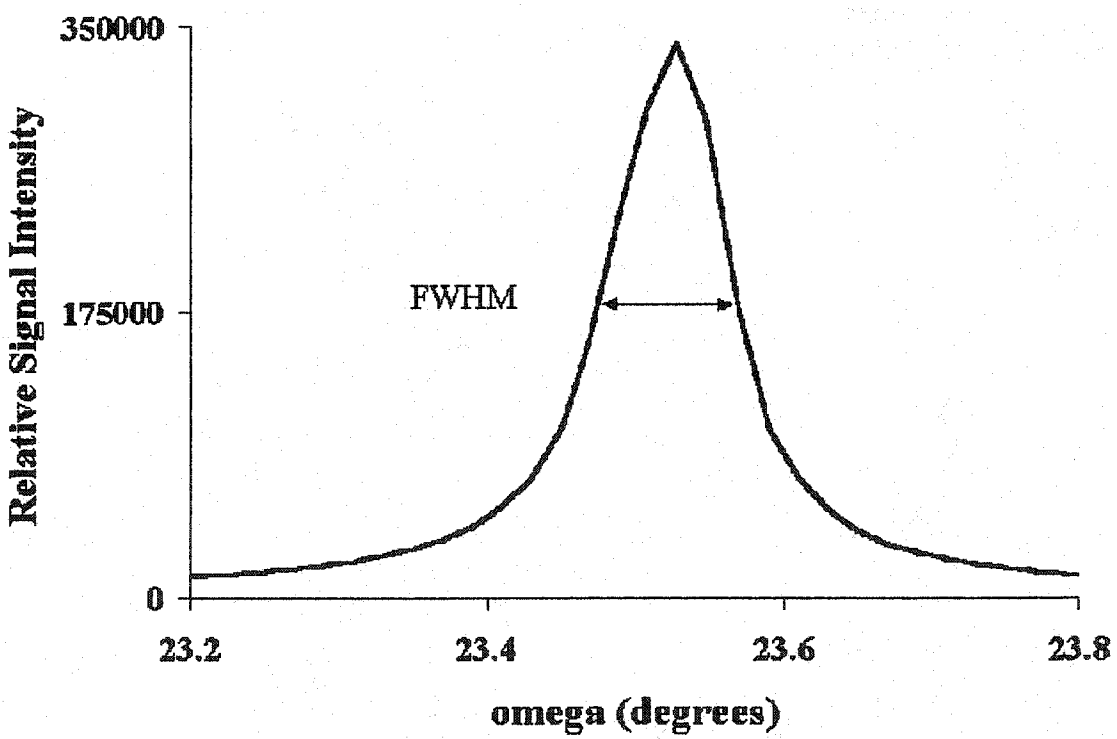


FIG. 6. Omega-rocking scan XRD data for the diffraction peak of (2,2,0) on the unpolished face of crystal K4A.

Table 2 lists the Miller indices for $CdGa_2S_4$ crystals investigated with XRD. The crystal quality was good. Only crystal K1 was considered to be unacceptable for EPR analysis. K1 had one XRD peak in the two theta scan with a FWHM of 2°. This peak did not correspond to an expected diffraction peak from the defect chalcopyrite structure. The width of XRD peaks for K1 may be caused by crystal defects such as polycrystalline inclusions. Analysis of the two theta and omega rocking scans for peaks attributed to $CdGa_2S_4$ and $CdGa_2S_4$:Cr are summarized in Table 2.

Side 1 of most crystals was undetermined by XRD. This side was optically polished. Vector analysis was used to determine the third side if all three sides of the crystals could not be determined by XRD. The planes that were determined mathematically are placed in {} brackets in Table 2. The mathematically determined crystal planes for the optically polished side do not fulfill the interference conditions listed in Eq. (6).

## B. EDXS

When an atom is bombarded with high energy electrons, X-rays are produced as the atoms are ionized. Each atom has a unique fingerprint of energies produced by the ionization. EDXS analyzes the energy distribution of a sample after the sample has been bombarded with high energy electrons. The specific atoms in the sample may be determined to approximately 1 mole percent concentration. Also, it is possible to use EDXS to approximate the ratio of elements in the sample.

The high energy electrons used to ionize a sample in EDXS will produce X-rays as an electron falls from a higher level to replace the lower level electron that has been displaced. As an electron from the higher shell falls to the lower level, it will emit

TABLE 2. Crystal orientations in tetragonal Miller coordinates. Orientations determined mathematically are shown in brackets. The abbreviation undet. is used for undetermined.

| | Side 1 (polished)XRD | | Side 2 (unpolished)XRD | | Side 3 (least area)XRD | |
|---|---|---|---|---|---|---|
| | Plane | FWHM | Plane | FWHM | Plane | FWHM |
| K1 | Undet | | Undet. | | Large peak 24-26° | |
| K2 | {1,1,1} | | (3,1,4) | 0.09 | 2.2° from (1,1,2) | 0.1° |
| K3A | Undet | | Undet | | 7.3° from (1,1,2) | 0.1° |
| KUn | {5,5,9} | | Undet. from (1,1,0) | | 2.2° from (1,1,2) | 0.05° |
| K4 | {5,5,9} | | Assumed >5° from (1,-1,0) | | 5.7° from (1,1,2) | 0.06° |
| K4A | {5,5,9} | | 0.4° from (1,1,0) | 0.11° | 1.8° from (1,1,2) | 0.06° |
| K5 | 2.7° from (1,0,1) | 0.2° | Undet from (2,1,3) | | {4,0,1}. | |
| K6 | 3.65° from (0,0,4) | 0.8° | 6.8° from (1,-1,0) | 0.4° | {1,1,0} | |
| | 3.55° from (1,0,1) | 0.2° | | | | |
| B1 | {0,1,2} | | 5.4° from (2,0,4) | 0.2° | (3,2,3) | 0.3° |
| B2 | {1,-1,0} | | 1.8° from (1,1,0) | 0.2 | 0.3° from (0,0,4) | 0.2° |
| | {1,-1,1} | | | | 5.4° from (3,1,2) | 0.2° |

X-rays. Because the elemental fingerprint depends on the final orbit of the electrons, elements are often referred to by a letter that corresponds to the orbital. The designation of K, L, and M correspond to final orbital values with principal numbers of 1, 2, and 3, respectively. The expected X-ray fingerprint used in EDXS from all elements is well established. The software associated with EDXS will analyze sample composition based on elemental series chosen by the user by a standardless ZAF analysis. This type of analysis is described in most texts concerning EDXS. I refer the interested reader to *Fundamentals of Energy Dispersive X-Ray Analysis* by John Russ for details. This analysis produces a list of the elements in the sample of the percentage of composition by weight.

The first set of crystals received from Kuban State, labeled K1, K2, and K3, were analyzed with EDXS to assess crystal composition and dopant levels. Crystals K1, K2, and K3 were doped at the level of 1 mole percent, which might be measurable in EDXS. There was a color variation among these crystals. Crystals K1 and K2 were almost topaz in color. Crystal K3 was significantly more yellow. K3 was made with the same dopant concentration as K1 and K2 but was annealed. Three or four spots on each crystal were chosen for analysis to determine whether the stoichiometry varied in the crystal. These spots were chosen in different sections of the crystal, but the overall area of the crystal sampled with EDXS was less than 1%.

Output spectra showed peaks consistent with cadmium and gallium L shell and sulfur K shell X-rays. Crystals K1 and K2 had a small peak near the energy level of chromium's K shell. K1 and K2 crystals were analyzed with cadmium, gallium, sulfur, and chromium as constituents. K3 was only analyzed with cadmium, gallium, and sulfur as constituents, because this crystal did not have a peak near the chromium output. The

output from the analysis is in weight percent for each element. The output was converted to mole percent to get an approximate idea of the stoichiometry. Table 3 shows the results of EDXS analysis.

TABLE 3. EDXS results for $Cd_wGa_xS_y:Cr_z$

| Crystal | $Cd_w$ w | $Ga_x$ x | $S_y$ y | $Cr_z$ z |
|---|---|---|---|---|
| K1 | 0.23 ± 0.01 | 0.80 ± 0.04 | 0.55 ± 0.06 | 0.01 ±0.01 |
| K2 | 0.25 ± 0.03 | 0.78 ± 0.06 | 0.53 ± 0.03 | 0.02 ± 0.00 |
| K3A | 0.27 ± 0.01 | 0.72 ±0.01 | 0.62 ± 0.00 | N/A |

Because the XRD studies of crystal K1 did not show any peaks that could be identified with a defect chalcopyrite, it is not certain K1 has a defect chalcopyrite structure. Therefore, K1 will not be considered in the compositional analysis, because this crystal may not have the same crystal structure as K2 and K3A.

The annealed crystal, K3A, was significantly more consistent in composition than the unannealed crystal K2. Within the accuracy of the equipment, the annealed crystal, K3A, did not have any standard deviation in composition to the second digit. The deviation in percentage of composition was measurable to the second digit in the unannealed crystal. The percentages of cadmium and sulfur were increased in the annealed crystal, K3A, relative to the unannealed crystal, K2. The percentages of gallium and chromium were reduced in the annealed crystal. If the analysis for chromium in these samples is believed, there is significant deviation in the levels of

chromium throughout crystal K2, which might be indicative of clumping. The color for the annealed sample, K3A, was significantly more yellow than the color of the un-annealed samples. The unannealed samples, K1 and K2, which were studied with EDXS, have a yellow-brown color similar to topaz. Although the other crystals were not studied with EDXS, all the other samples received are pale yellow.

# CHAPTER 4

## EPR

The spin of an electron is described only through the quantum mechanical properties of the system. The manifestations of spin were first demonstrated in the laboratory through the Stern-Gerlach experiment. In 1922 Stern and Gerlach showed that a beam of Ag atoms placed in a magnetic field is split into two separate beams. This finding proved that the angular momentum of electrons was a quantum effect. However, the proper interpretation for the Stern-Gerlach experiment did not come until after Goudsmit and Uhlenback proposed in 1925 that the electron possessed an intrinsic angular momentum, which gave electrons a constant magnetic moment. The constant magnetic moment of an electron is generally referred to as the spin of an electron. The realization of an electron spin allowed the anomalous Zeeman effect to be explained. In the anomalous Zeeman effect more spectral lines are seen from atoms in a magnetic field than can be explained by the Bohr-Sommerfield theory of the atom [33].

EPR, or electron spin resonance, ESR, as it is often called, utilizes magnetic fields and microwave radiation to resonate between the angular momentum projections, $m_s$, of a spin state, S. Only unpaired electrons will produce a signal in EPR experiments. When placed in a magnetic field, an electron will precess about the magnetic field with a frequency, $\omega$, proportional to the applied magnetic field [33]. Absorption of electromagnetic radiation occurs when the electron's frequency of precession equals the frequency of the electromagnetic radiation [34]. In field swept EPR, which is utilized in

the experiment, microwave radiation of a single frequency is applied to the sample while an applied magnetic field is varied. In solids, the centers responsible for this absorption are often defects present in small quantities. Detection methods such as phase sensitive detection are often used to increase the signal to noise ratio.

Because EPR deals with the energy of a quantum mechanical system, it is necessary to describe the Hamiltonian of the system. The Hamiltonian of an electronic system may be described by spatial and spin contributions. In magnetic resonance studies, the spatial portion may be integrated over all space to yield numerical values. The remaining spin portion of the Hamiltonian, the spin Hamiltonian, contains the aspects pertaining to EPR [35]. The energy levels predicted by the Hamiltonian are then analyzed to determine at which magnetic fields microwave absorption will occur.

Often the Hamiltonian used to describe the EPR experiment assumes that the paramagnetic centers are associated primarily with a defect and interact weakly among themselves or with the host crystal. Unfortunately, the spectra do not fit the angular or line width variation expected of the standard theory. There are two possible explanations for the differences seen in the spectra: Either the centers represent shallow effective mass like acceptors, or they are exchange coupled systems. In the sections below the Hamiltonian and EPR spectra expected from the commonly used theory are described first. Then the Hamiltonians and deviations from the commonly used theory seen for effective mass like acceptors and exchange coupled systems are discussed. In the following discussions of EPR the effects of the nuclear magnetic field on EPR are not considered, because these effects are not seen in the samples.

## A. EPR of noninteracting centers

### *1. EPR of defects*

Generally EPR assumes that individual paramagnetic centers are dilute within the sample. By dilute it is meant that the centers are separated from each other and only interact weakly with each other. In most solids the defects are present in sufficiently low quantity for the defects to be dilute. The Zeeman effect dominates noninteracting centers. The Hamiltonian of the Zeeman interaction between an electron and a magnetic field is written as Eq. (7) [33].

$$H = -\mu \bullet \mathbf{B}. \tag{7}$$

The electron spin magnetic moment, $\mu_e$, of the system is proportional to the spin operator, $S$, through the constants $g$, the Zeeman factor, and $\beta_e$, the Bohr magneton, as illustrated in the following equation [33].

$$\mu_e = -g\beta_e \mathbf{S}. \tag{8}$$

It is usually assumed the contributions from orbital angular momenta, **l**, are minor. Physically, the small orbital angular momentum may be explained by realizing the electrons associated with a single atom are constrained to move within a finite space because of electrical interactions with the neighboring atoms. Because the electrons are not free to circulate, they tend to have small orbital angular momenta. In addition, the orbital angular momentum couples to the spin with a coupling constant λ. Therefore, the magnetic moment with the addition of orbital angular momentum is described fully by Eq. (9) [33].

$$\mu = -\beta_e(\mathbf{l} + g\mathbf{S} + \lambda\, \mathbf{l} \bullet \mathbf{S}) \tag{9}$$

Because the orbital angular momentum expected to contribute much less than the free electron spin to the Hamiltonian, it is possible treat the orbital angular momentum as a perturbation of the Hamiltonian for the Zeeman effect. The first order terms from the orbital angular momentum perturbation of a free electron are zero. The second order terms from perturbation theory yield a matrix, $\mathbf{\Lambda}$. The orbital angular momentum's contribution to the Zeeman effect is accounted for by creating a tensor, $\underline{g}$, which is defined in Eq. (10) [33]. The 3X3 unit matrix is $\mathbf{1_3}$.

$$g = g_e \mathbf{1_3} + 2\lambda\mathbf{\Lambda}. \tag{10}$$

The spin-orbit interaction term, **D**, may be written in terms of the perturbation theory as [33]

$$\mathbf{D} = \lambda^2 \mathbf{\Lambda}. \tag{11}$$

The following equation lists the Hamiltonian for the electron and orbital angular momentum [33].

$$H = \beta_e \mathbf{B}^T \bullet \underline{g} \bullet \mathbf{S} + \lambda^2 \left( \mathbf{S}^T \bullet \mathbf{\Lambda} \bullet \mathbf{S} \right). \tag{12}$$

There is another correction to the Hamiltonian for systems with spin of one or greater. In transition metal ions the spin is generally greater than or equal to one, and there is an additional need to include this correction in the Hamiltonian. When two or more electrons are present these electrons may interact through exchange and dipole interactions. The exchange interactions depend on distance between the interacting defects. The Hamiltonian for the exchange energy is [33]

$$H_{ex} = J\left(\mathbf{S}_1^T \bullet \mathbf{S}_2\right). \tag{13}$$

The isotropic constant $J$, Eq. (14), is determined from the exchange integral for the wavefunctions of the two paramagnetic centers, $\Psi_1$ and $\Psi_2$, which are separated by a

distance $r$ [33]. The vectors $r_1$ and $r_2$ describe the positions of the two paramagnetic centers.

$$J = \int \Psi_1(r_1)\Psi_2(r_2)\left(e/r_{12}\right)^2 \Psi_1(r_2)\Psi_2(r_1)d\tau_1 d\tau_2 . \tag{14}$$

For dilute systems the defects are far apart, so the exchange interaction is generally negligible. Therefore, exchange interactions are not included in the Hamiltonian for a dilute system of defects. However, the magnetic dipole interactions between electrons will create a magnetic field that is always present in the solid. The Hamiltonian, $H_{ss}$, for the magnetic dipole interaction between two paramagnetic centers depends on the magnetic dipole of each center, $\mu_1$ and $\mu_2$, as well as the distance between the centers, $r$ [33].

$$H_{ss} = \frac{\mu_0}{4\pi}\left[\frac{\vec{\mu_1}\bullet\vec{\mu_2}}{r^3} - \frac{3\left(\vec{\mu_1}\bullet\vec{r}\right)\left(\vec{\mu_2}\bullet\vec{r}\right)}{r^5}\right]. \tag{15}$$

The magnetic dipole-dipole field is anisotropic and will cause a splitting of the eigenfunctions of $S_z$ in the absence of an external applied magnetic field, referred to as the zero field splitting. The Hamiltonian for the magnetic dipole-dipole effects is quadratic in spin. Generally the Hamiltonian is written in a matrix notation so that the dipole-dipole interactions are described through a matrix D. The final Hamiltonian for dilute paramagnetic centers is given by the following equation [33].

$$H = \beta e \mathbf{B}^T \bullet \underline{\mathbf{g}} \bullet \mathbf{S} + \mathbf{S}^T \bullet \underline{\mathbf{D}} \bullet \mathbf{S} . \tag{16}$$

The symmetry of the environment surrounding the defect will affect how the **g** values change as the crystal is rotated about an axis. Defect symmetry may be cubic; uniaxial, which is sometimes called axial; and rhombic. In axial symmetry there is an axis about which rotation shows no deviations of the EPR signal. One reason for the

interest in chalcopyrites as a host for dopant atoms is that they have a naturally occurring compression of the c axis. The compression of the c axis removes degeneracy of the electronic orbital energy levels and creates a symmetry axis. Defects in $CdGa_2S_4$ are expected to have an axial symmetry because of the compression on the c axis. Therefore, chromium in $CdGa_2S_4$ should have axial symmetry.

The principal axis system, where **g** is diagonal, of an axially symmetric defect will have two values that are the same, $g_\perp$, or $g$ for the applied field perpendicular to the axis of symmetry, and one value that is different, $g_{//}$, or g for the applied field parallel to the axis of symmetry. At an angle between the applied field and the symmetry axis, $\theta$, the value of $g$, $g(\theta)$, is determined from the following equation [33].

$$g(\theta) = \sqrt{\left(g_{//}\cos(\theta)\right)^2 + \left(g_{\perp}\sin(\theta)\right)^2}. \tag{17}$$

$Cr^{3+}$ in $Al_2O_3$, ruby, is an example of a magnetically dilute EPR center with an axial symmetry. The $Cr^{3+}$ ion has three unpaired electrons that interact to give the ion an effective spin of three halves (3/2). The EPR experiments found a $g_{//}$ value of 1.984 and a $g_\perp$, value of 1.986 for $Cr^{3+}$ in $Al_2O_3$. The zero field splitting of $Cr^{3+}$ in $Al_2O_3$ has been determined to be $-0.1915$ $cm^{-1}$. Data taken at several axes were consistent with an axial symmetry [36].

### *2. EPR of shallow effective-mass acceptors*

Chromium has been shown to act as an acceptor in the II-VI compounds ZnS and CdTe [37]. Because $CdGa_2S_4$ is similar to the II-VI compounds, it is reasonable to believe that chromium may be an acceptor in $CdGa_2S_4$. Previous TSL, TSC, and PL experiments on $CdGa_2S_4$:Ag have shown that Ag behaves as an acceptor in $CdGa_2S_4$

[22]. Shallow acceptors in semiconductors may be described through the effective-mass approximation. In semiconductor physics effective-mass acceptors can be described in the Hartree-Fock approximation. Even when effective-mass acceptors are dilute, their Hamiltonian is different from the Hamiltonian described in the preceding sections.

Shallow acceptors will have EPR spectra with a large anisotropy. The $g$ values of shallow acceptors should change as the sample is rotated about different axes [38]. Watkins has shown for aluminum in 6H-SiC that the $g$ tensor may be described for any angle by the following equation.

$$g(\theta) = K\cos(\theta) \tag{18}$$

In this equation theta is the angle between the applied magnetic field and the crystal c axis, and $K$ is a constant that depends on the material [39].

Shallow acceptors lie close to the valence band. The wavefunction of the shallow acceptor will overlap with the valence band, leading to a mixing of spin states between the acceptor and valence band. As the angle is varied the probability of transitions between spin states will vary, resulting in varying intensity of the EPR signal. The EPR line shape will vary with angle, although the manner has not been predicted for shallow acceptors in $CdGa_2S_4$. The line width of the shallow effective-mass acceptors depends on how fully the acceptor interacts with the valence band. How the line width should vary with angle has not been described for shallow acceptors in $CdGa_2S_4$.

## B. EPR of exchange coupled system

This section will discuss the spin Hamiltonian for exchange interactions between paramagnetic centers. First how spin states greater than one-half are treated for atoms

that have more than one unfilled orbital in a dilute system is discussed. Next the problem of electron exchange interactions on two separate atoms is discussed.

The Hamiltonian for many electron atoms is written with an electron exchange term. When the Hamiltonian is solved for the many electron atoms, the electronic orbitals have the exchange between electrons included in their quantum mechanical description. In an EPR experiment on an atom with multiple unfilled electron orbitals, an exchange term for the electrons between orbitals of the atom does not need to be included. For example, $Cr^{3+}$ in ruby has three unpaired d orbital electrons. The spin Hamiltonian for $Cr^{3+}$ in ruby uses the total spin state of 3/2. The Hamiltonian is not written with terms for the spin of all three unpaired electrons and the exchange interaction among the three electrons.

For an exchange coupled system the electrons are exchanging between orbitals of two different atoms. Because the exchange coupled system is between orbitals of different atoms, the spin Hamiltonian must have a term that explicitly considers the exchange interaction between the electrons. In the standard dilute description of EPR the exchange interaction between paramagnetic centers is assumed to be negligibly small.

In the next sections the origins of the exchange interactions are explained, as well as what may cause the exchange interaction to be large enough to dominate the EPR spectra. The spin Hamiltonian for exchange coupled systems is described. Last, the effects of a strong exchange on EPR spectra and the exchange narrowing of resonance lines are described.

*1. Exchange Interaction*

There are several types of exchange interactions that may exist within a solid. The easiest exchange interaction to understand is the direct exchange. In the following section this type of exchange is discussed in the most detail. However, a more common type of exchange interaction is superexchange, which occurs between paramagnetic centers that are separated by nonmagnetic ion(s). It is also possible for partially filled f-shells atoms to experience both direct exchange and exchange that occurs through the conduction electrons, which is referred to as indirect exchange [40].

Because nuclei can be modeled as a potential well, the effect of two identical atoms next to each other, as in a solid lattice, may be modeled as a double potential well. The double potential well system may provide insight into exchange coupling on a basic level. Using quantum mechanics to find the motion of two electrons of mass m in the potential wells of two identical nuclei, V(x), such that

$$V(x) = (1/2)m\omega^2(|x| - a)^2, \tag{19}$$

determines that the resulting wavefunctions for

$$a >> \sqrt{\left(h/m\omega^2\right)} \tag{20}$$

initially have an electron in each well. When the time evolution is applied to the system, the two electrons exchange places during a time, $\tau$ , of [41]

$$\tau = \left(\pi/2\right)\sqrt{\left(\hbar\pi/2V_0\omega\right)}\exp\left(2V_0/\hbar\omega\right). \tag{21}$$

Here $V_0$ is the energy where the two potential wells intersect, as measured from the bottom of the potential wells. In all exchange coupled systems the exchange referred to is the swapping of the positions of the masses. To return to the description of two nuclei

close to each other, the electrons will swap positions between nuclei with a certain time constant.

Although the double oscillator model provides useful information about molecules, the description of effects within a solid is more complex. The Hartree-Fock approximation may be used to address the interaction of electrons within a crystal lattice. The Hamiltonian within a solid would be unsolvable if the complete interactions within a solid were considered. Hartree-Fock assumes that an individual electron interacts with a continuous distribution of electrons. The exchange term resulting from this assumption is $J$, defined in Eq. (14). The exchange interaction term in the Hartree-Fock equation implies that the motion of an electron in a solid interacts with the other electrons in a way that depends on the individual electron's position [42]. Additionally, the Hartree-Fock approximation contains a delta function in the exchange interaction; therefore, the exchange term is zero for electrons of opposite spin [43].

In the double well model, $\tau$, the period of oscillation of the electrons between the two nuclei, increases as the nuclei come closer together, or the parabolic shape of the nuclei gets wider. Similarly, in a solid the isotropic exchange constant will increase either as the paramagnetic centers come closer together or as their wavefunctions become larger. One way to gauge the probability of exchange within a solid is to look at the orbitals of the paramagnetic centers involved in the exchange.

Exchange strength can be discussed in terms of the covalency of the bonds involved in the exchange interaction. The exchange constant increases as the orbitals of the atoms involved in the exchange become more covalent. In terms of dopant atoms in a crystal, the more covalent the impurity and host orbitals are, the more likely the dopant atom is to form an exchange interaction with the atoms in the surrounding crystal host.

*2. Exchange Hamiltonian*

Heisenberg described the Hamiltonian for an exchange interaction between spins $S_1$ and $S_2$ in terms of the isotropic exchange constant $J$ in Eq. (13). Although only the linear term is considered, it is also possible to have a biquadratic term of exchange [44]. The complete theory of exchange coupling between spin centers takes into account spin-orbit coupling, relativistic effects, and exchange interactions with excited states of the atoms. The exchange Hamiltonian which includes the complete theory of exchange coupling is [44]:

$$Hex = J(\mathbf{S}_1 \bullet \mathbf{S}_2) + \mathbf{S}_1 \bullet \underline{\mathbf{D}} \bullet \mathbf{S}_2 + d(\mathbf{S}_1 \times \mathbf{S}_2). \tag{22}$$

In this expression, the $\underline{\mathbf{D}}$ term also incorporates the dipole-dipole interactions that occur between the two centers.

The total Hamiltonian for the system, $H_S$, incorporating the exchange effect is [44]

$$Hs = \beta e \mathbf{B}^{\mathrm{T}} \bullet \underline{\mathbf{g}} \bullet (\mathbf{S}_1 + \mathbf{S}_2) + (\mathbf{S}_1 + \mathbf{S}_2)^{T} \bullet \mathbf{D} \bullet (\mathbf{S}_1 + \mathbf{S}_2) + H_{ex}. \tag{23}$$

Because it is difficult to solve the total Hamiltonian, often a Hamiltonian is created for transitions that occur in each of the total spin manifold with the form [44]

$$H = \beta_e \mathbf{B}^{\mathrm{T}} \bullet \underline{\mathbf{g}} \bullet \mathbf{S}_T + \mathbf{S}_T^{T} \bullet \mathbf{D} \bullet \mathbf{S}_T. \tag{24}$$

The total spin state, $S_T$, is found by adding the spins involved in the exchange system. From quantum mechanics it is known that the addition of two angular momentum states, which include spin, gives a range of possible resulting states. If two spins states, $S_1$ and $S_2$, are added the resulting total spin, $S_T$, can have values [33]

$$S_T = \{-(S_1 + S_2), -(S_1 + S_2) + 1, \ldots, (S_1 + S_2) + 1, (S_1 + S_2)\}. \tag{25}$$

Because the complete Hamiltonian for exchange coupled centers includes spin-orbit coupling and dipole-dipole interactions, the EPR spectra may show large angular

and line width variability. The spin-orbit coupling causes anisotropic and off diagonal terms to appear in the D matrix [44]. The inclusion of spin-orbit coupling is particularly difficult to accomplish. Only the basics of the treatment are outlined below.

The coupling for each center is represented through the usual Hamiltonian:

$$H_\alpha = \lambda \mathbf{L} \bullet \mathbf{S} \tag{26}$$

The exchange Hamiltonian for the centers is found by treating the spin-orbit for each center as a perturbation. As with the dilute systems, the spin-orbit coupling may be included by viewing $J$ as a tensor instead of a scalar. However, the integral involved in the perturbation theory includes exchange interactions between the ground and excited states of the different centers [44].

### *3. Effects of exchange interactions on EPR spectra*

Exchange interactions may cause many effects on EPR spectra. The two main factors to consider in determining the effects of exchange are the number of interacting centers and the size of the isotropic exchange interactions. Exchange systems may exist between a small number of paramagnetic centers to yield dimers, trimers, or clusters. If the exchange system contains a large number of paramagnetic centers that are linear within the crystal, the exchange system may exist as one, two, or three dimensional chains. The difference in the EPR spectrum of an exchange coupled system, as opposed to a non-exchange coupled systems, is particularly striking if the isotropic exchange energy, $J$, defined in Eq. (14), is greater than the microwave energy of the EPR system, or if the isotropic exchange energy, $J$, is greater than the energy of the dipole-dipole interaction, and exchange narrowing of the resonance occurs. The strong exchange

regime and exchange narrowing will be discussed in the following sections, since it may be applicable to $CdGa_2S_4$:Cr.

If the isotropic exchange energy is greater than the microwave energy, the EPR spectrum is referred to as being in the strong exchange regime. In the strong exchange regime, the EPR spectrum of pairs often consists of transitions from one or more total spin states [44]. The theory of strong exchange is essentially the EPR theory for spin states greater than one-half. The Hamiltonian for the strong exchange regime is Eq. (13), with the other terms treated as perturbations to this Hamiltonian. In contrast, the appropiate Hamiltonian for the weak exchange limit is Eq. (23). The EPR spectra of weak exchange will show additional resonances near the g values for the individual ions involved in the exchange interaction [44]. Figure 7 illustrates the difference between a strong exchange and a weak exchange.

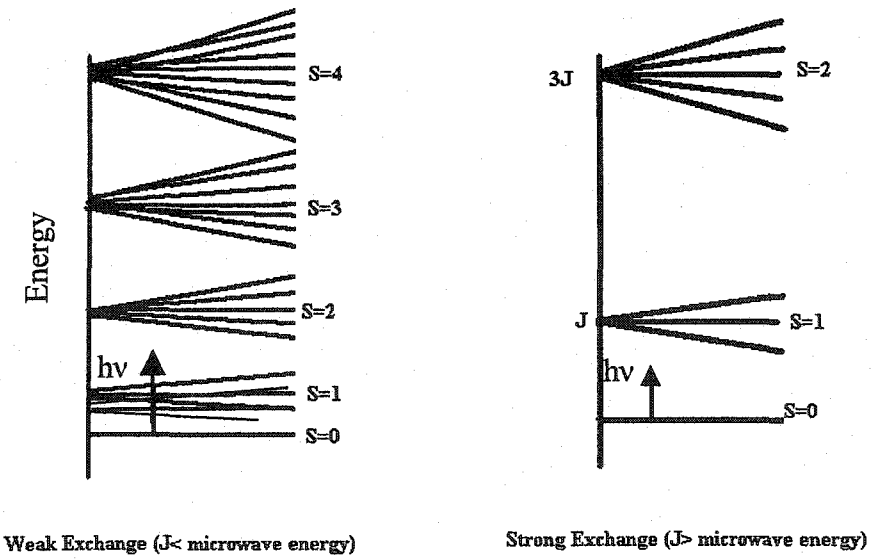


FIG. 7. Energy diagram for weak and strong exchange limits. The energy of the applied microwave radiation in the EPR experiment is hv.

*4. Exchange narrowing*

For the ensemble of spins in an exchange system with the total spin value of magnetization M and gyromagnetic ratio γ, the discussion of exchange narrowing is begun by considering how the spin precesses about an external magnetic field $B_0$. In EPR the external magnetic field, $B_0$, that the electron experiences is the sum of the applied magnetic field and the local field. When the electrons are exchanging between centers with different local magnetic fields, the magnetic field the center experiences will change with time. This time varying field is designated B(t). Exchange narrowing can be discussed by considering the precession of the spin about the magnetic field $B_0 + B(t)$.

Consider B(t) as a fluctuation of $B_0$. If the electron is assumed to have a linear response to this fluctuation, the equation of motion for the spin precession is [44]

$$\frac{dM_x}{dt} = i\omega(t)M_x. \tag{27}$$

The solution to Eq. (27) is a modulated oscillator, with the modulation corresponding to $\omega(t)$. The time average of this modulation is $\omega_0$. The value of $M_x$ at any time $t$ is [44]

$$M_x = M_x(0)\exp\left\{i\int_0^t \omega(t')dt'\right\}. \tag{28}$$

$F(t)$ is defined to equal the integral in the exponential portion of Eq. (28). To analyze the integral portion of the exponential, the time varying modulation $\omega(t)$ must be described. The time varying modulation, $\omega(t)$, is defined in terms of the magnitude, $\Omega$ , and the characteristic time, $\tau_c$. The magnitude, $\Omega$, is defined as the average square modulus of the modulation $\omega(t)$. The characteristic time is a measure of how fast the modulation occurs. In exchange coupling the time variation of the modulation is caused by the exchange of

the electrons between the two atoms. The isotropic exchange coupling constant, $J$, is often used to approximate the characteristic time by Eq. (29).

$$\tau_c \cong \frac{\hbar}{J}. \tag{29}$$

A fast modulation is defined as one with a small characteristic time, which satisfies Eq. (30).

$$\Omega\tau_c \ll 1. \tag{30}$$

For a fast modulation the characteristic time is small enough for the time, $t$, in the integration of $F(t)$ to include many fluctuations of the modulation $\omega(t)$. The time average of $\omega(t)$ will be a constant. Therefore, $F(t)$ will be proportional to the time $t$.

A slow modulation is defined as one with a large characteristic time, which satisfies Eq. (31).

$$\Omega\tau_c \gg 1. \tag{31}$$

Because the characteristic time is large for a slow modulation,the integration of $F(t)$ will not include a complete cycle of $\omega(t)$. Since only a portion of a cycle of $\omega(t)$ occurs in the integration time $t$, the integrand will be proportional to the time $t$. The integral $F(t)$ will be proportional to the square of time. Dipole-dipole interactions depend on the distance between the centers involved in the exchange interactions. Unless the centers are very close to each other, dipole-dipole interactions are in the slow modulation regime.

Using the fluctuation-dissipation theorem for a linear response system, Eq. (32), which is the the Fourier transform of F(t), equals the resonance absorption spectrum at the frequency $\omega$ [44].

$$I(\omega-\omega_0)=\left(\frac{1}{2\pi}\right)\int\exp\left(-i(\omega-\omega_0)t\right)\exp\left(iF(t)\right)dt\,. \tag{32}$$

In an EPR experiment, the intensity of the absorption of microwaves of frequency $\omega$ for an exchange coupled system is equal to Eq. (31). The Fourier transform, Eq. (32), for a fast modulation produces a Lorentzian absorption curve, and a slow modulation produces a Gaussian absorption curve [44]. The Gaussian curve is significantly broader than the Lorentzian curve.

When the energy of the exchange coupling is greater than the energy of the dipole-dipole interaction, the exchange modulation will dominate the spectra. Because the exchange interaction will produce a fast modulation, the absorption line shape will be Lorentzian. The absorption will take place at the time average of the modulation, $\omega_0$. In EPR experiments the effect of the absorption occuring at $\omega_0$ is that the resonance will occur at a g value that is the average g value of the centers in the exchange coupling. This effect is referred to as an exchange narrowed resonance.

Because the dipole-dipole interactions occur along a line connecting the exchange centers, the dipole-dipole contributions to the line shape and line width are largest when the external magnetic field is in this direction. Therefore, an exchange narrowed resonance will become more Gaussian and broaden when the external magnetic field is in the dipole-dipole direction. By plotting the change in the peak to peak width of the resonance, $\Delta B_{pp}$, the dipole-dipole interaction may be characterized. The dipole-dipole interaction causes a variation of $\Delta B_{pp}$ with $\theta$, the angle between the applied magnetic field and the dipole-dipole direction, of the form in Eq. (33) [44].

$$\Delta B_{pp}=A+B\left(3\cos^2(\theta)-1\right)^n. \tag{33}$$

The value of n is determined in part by the type of exchange system. For an exchange system between chains of atoms, n equals to four thirds. For an exchange system between dimmers, n equals to two [44]. The maximum line width of exchange systems varies greatly among solids. Maximum line widths of over 1,000 Gauss have been reported in exchange coupled systems [44].

In addition to determining the line shape of an EPR absorption curve, exchange narrowing will also change the number of lines present in the EPR spectra. When the characteristic time of a fluctuation is small, the electron precession changes before a quanta of radiation may be absorbed. A small characteristic time leads to the absorption of radiation at the average frequency of the fluctuations. Exchange narrowing of a total spin state results in a single resonance line that is centered at the average g value of all the centers involved in the exchange.

Let us go over in detail how the g value of an exchange narrowed line will be computed for a crystal with axes a, b, and c. Assume that two centers are interacting. The first paramagnetic center, a, will have the following g tensor:

$$\underline{g_a} = \begin{bmatrix} g_{a11} & g_{a21} & g_{a31} \\ g_{a12} & g_{a22} & g_{a32} \\ g_{a13} & g_{a23} & g_{a33} \end{bmatrix}. \tag{34}$$

The second paramagnetic center, b, will have the g tensor given below.

$$\underline{g_b} = \begin{bmatrix} g_{b11} & g_{b21} & g_{b31} \\ g_{b12} & g_{b22} & g_{b32} \\ g_{b13} & g_{b23} & g_{b33} \end{bmatrix}. \tag{35}$$

The resulting g tensor for the exchange narrowed interaction of these two centers would be given by the tensor in Eq. (36) [45]:

$$\underline{g_T} = \left(\frac{1}{2}\right)\begin{bmatrix} g_{b11}+g_{a11} & g_{b21}+g_{a21} & g_{b31}+g_{a31} \\ g_{b12}+g_{a12} & g_{b22}+g_{a22} & g_{b32}+g_{a32} \\ g_{b13}+g_{a13} & g_{b23}+g_{a23} & g_{b33}+g_{a33} \end{bmatrix}. \quad (36)$$

The averaging of g values in a plane is illustrated for $[MoOCl_3(hmpa)_2]$. Fig. 8, reprinted from [45] with permission of Elsevier Publishing, illustrates the effects of exchange narrowing on EPR spectra taken about different axes of rotation. .The dashed

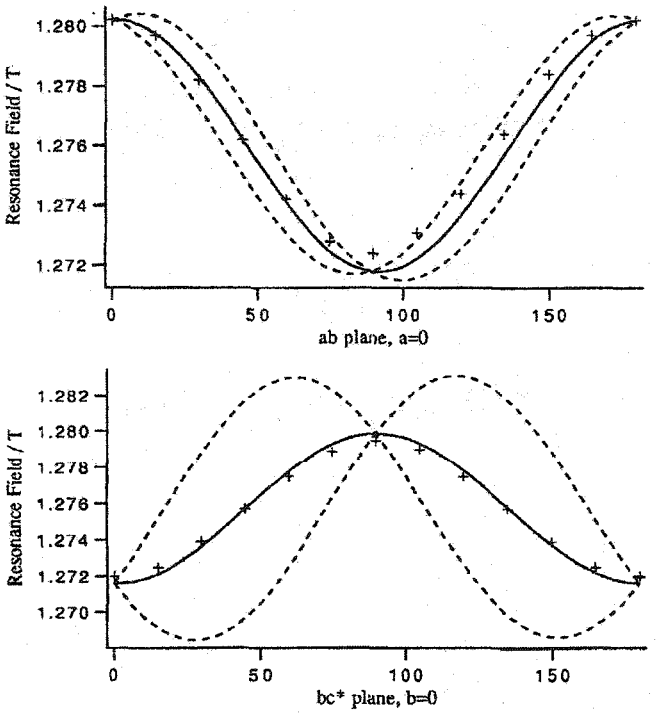


FIG. 8. Comparison of exchange and non-exchange systems for [MoOcl3(hmpa)2]. The dashed lines are expected g value without exchange narrowing, solid line is average of dashed lines, and + is experimental values.

line,which represents the expected EPR signal without exchange narrowing, changes as the EPR spectum is taken about two different rotation axis. The solid line is the average of the g values in the different axis of rotation. The plus marks are the experimental data. Although the spectrum without exchange changes in the different rotation axis, the

average of the nonexchanged spectra does not significantly change about the different rotation axis. The experimental values of the resonances do not significantly vary as the rotation axis changes, which is consistent with the expected values of exchange narrowed resonances.

### *5. Temperature effects on exchange spectra*

The exchange interaction is not dependent on temperature. However, temperature effects may be used to differentiate between chains and other types of exchange systems. For instance, a temperature dependent line width occurs in chains because of local ordering within the sample as the temperature is lowered to a critical point. It has been noted that some chains also have a shift in g values at lower temperature [44]. There should be no effect of temperature on line width or g value in exchange coupled pairs [44].

Although the line width of exchange coupled pairs is temperature independent, the intensity of the spectra will change as the temperature is varied. In pairs the EPR spectrum often consists of lines from more than one total spin state. The population of these different spin states will obey Boltzmann statistics. Because the intensity of the EPR signal is proportional to the population of the state, the variations in temperature may be used to estimate the exchange coupling energy. The energy, E(S), of the total spin states differs by [44]

$$E(S)-E(S-1)=SJ\,. \tag{37}$$

Assuming a Boltzmann distribution of pairs with different spins, the intensity, I(S), of the EPR resonance for each spin state should differ with temperature through the equation given below [44].

$$I(S) \propto \frac{\exp\left(-E(S)/2kT\right)}{\left(\sum(2S+1)\exp\left(-E(S)/2kT\right)\right)}. \quad (38)$$

By using the ratio of the intensities of two spin states, J can be estimated. Eq. (39) shows how to estimate J for total spin states that differ by 1.

$$\frac{I(S)}{I(S-1)} \propto \frac{\exp(-E(S)/kT)}{\exp(-E(S-1)/kT)} = \exp(-SJ/kT). \quad (39)$$

## C. EPR of results

In this section the EPR spectra for $CdGa_2S_4$ and $CdGa_2S_4$:Cr and the centers being studied are described. Then the angular variation of the spectral lines for rotation of the crystals about the (1,1,2) axis is discussed. Next, the angular variations of the EPR resonances being studied are described as the sample is rotated about three different axes. The angular variations in line width and line shape will be discussed after the angular variations. The temperature studies of the spectra are discussed. Last, the relative signal intensity in each type of crystal is described.

### *1. $CdGa_2S_4$ and $CdGa_2S_4$:Cr EPR spectra*

Three types of crystals were analyzed: undoped $CdGa_2S_4$, $CdGa_2S_4$:Cr, and annealed $CdGa_2S_4$:Cr (see Table 1). The EPR for undoped $CdGa_2S_4$ showed no resonances lines. Both the annealed and unannealed doped crystals showed EPR resonances. In all crystals, both doped and undoped, the EPR spectra were sensitive to visible illumination. However, the EPR of samples exposed to visible light will not be addressed in this dissertation. Figure 9 shows spectra of undoped $CdGa_2S_4$ (Kun),

unannealed $CdGa_2S_4$:Cr (K2), unannealed $CdGa_2S_4$:Cr (B1), and annealed $CdGa_2S_4$:Cr (K4A). The set of resonance lines present in all doped samples is the focus of the present investigation. These resonance lines are indicated by a vertical dashed line in Fig. 9.

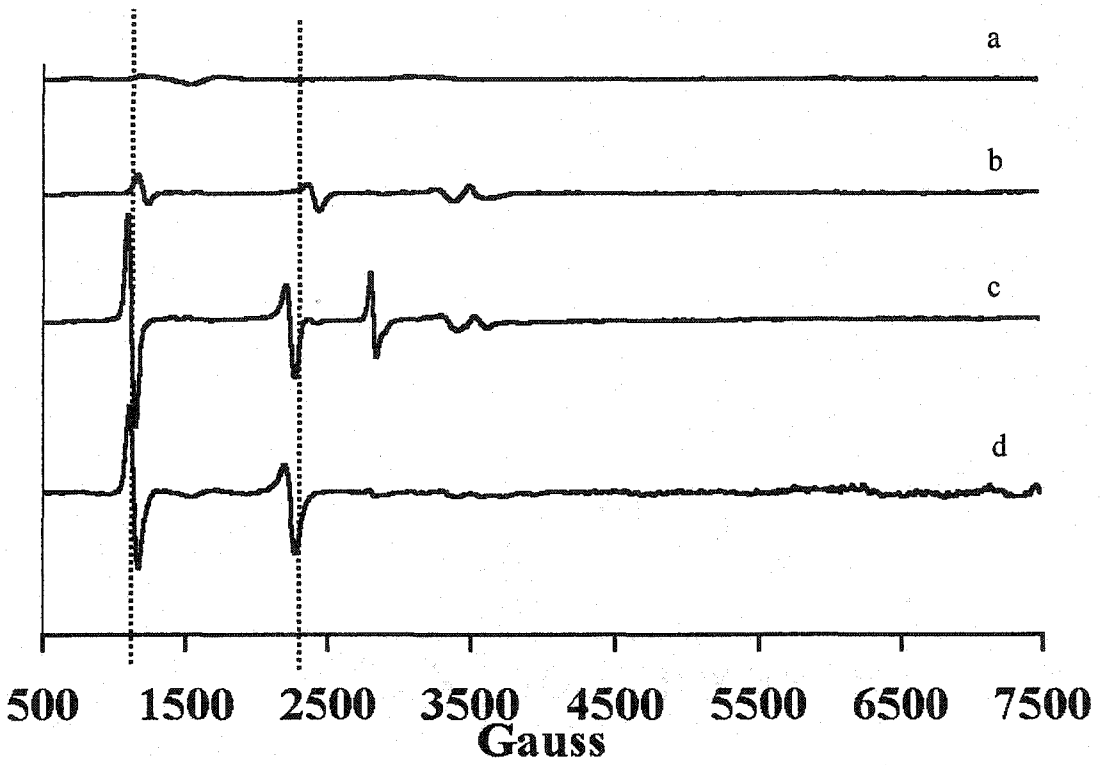


FIG. 9. EPR first derivative spectra at 12 Kof (a) ndoped $CdGa_2S_4$, (b) un-annealed $CdGa_2S_4$:Cr from Kuban State University, (c) unannealed $CdGa_2S_4$:Cr from The BAE Corporation, (d) and annealed $CdGa_2S_4$:Cr.

The paramagnetic center near 3,000 Gauss in crystal B1 from The BAE Corporation is an experimental artifact. This center is from the quartz tube used in the flow through liquid helium low temperature system used only on crystal B1. Additional signals, which we did not study, appear in crystals that have not been annealed and when the crystals are excited by light of energy near the band gap. The center near 3,400 Gauss on the un-annealed sample spectra will appear in both the annealed and undoped sample spectra

after illumination by band to band excitation. Therefore, the center at 3,400 Gauss did not disappear with annealing.

### *2. Angular variation of $CdGa_2S_4$ and $CdGa_2S_4$:Cr EPR spectra rotated about (1,1,2)*

Figure 10 shows the g value of the resonance lines versus angle for crystal K4A as the crystal is rotated about the (1,1,2) axis. The two resonance lines being studied have maximum g values of 3 and 6. The resonance lines being studied are referred to throughout this dissertation as the g=6 line and the g=3 line. The lowest value of *g* that could be determined from experiments is 0.93. Except for angles where the *g* value is close to the detection limit, the *g* values of the g=6 resonance line are twice the *g* values of the g=3 resonance line. For purposes of this discussion, the two resonances are considered related by a factor of 2 throughout the entire angular variation.

The region where the g values are not related by a factor of 2 is near the high magnetic field where the resonance lines are broadest. It is difficult to accurately determine the zero crossing for broad lines. There is also an error associated with the angle of rotation.

For dilute systems, a factor of 2 dependence between resonance lines often indicates a defect system with a spin state of 1. In dilute centers with a spin state of one the resonances at the half value are caused from "spin forbidden" transitions when the magnetic moment of the spin state changes by 2 rather than 1. Because these half-valued transitions are spin forbidden the intensity is usually smaller than the spin allowed transitions. However, the data have two very strong resonance lines; thus, it is not clear that the half-field line results from a spin forbidden transition.

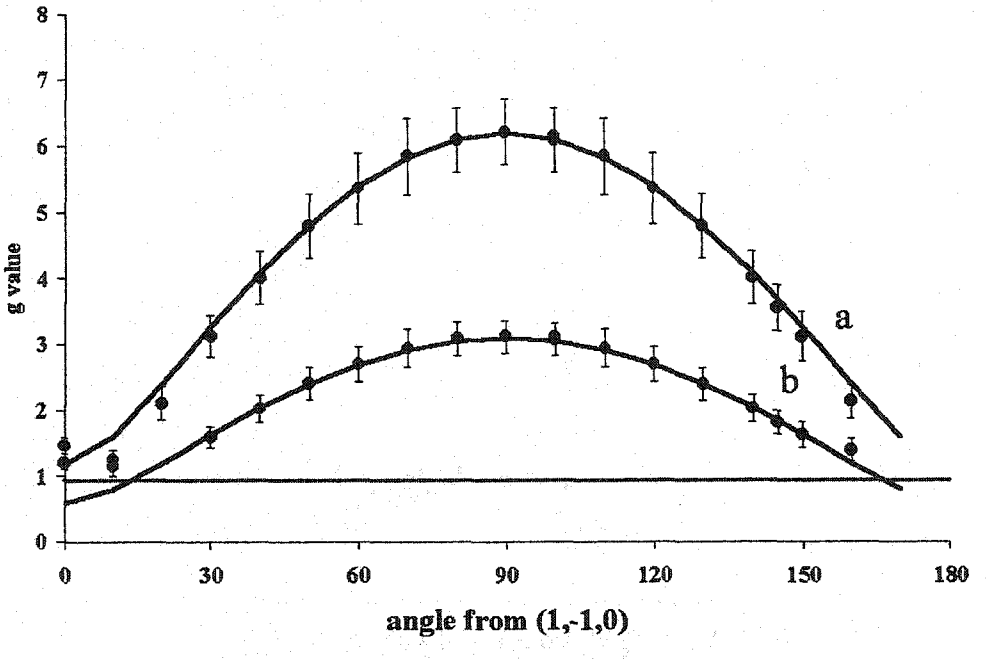


FIG. 10. Angular variation of resonance lines being studied for annealed $CdGa_2S_4$:Cr, crystal K4A, about the (1,1,2) axis. Lines are fitted equation $\sqrt{\left(\left(A\cos(\theta)\right)^2+\left(B\sin(\theta)\right)^2\right)}$, for (a) A=1.2, B=6.2 and (b) A =0.6, B =3.1.

In exchange coupled systems the dipole-dipole interaction should be greatest for the broadest lines. Because the dipole-dipole interactions influence the *D* tensor of Eq. (22), exchange coupled systems will experience a change in the Hamiltonian because of dipole-dipole interactions. For an exchange coupled system in the strong exchange regime, the dipole-dipole interactions will be a perturbation to Eq. (13). The variations from a factor of two relationship near the extremely low values of *g* could be caused by the effects of dipole-dipole interactions on the exchange system.

Examining Fig. 10 reveals a large anisotropy in the *g* values of these resonance lines. Transition metal ions doped in crystals may have a large *g* value anisotropy [35]. Because chromium is expected to substitute in $CdGa_2S_4$ in a tetrahedral environment, it is reasonable to expect that the EPR spectra for Cr in $CdGa_2S_4$ will be similar to the EPR

spectra for Cr in CdS. Initially, $Cr^{2+}$ in CdS was modeled with an effective spin of one half and a g tensor with $g_{//}$ equal to 7.75 and $g_{\perp}$ approximately equal to zero [46]. These values are similar to the coefficients fit to the g=6 line, leading us initially to think this resonance peak could be from $Cr^{2+}$ in $CdGa_2S_4$.

Drawn in Fig. 10 is a fit to the function for an axially symmetric center, Eq. (17), with $g_{//}$=A and $g_{\perp}$=B, for coefficient values A=1.2, B=6.2 9 (a) and =0.8, B=3.2 (b). For axially symmetric centers, θ is the angle between the axis of symmetry of the defect and the applied magnetic field. The angle measured in the laboratory corresponds to the angle theta when the axis of symmetry is in the rotation plane of the sample. If the sample is rotated about a different axis, the angle measured in the laboratory is no longer the angle between the axis of symmetry and the applied magnetic field. For axially symmetric centers, the shape of the curve describing the angular variation of g values will change with differing rotation axes.

The data in Fig. 10 fit the function for an axially symmetric center with the laboratory angle, implying that the defect axis lies in the plane of the applied magnetic field. Within experimental error, Fig. 10 is the angular variation of *g* expected for angular rotation of the sample with the axis of symmetry in the rotation plane. However, for reasons explained in the next section, I do not believe the (1,1,2) axis corresponds to the symmetry axis for an axially symmetric system. The A and B coefficients do not correspond to values of $g_{//}$ and $g_{\perp}$.

### *3. Angular variation of $CdGa_2S_4$:Cr EPR spectra rotated about different axis*

To unambiguously determine the type of symmetry in the defect, the defect is rotated about three different axes. When the axis of symmetry is no longer in the rotation plane, the angle measured in the laboratory does not equal the angle theta in Eq. (17). The laboratory angles will be related to the angle theta by applying the appropriate rotation matrix [35]. Figures 11-13 show the angular variation of $g$ in three additional axis of rotation for the centers being studied in $CdGa_2S_4$:Cr.

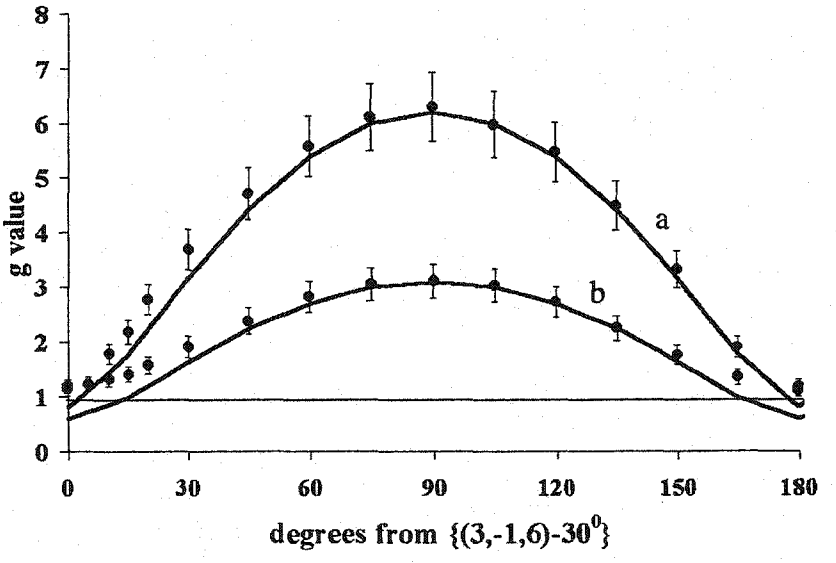


FIG. 11. Zero crossings of a $CdGa_2S_4$:Cr crystal from BAE Corporation rotated about the (3,2,3) axis. Angles are from the (3,-1,6) – $30^0$. Lines are fitted equation $\sqrt{\left(\left(A\cos(\theta)\right)^2+\left(B\sin(\theta)\right)^2\right)}$, for (a) A=1.2, B=6.2 and (b) A=0.6, B=3.1.

The data can be fit in all three additional rotation axes with the same equation for rotation about the (1,1,2) by using the laboratory angles in each of the three additional rotation axis, which is not consistent with a simple dilute system. Therefore, it is believed that the system is a collection of defects in which the g value is averaged.

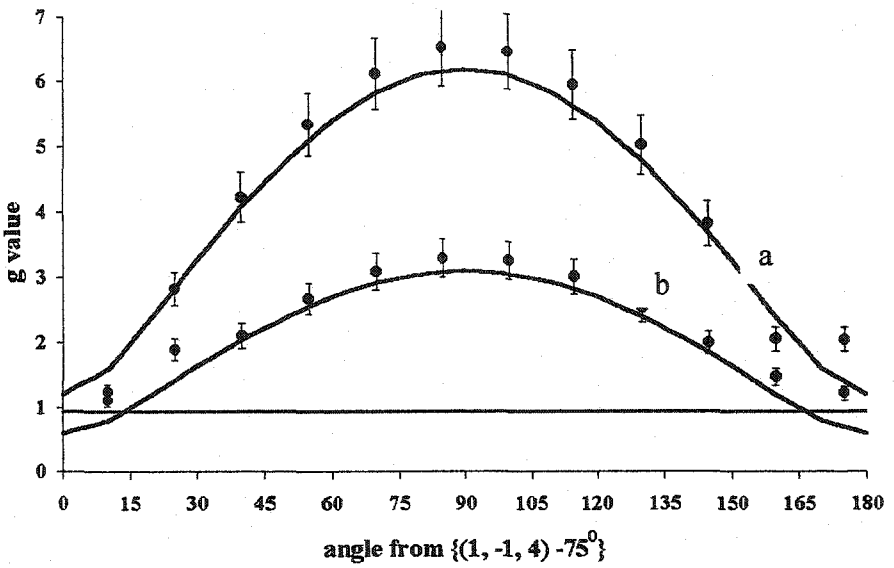


FIG. 12. Zero crossings of $CdGa_2S_4$:Cr crystal K4 rotated about the (2,2,-7) axis. Angles are from the (1,-1,4) – $75^0$. Lines are fitted equation $\sqrt{\left(\left(A\cos(\theta)\right)^2+\left(B\sin(\theta)\right)^2\right)}$, for (a) A=1.2, B=6.2 and (b) A=0.6, B=3.1.

For exchange narrowed systems the g values are determined by the average of all *g* values associated with the interacting centers. In the exchange narrowed regime each paramagnetic center will change *g* values as the rotation axis of the crystal is varied. However, it is not unusual for the average of the interacting centers to be almost the same as a crystal is rotated about several different axes. Because the *g* value as the crystal is rotated is the average *g* value in each plane, determining the manner in which an exchange coupled system varies requires an advanced knowledge of the individual *g* tensors for each of the centers involved in the coupling. Conversely, it is impossible to determine the individual centers $g_{\perp}$ or $g_{//}$ values from different rotation axes of an exchange narrowed system unless some prior knowledge of the individual centers exists [45]. Because no previous EPR analysis has been done on these crystals, the symmetry of the center may not be determined.

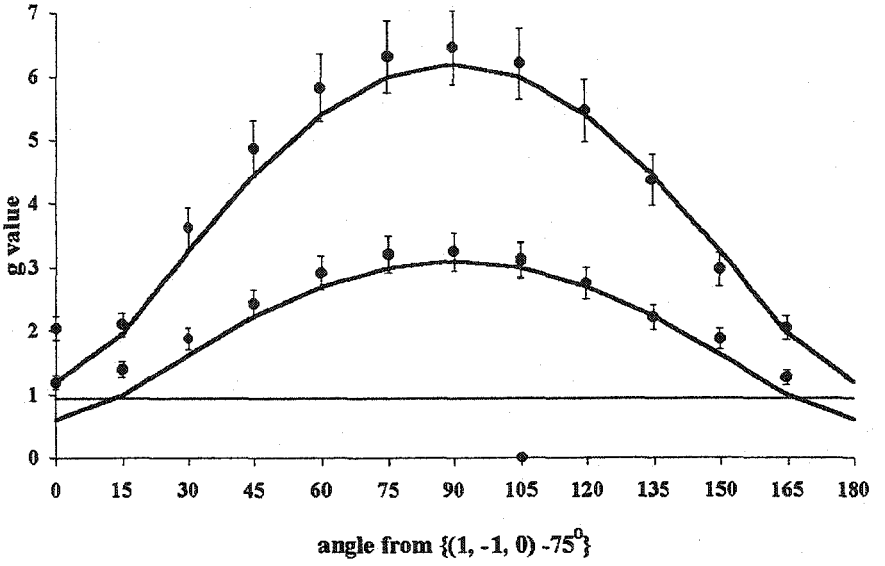


FIG. 13. Zero crossings of a $CdGa_2S_4$:Cr crystal K4 rotated about the (0,0,1) axes. Angles are from the (1,-1,0) - $75^0$. $\sqrt{\left(\left(A\cos(\theta)\right)^2+\left(B\sin(\theta)\right)^2\right)}$, for A =1.2, B =6.2 (a) and A =0.6, B =3.1 (b).

### *4. Angular dependence of line width of $CdGa_2S_4$:Cr EPR spectra*

Figure 14 shows the peak to peak line width variation, $\Delta B_{pp}$, for crystal K4A as a function of angle. The center peak fits fairly well to Eq. (33), with an A value of 50 and a B value of 135, which is shown on the graph. The constant 50 corresponds to an isotropic line width for the center. Equation (33) is the equation expected for angular variation of the line width caused solely by dipole-dipole interaction. In a solid there are several mechanisms for line width broadening in addition to dipole-dipole interactions. The line widths for exchange coupled systems often vary from the equation for dipole-dipole interactions due to additional broadening mechanisms, especially at the second peaks near plus and minus 90 degrees [44]. Shallow effective mass acceptors often exhibit an angular variation of the resonance line width. No functional form for the angular change in line width of a shallow acceptor in $CdGa_2S_4$ has been predicted.

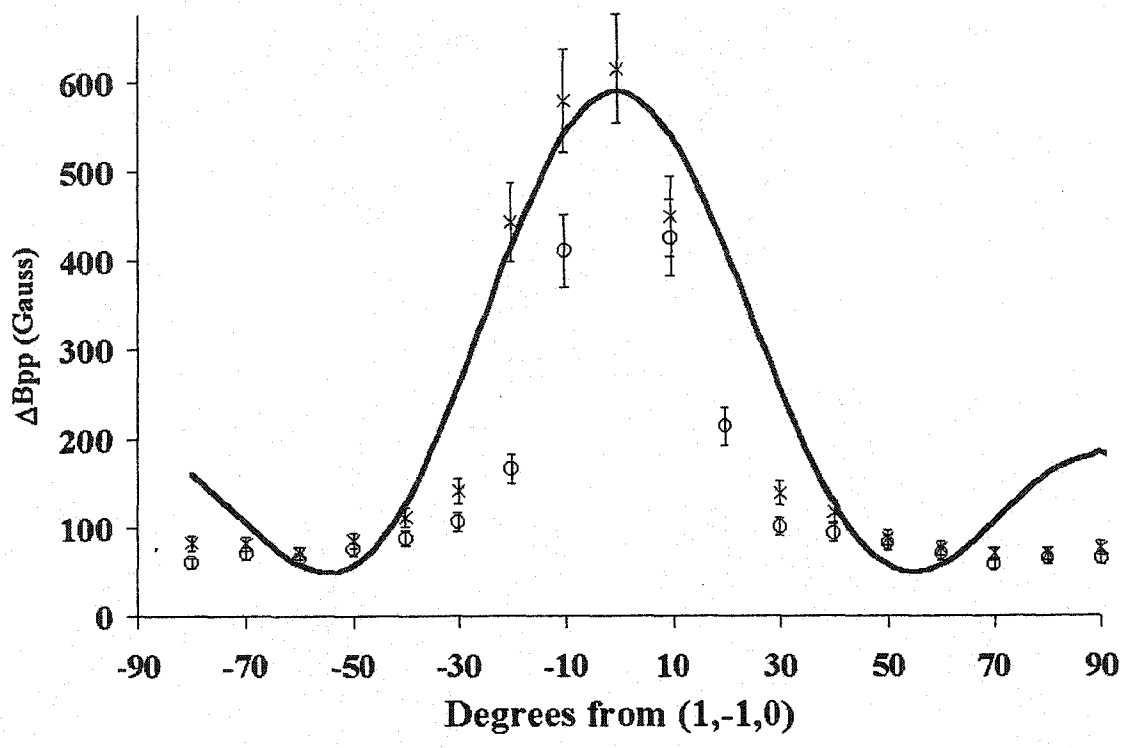


FIG. 14. EPR resonance line width variation with angle about rotation axis (1,1,2) for crystal K4A. Solid line represents a fit to the equation $50+135\left(3\cos(\theta)^2-1\right)^2$.

*5. Line shape analysis of $CdGa_2S_4$:Cr EPR spectra*

The line shape of the resonance lines was analyzed by using the method described in Appendix A. The EPR resonances were entirely Lorentzian for the narrower line widths. As the line widths became larger, the line shape became more Gaussian. Nonetheless, the resonance line shape for broader line width was still Lorentzian near the center of the resonance. This variation in angular line shape is exactly what is expected for exchange coupled systems [44]. For shallow acceptor in $CdGa_2S_4$ the type of line shape and the variation of the line shape with angle have not been predicted.

### *6. Line shape analysis of $CdGa_2S_4$:Cr EPR spectra*

The line shape of the resonance lines was analyzed by using the method described in Appendix A. The EPR resonances were entirely Lorentzian for the narrower line widths. As the line widths became larger, the line shape became more Gaussian. Nonetheless, the resonance line shape for broader line width was still Lorentzian near the center of the resonance. This variation in angular line shape is exactly what is expected for exchange coupled systems [44]. For shallow acceptor in $CdGa_2S_4$ the type of line shape and the variation of the line shape with angle have not been predicted.

### *7. Temperature dependence of $CdGa_2S_4$:Cr EPR spectra*

The temperature dependence of the EPR resonance lines was determined by taking scans at 200 K, 100 K, 50 K, 20 K, and 11 K. Figure 15 illustrates the spectra of $CdGa_2S_4$:Cr taken at one angle for different temperatures. Temperature studies of these two centers showed that the resonance peaks existed from 4 K to 200 K. Sample data were not taken above 200 K or below 4 K. No additional resonance lines were found in EPR spectra at any of the temperatures studied. Figure 15 illustrates how the EPR resonance spectra change with temperature for crystal K4. In Fig. 15 all spectra have been Boltzman normalized to 12K. No change in $g$ values or line width occurred as the temperature was lowered. The lack of variation in $g$ values and line width implies that an exchange system is composed of a few atoms and not a chain.

Figure 16 shows the integrated signal intensity after correction for the temperature dependence of the Boltzmann distribution for crystal K4. The integrated signal intensity of these resonances has a very large error. The resonances shown in Fig. 15 have the most narrow line widths and most Lorentzian line shape seen in $CdGa_2S_4$:Cr. It can be

seen that there is a shoulder on the resonance lines, which makes it difficult to determine exactly where the integration should begin. By varying the initial and final points of integration to include or exclude portions of the shoulder on the resonance lines, the total signal intensity could be varied by a factor of two. The error bars on Fig. 16 reflect this

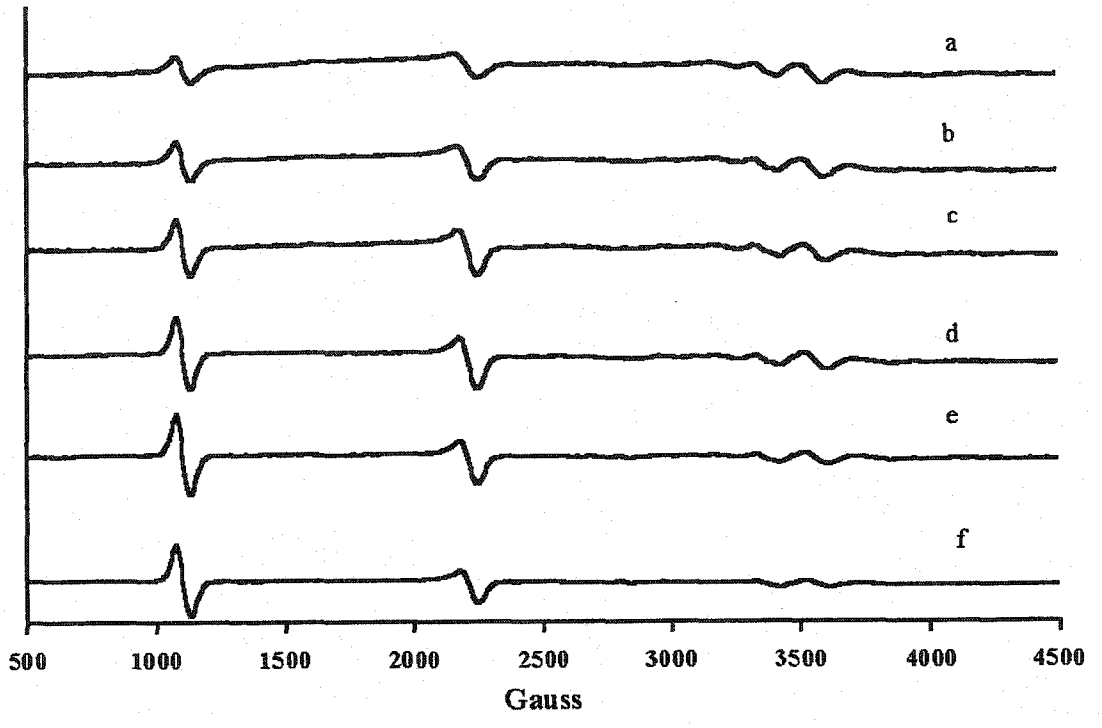


FIG. 15. EPR resonance spectra at (a) 200 K, (b) 150 K, (c) 100 K, (d) 50 K. (e) 20 K, and (f) 12 K normalized for Boltzmann factor to 12 K for crystal K4.

error. Double integration of the resonance peaks at 200 K has significant associated error because the resonance spectrum for 200 K has very small peaks. Although the total integrated intensity of the resonance spectra at 200K is presented, the data at 200K are not used in the analysis of temperature effects.

If the EPR lines from defects in an exchange coupled system arise from two different spin states, the isotropic exchange coupling constant, J, may be determined from

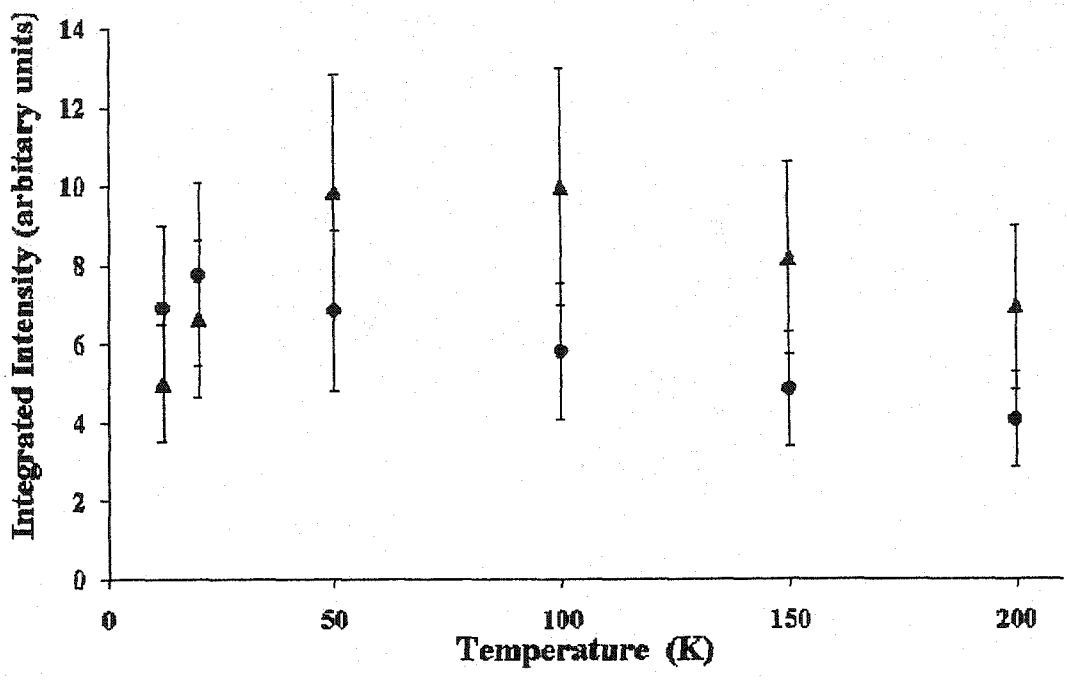


FIG. 16. Intensity of EPR signal determined by double integration of first derivative spectra Boltzmann normalized to 12 K for $CdGa_2S_4$:Cr crystal K4. The g=3 center is denoted by •, and the g=6 center is denoted by ▲.

the temperature dependence of the ratio of the intensities of each spin state. By taking the natural logarithm of Eq. (39) the relationship below is found, with A being the proportionality constant of Eq. (39).

$$\ln\left(\frac{I(S)}{I(S-1)}\right) = \ln(A\exp(-SJ/kT)) = A' - \frac{SJ}{kT}. \tag{40}$$

From plotting the log of the ratio of total spin state intensity against the inverse temp-erature, a straight line may be fit to the data. The fit line will have a slope that is related to the exchange constant.

By assuming the two resonances in the data reflect two different total spin states of the same defects, Eq. (40) can be used to estimate $J$ for $CdGa_2S_4$:Cr. Figure 17 shows the plot of the log of the ratio of the intensity of the g=6 resonance to the g=3 resonance

versus inverse temperature. It is assumed that the two resonances correspond to total spin states of one (g=6) and two (g=3) for these calculations, which allow an estimate of the magnitude of the isotropic exchange constant *J*. Analysis of data from crystal K4 and K4A yielded *J* values of 4±2 $cm^{-1}$ and 3±2 $cm^{-1}$, respectively. X-band microwaves used in the EPR system have energy of 0.31$cm^{-1}$. The value for *J* determined above places the spectra in the strong exchange regime. Further analysis shows that a strong exchange regime will persist under the assumptions of spin states as high as 38.

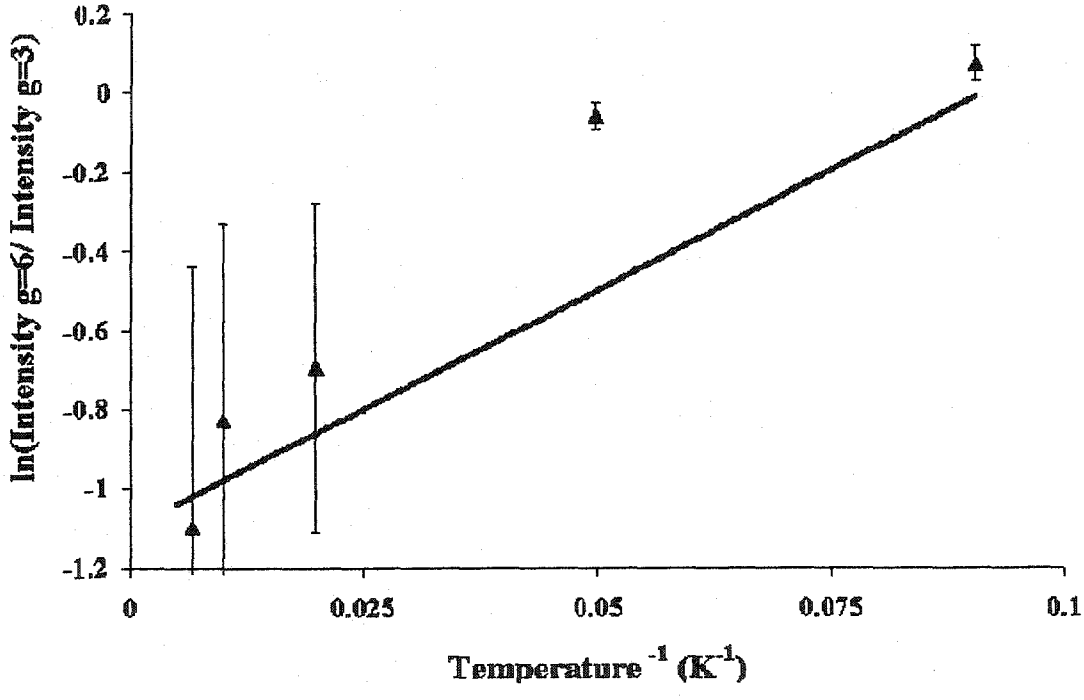


FIG. 17. Temperature dependence of the ratio of resonance intensity for unannealed $CdGa_2S_4$:Cr. The line is a best fit to Eq. (40) with SJ/K equal to -12 and A' equal to 0.5.

The error associated with the determination of *J* was found by varying the best fit line. The lines with greatest and least slopes that could be drawn provided the error. It should be noted that this analysis is based on a best fit line to data on K4 and K4A that

consisted of only five and four data points, respectively. To reduce the error more data points would need to be taken.

The experimentally determined value of J is large enough to place the EPR data in the strong exchange regime. The value of the exchange interaction depends on how greatly the host lattice and defect interact. For transition metal ions reported values for the exchange constant *J* vary greatly. Nearest neighbor $Cr^{3+}$ pairs in ruby have been reported to have an exchange constant equal to 385 $cm^{-1}$ [47]. Manganese pairs in CdCl and CdBr have been reported with exchange constants of 1.43 $cm^{-1}$ and 1.33 $cm^{-1}$, respectively [48].

Figure 18 shows the resonance spectra for the centers being studied at both 12 K and 4 K, with the spectra Boltzmann normalized to 4 K. The g=6 resonance increases in

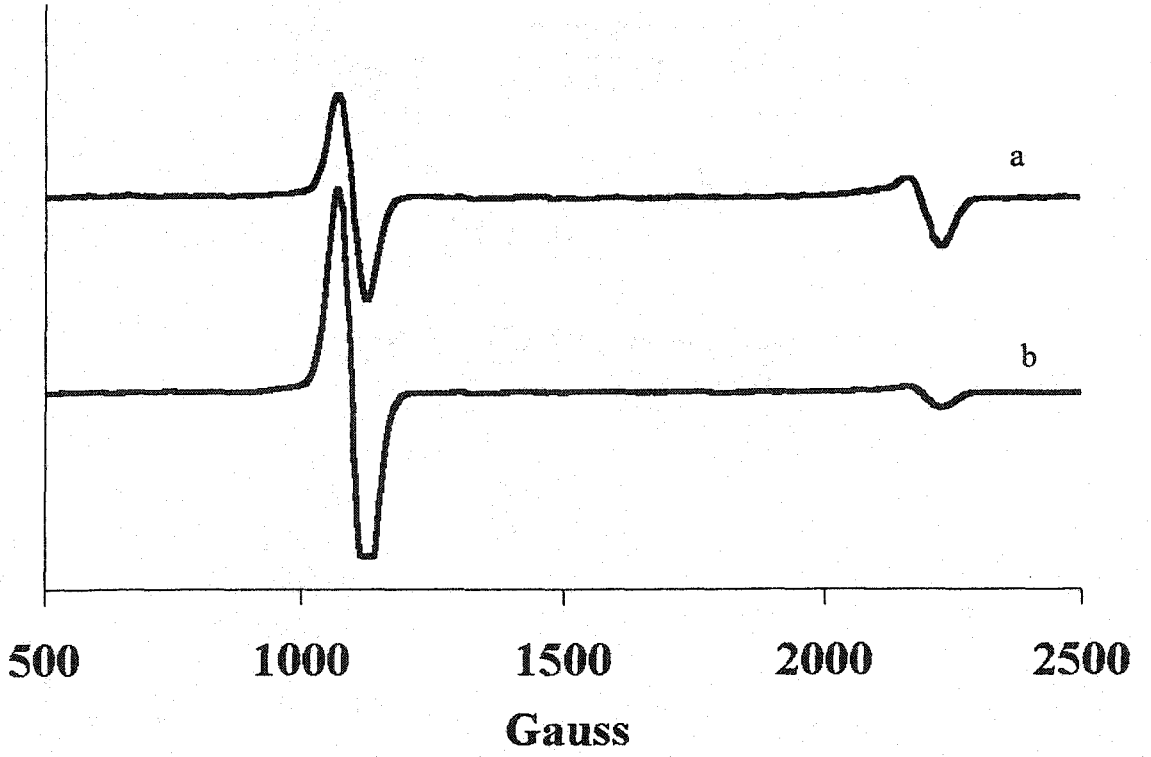


FIG. 18. EPR spectra at 12K (a), and 4K (b) for crystal K4 rotated about (1,1,2) axis. Both plots were normalized to 4K

size, corresponding to an increase in the number of centers in the g=6 resonance at 4 K. The g=3 resonance decreases in size, corresponding to a decrease in centers in the g=3 resonance at 4 K. As discussed earlier, if the resonances result from an exchange narrowed system, there could be more than one spin state. As the temperature is lowered, the distribution of the exchange system spin states will go to the ground total spin state. For exchange coupled paramagnetic centers, Fig. 18 indicates the g=6 signal is a ground state for the system.

### *8. Signal Intensity*

Table 4 lists the relative signal intensity for the EPR resonance peaks and the doping level of the crystal for the crystals K2, K3A, K4, K4A, and B1. The intensity of

TABLE 4. Relative number of centers in EPR resonance.

| Crystal | Signal Intensity referenced to K2 ($10^{17}$ centers/cm$^{-3}$) | | Cr doping level in melt ($10^{19}$ atoms/cm$^3$) |
|---|---|---|---|
| | g=6 | g=3 | |
| K2 | 1.0±0.5 | 1.0±0.5 | 6.0 |
| K3A | 1.3±0.6 | 2.0±1.0 | 6.0 |
| K4 | 0.9±0.5 | 1.2±0.5 | <6.0 |
| K4A | 5.8±3.0 | 3.8±2.0 | <6.0 |
| B1 | 8.0±4.0 | 17.0±9.0 | 1.0 |

the signal may be related to the number of centers in these crystals by comparison with a known standard, as outlined in Chapter 2. Assuming uniform distribution of dopant, a comparison of the signal intensity of the resonance lines being studied in $CdGa_2S_4$:Cr

with the signal intensity of the Si standard determines that the crystal doping level is on the order of $10^{17}$-$10^{18}$ centers per $cm^{-3}$. The concentration of defects is not sufficient to cause nearest neighbor interactions between the defect centers unless the defects are nonrandomly distributed. The number of centers is 1 to 2 orders of magnitude less than the doping level of chromium. The chromium doping level listed is the amount of chromium doped into the melt. Not all of the chromium in the melt may have been incorporated into the crystal lattice.

## D. Discussion

$CdGa_2S_4$:Cr shows two EPR resonances in all crystals. The research presented here focuses on these two resonance lines. The resonance lines studied show large anisotropy in g values and line widths. Shallow mass acceptors exhibit g value and line width anisotropy in EPR experiments. The angular variation of the two resonance lines may be fit to the same equation for axial symmetry with the same coefficients in all axis of rotation, and using $\theta$ equal to the angle measured in the laboratory for every axis of rotation. The angular variation of the line width was compared with the theoretical function for broadening caused by dipole-dipole interactions. The line width variation was consistent with the central region of the function for the angular variation of dipole-dipole broadening. The line shape of the resonance lines was analyzed and found to be Lorentzian at the narrowest line width. As the line width increased the line shape became increasingly Gaussian. The line shape is the most Gaussian at the largest line width. The temperature studies of the resonance lines showed no shifts in line width, line shape, or g values.

The EPR experimental results have traits consistent with a cluster of defects and an effective mass acceptor. A cluster of defects will interact with each other. In the EDXS experiments there was no indication of clumping. If a uniform distribution is assumed, comparison of the signal size with a known standard did not show a defect concentration large enough for the defects to be nearest neighbors. An exchange system involving superexchange can allow defects to interact without clumping. For an ODC, the DA pairs are present every few unit cells. A dopant atom incorporated into an ODC will always be within a few unit cells of a DA pair. Even at a low concentration, a dopant atom in an ODC will always be close enough to an ODP to interact with the ODP through a superexchange mechanism.

As shown in Fig. 8, in an exchange narrowed system the resonance lines will be at the average $g$ value of the centers involved. The average of the $g$ values may not change appreciably as the rotation axis is varied. Therefore, the existence of two resonance lines that have the same angular dependence in every rotation axis can be explained by an exchange narrowed system.

Analysis of the line width variation with angle showed that the central peak is consistent with dipole-dipole broadening. Because there is generally more than one type of EPR line width broadening that occurs in solids, the greatest variation between data and dipole-dipole fit is near the wings of the function for angular variation dipole-dipole interactions. Exchange narrowed resonance lines will experience dipole-dipole broadening and are expected to have large variations in line width.

The exchange narrowed lines have their line shapes theoretically determined to be Lorentzian at the narrowest line width. As the line width of the resonances increases, the line shape of an exchange narrowed resonance will become more Gaussian. The widest

resonance will have the most Gaussian nature in an exchange narrowed resonance, which is exactly what was seen in the spectra.

The temperature studies of the resonance lines showed no shifts in line width or *g* values. Exchange coupled systems that exist in chains will have shifts in line widths and *g* values as the temperature is lowered below a critical point. The temperature data support the belief that the exchange occurs between a small number of defects, possibly a dimer.

Analysis of the change in the ratio of signal intensity between the two resonance lines with temperature determined an experimental value for the isotropic exchange constant *J*. For crystal K4 the isotropic exchange constant was determined to be 4.±2. $cm^{-1}$. For crystal K4A the experimentally determined value for the isotropic exchange constant was 3. ± 2. $cm^{-1}$. This analysis assumes the g=3 line has a total spin state of 2 and the g=6 resonance has a total spin state of 1. The experiments used x-band microwaves that have energy of 0.31 $cm^{-1}$. The experimentally determined exchange constant is large enough to place the experiments within the strong exchange regime. By using Eq. (40) and the greatest value of experimentally determined exchange constant, two total spin states with values of 37 and 38 can be assumed and still keep the experiment in the strong exchange regime. For an exchange coupled system between a small number of centers such as a dimer, it is unlikely to have a total spin state greater than 38.

Effective mass like acceptors may exhibit angular variations in line width and line shape. The forms of the angular variation in line width and line shape for an effective mass acceptor in $CdGa_2S_4$ are unknown. Effective mass acceptors may exhibit angular variations of *g* values that were seen in EPR experiments, but only for one rotation axis.

An effective mass acceptor in a dilute system will not have the same angular variation in all axes of rotation

$CdGa_2S_4$ has a high number of native neutral defects. In $CdGa_2S_4$ both cadmium and gallium are only bonded to sulfur. Sulfur is a large atom. In $CdGa_2S_4$ sulfur has a nonbonding orbital. The nonbonding orbitals of sulfur are directed toward each other to create a two-dimensional lattice within $CdGa_2S_4$ that is high in electron density. A positive charge, or hole, in this lattice will be surrounded by eight electrons. Although no calculations have been done, based on Coulombic interactions of the electrons, it should be energetically favorable to place positive charge, or hole, in the middle of the non-bonding sulfur orbitals.

Previous analysis of $CdGa_2S_4$:Ag used TSL, TSC, and PL studies. These studies suggest that the Ag serves as an acceptor, and that Ag forms a short range complex with one of the trapping defects noted in undoped $CdGa_2S_4$ [22]. The EPR results may be interpreted as an acceptor in an exchange coupled system with a defect. Because the exact nature of the native defects in undoped $CdGa_2S_4$ is not known, a model for the center being studied in the EPR experiment may not be determined. However, one possibility is that chromium acts as an acceptor in $CdGa_2S_4$ that is exchange coupled to native defect on a sulfur atom. Another possibility is that the cation lattice contains defects similar to those defects seen in $CuInSe_2$, and that the chromium interacts with defects in the cation sublattice.

# CHAPTER 5

## OPTICAL INTERACTIONS

Optical studies of $CdGa_2S_4$ have mainly focused on the undoped material and the visible region of the spectra because $CdGa_2S_4$ is transparent from 450 nm to 13 μ. $CdGa_2S_4$ has a birefringence coefficient larger than $LiNb_3$, which changes sign in the visible region of the electromagnetic spectrum [24,49]. The band structure and phonon absorption of $CdGa_2S_4$ have been described [50]. Fluorescence studies have been done on $CdGa_2S_4$:Ag and $CdGa_2S_4$:In. Absorption studies of $CdGa_2S_4$:Co show a symmetry of $S_4$ with effects from spin-orbit coupling [25]. No absorption or fluorescence spectra are available for $CdGa_2S_4$:Cr in the scientific literature.

Our optical studies focused on describing the absorption and fluorescence of $CdGa_2S_4$:Cr. In semiconductors such as $CdGa_2S_4$, the energy levels associated with absorption or emission occur from many different mechanisms such as crystal lattice vibrations, interband transitions, intraband transitions, transitions within DA pairs, hydrogenic levels associated with acceptors, excitonic absorption, and energy levels associated with dopant ions. These mechanisms work in a competitive manner, with one or two generally dominating the absorption or fluorescence spectra. However, the mechanisms that dominate the absorption spectra may not be the same mechanisms that dominate the fluorescence spectra. The following sections will discuss the rudiments of these mechanisms and their different characteristics of absorption and fluorescence. The chapter then reviews the results for the absorption and fluorescence of $CdGa_2S_4$:Cr.

## A. Absorption mechanisms

### *1. Crystal lattice vibrations*

Although crystals exist with a defined structure, or lattice, the atoms are not static. The atoms and electrons will vibrate slightly around the lattice points. The electronic wavefunction is coupled to the lattice ions. As the lattice ions are displaced from their equilibrium position, the electronic wavefunctions will be deformed. In describing the crystal potential both the adiabatic and harmonic approximations are generally adopted. The adiabatic approximation is built on the difference in mass between an electron and an ion. The differences in mass will yield different velocities for the ion and electrons. The typical electron velocity is approximately $10^8$ cm/s [40]. The typical ion of the crystal lattice has a velocity of approximately $10^5$ cm/s [40]. Because the ions of the crystal lattice move 3 orders of magnitude slower than the electrons, the change at any instant in the ionic potential experienced by an electron will be negligible. It may be assumed that the deformations to the electronic wavefunctions caused by the displace-ment of the ions in the crystal lattice at any given instant may be treated as perturbations to the ground state wavefunction [40]. Therefore, any interactions with electrons in a solid may assume the electrons are in a ground state with respect to the instantaneous ionic lattice configuration. The harmonic approximation assumes that deviations from equilibrium positions are small [40]. This assumption allows the potential energy of interatomic interactions to be expanded about the equilibrium positions. The first non-zero term in the Taylor expansion is the second order term, which creates a Hamiltonian with the same terms as a mass attached to a spring [40].

The harmonic approximation essentially reduces the problem of determining ionic motions within a solid to the quantum harmonic oscillator. The resulting normal modes

of vibrations found by solving the appropriate Schrodinger equation are referred to as phonons [40]. The phonons of a crystal lattice may be in either optical or acoustical modes. The optical modes in a crystal have wavelengths long enough to interact with electromagnetic radiation. The optical branches are characterized as either longitudinal, for vibrations that are polarized parallel to the wavevector, or transverse, for vibrations perpendicular to the wavevector [40]. The frequency of lattice vibrations is often in the IR region of the electromagnetic spectrum. Phonon absorption bands for chalcopyrites have shown absorption in the IR [51].

### *2. Vibronic, direct, and indirect transitions*

Absorption or emission of radiation from electronic transitions within the energy levels of an individual atom occurs with electromagnetic energy equal to the energy difference between the initial and final states of the electron. In solids the energy difference between the initial and final electron energies may or may not equal the energy of the emitted or absorbed electromagnetic radiation. At any given time a solid will contain phonons of wavevector, $\mathbf{k}_p$. The phonons in a crystal may be defined in terms of the occupation number, $n_k$, which is the number of phonons with wavevector $\mathbf{k}_p$ that are present in the crystal [40]. The crystal momentum, $\mathbf{p}_c$, is defined as

$$\mathbf{p}_c = \hbar\mathbf{k}_p . \tag{41}$$

The crystal momentum defined in this way is not associated with the momentum of the lattice ions. Total crystal momentum is conserved in any transition to within ħ times a reciprocal lattice vector, $\mathbf{k}$ [40].

Electrons and phonons may interact. Energy may be transferred between the electrons and phonons [40]. For this reason, it is possible for electronic transitions

between energy levels in a solid to emit radiation of energy not equal to the energy difference in the levels. The electromagnetic radiation emitted during a transition may equal the energy difference between the two energy bands in the solid plus or minus the energy of one or some integral number of phonons. These types of transitions are often referred to as vibronic or phonon assisted transitions. In fluorescence studies vibronic spectra show a series of lines corresponding to the integer multiples of phonons. Figure 19 represents an idealized spectrum for vibronic fluorescence. In Fig. 19 the energy of a phonon is p.

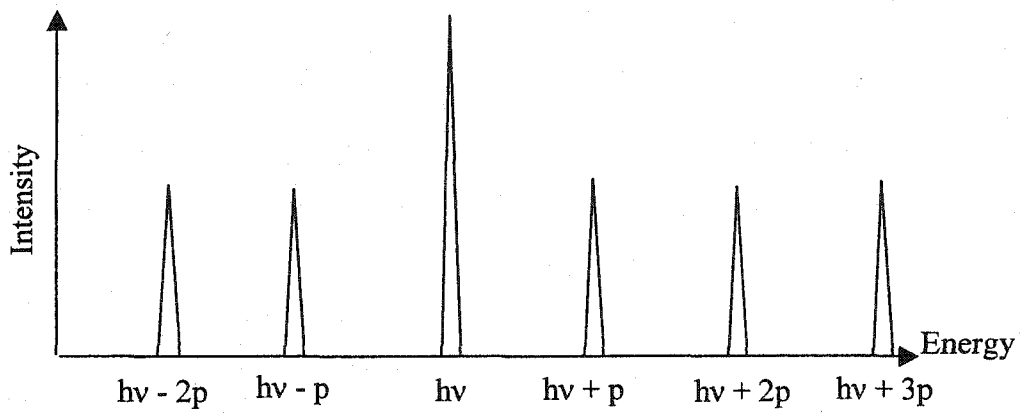


FIG. 19. Idealized vibronic fluorescence of a crystal with phonon energy of p.

The large peak in the center of the graph corresponds to the difference between the two energy levels when no phonons are created or destroyed and is referred to as the zero phonon line. At higher temperature the peaks become wider, and a vibronic fluorescence spectrum will show a central line flanked by broad unstructured fluorescence bands. As the temperature is decreased, the phonons available to be absorbed are decreased. Below a critical temperature, which varies with material, there will not be enough phonons in the material for the fluorescence accompanied by absorption of

phonons to be detected. Because the fluorescence lines at energy greater than the zero phonon line correspond to the creation of a phonon in the material, these lines will remain at low temperature. These effects combine to yield a low temperature vibronic spectrum that is dominated by the zero phonon line and lines that correspond to the creation of phonons [52].

For semiconductors, optical transitions may occur between the conduction and valence bands. If the conduction band minimum and the valence band maximum occur at the same position in reciprocal space, the optical transitions are called direct transitions. If the energy minimum of the conduction band and the energy maximum of the valence band occur at different points in reciprocal space, the phonons of the semiconductor may provide the crystal momentum to the electron which is necessary for the electron to transition between the valence and conduction bands. These phonon assisted transitions are called indirect transitions. Figure 20 illustrates the direct and indirect transitions in semiconductors [40].

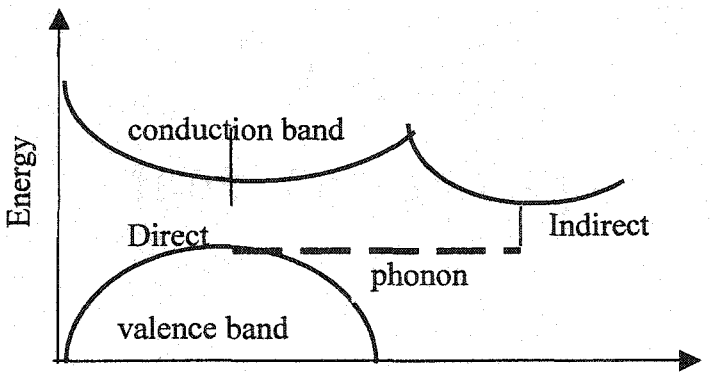


FIG. 20. Direct and indirect transitions between the conduction and valence bands of a crystal.

### *3. Donors and Acceptors*

Defects within a solid may be characterized as donors or acceptors, depending on whether the defects typically donate an electron to or accept an electron from an energy band. Acceptors in tetrahedrally coordinated semiconductors have been shown to bind electrons from valence bands and may form a hydrogenic system. The electrons may be excited within this hydrogenic state to yield narrow, discrete absorption lines similar to the lines expected from hydrogen.

There may be several differences between the atomic hydrogen absorption series and the series observed by a hydrogenic system within a solid. The absorption spectra may have additional lines not present in the absorption of hydrogen. The extra lines occur if the symmetry of the crystal is lowered from tetrahedral. These additional lines result from the removal of degenerate levels [28]. Also, for hydrogenic systems in solids, the wavelengths of the hydrogen series may be shifted by a constant, as shown below.

The wavelength for the absorption of hydrogen depends inversely on the Rydberg constant, R, defined below, where m is the mass of the electron, $\varepsilon_0$ is the dielectric constant, e is the electron charge, c is the speed of light, and $\hbar$ is Planck's constant.

$$R = me^4 / 64\pi c \varepsilon_0^2 \hbar^3 \tag{42}$$

In the crystalline lattice this constant will be shifted from the Rydberg constant for hydrogen by the effective mass of the electron and the dielectric constant of the crystal. The effects of the crystal lattice shield the electron of a hydrogenic acceptor from the full interaction the electron would have with the acceptor if the acceptor were not in the solid. This shielding is approximated by using an effective mass for the electron. The effective mass of an acceptor in $CdGa_2S_4$ is not known. For semiconductors the effective mass of

an acceptor is generally about 0.2 times the mass of the electron. The index of refraction, n, is 2.498 for $CdGa_2S_4$ in the visible region [53]. In general n is a complex number. There are no experimental data for the complex index of refraction in $CdGa_2S_4$. This analysis will approximate the complex index of refraction as zero. The dielectric constant of a material is the square of the index of refraction, which yields a dielectric constant of 6.25 for $CdGa_2S_4$ [54]. With these values for effective mass of an electron and the dielectric constant, it is expected that the wavelengths of the hydrogen series will be shifted by the multiple 200. This constant would shift all of the hydrogen series out of the range of the instrument.

*4. DA pairs*

DA pairs may exist within solids. Solids with DA pairs are charge compensated when the pairs exist in the solid as $D^+$ and $A^-$. Because the donor and acceptor are oppositely charged, they will experience a Coulombic attraction of energy, E. The Coulombic attraction will depend on dielectric constant ε and the characteristic length of the DA pairs, R, which is determined by the crystal lattice parameters [52].

$$E = e^2 / R\varepsilon. \tag{43}$$

The donor or acceptor creates an additional energy level within the energy band. The energy level for the donor is referred to as $E_d$, and the energy level of the acceptor is referred to as $E_a$. Under optical excitation the charge compensated pairs may have both the donor and acceptor neutralized. As the crystal returns to equilibrium the electrons on the neutral donors recombine with the holes on the neutral acceptors and emit radiation of frequency υ [52] such that

$$h\upsilon = E_g - E_a - E_d + {e^2}/{R\ \varepsilon} \tag{44}$$

Equation (44) is valid when the characteristic length between the DA pairs, R, is much greater than the crystal lattice parameters. Within the crystal each donor or acceptor may be viewed as interacting with the nearest acceptor or donor, as well as with more distant acceptors or donors. Because the characteristic length between the interacting donor and acceptor will vary, there will be several discrete values of Coulombic attractions for the pair. As donors and acceptors combine, the emission spectrum will show a series of transitions that correspond to the different R between the pairs.

$CdGa_2S_4$ has shown all of the properties of ODP that were noted in the Introduction for $CuInSe_2$ [16,21,26]. Because ordered DA pairs have been observed in chalcopyrites, it is reasonable to expect that such a structure could exist in defect chalcopyrites. For the ODC $CuInSe_2$, the DA pairs were found to exist within the same unit cell [15]. Because the characteristic length R may be on the order of the lattice constants for ODP, an ODC may have absorption or fluorescence that does not obey Eq. (44).

### *5. Transition metal dopant atoms*

When lattices are doped with elements, the absorption from transitions within the dopant atom's electronic levels may be observed. The ruby laser was built on such a system. Ruby consists of $Cr^{3+}$ ion doped into an $Al_2O_3$ crystal lattice. The free Cr atom has an electronic configuration of $[AR]4s^1 3d^5$ [55]. In the first row of transition metal elements only chromium and copper have unfilled 4s electrons. The 4s and 3d orbitals are

very close in energy, with the 4s actually having less energy than the 3d states for these two metals. In $Cr^{3+}$ the electronic configuration is [AR] $3d^3$ [55].

Of course, the state of chromium being described is in a solid and not a free atom. The general approach is to consider how the crystal field, which is the electrostatic field produced by the ions of the lattice that surround the dopant atom, affects the energy levels of the dopant valence orbitals. Because the electrostatic field produced by the ions surrounding the dopant ion will depend on the spatial arrangement of the crystalline ions, symmetry terms will be used to describe the crystalline environment. Figure 21 shows a dopant atom in an octahedral environment. For example, if a free atom is placed in an octahedral field, this atom will have d orbitals split between two energy levels with symmetry $e_g$ and $t_{2g}$. The amount of this splitting is described as 10Dq, which is often called the crystal field splitting. Dq is the field strength parameter [56]. The first half of the first row of transition metal ions, which includes chromium, generally has crystal field splitting on the order of 10,000 to 20,000 $cm^{-1}$ [56]. Ligand field theory is an extension of crystal field theory, which allows for some interaction between the orbitals of the dopant crystalline lattice ions. Although excellent at describing many crystalline situations, ligand field theory is not particularly good with covalent bonding [57]. However, for a weak crystal field such as was found in $CdGa_2S_4$, ligand field theory is generally quite good.

For symmetry environments of crystal ions other than octahedral, the dopant orbitals will be split into energy levels other than those levels expected for octahedral symmetry. For this reason, symmetries other than octahedral can make predicting electronic parameters difficult. $CdGa_2S_4$ has $S_4$ symmetry, which is a subset of the tetrahedral environment. Ligand field theory may be used to approximate the results for

$CdGa_2S_4$ in a tetrahedral symmetry. The value for Dq in a tetrahedral field is equal to – 4/9 the value of Dq in an octahedral complex. The small values of Dq for tetrahedral complexes mean that the first row transition metals generally obey Hund's rule and maximize spin [56].

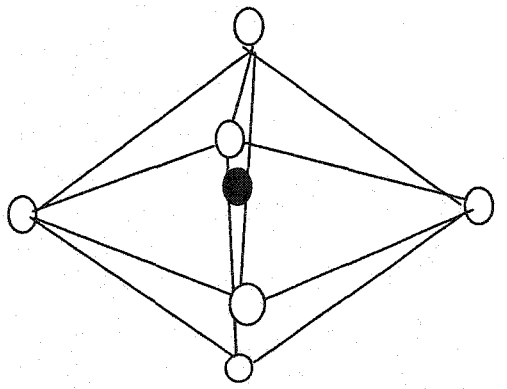

FIG. 21. Octohedral symmetry. Dopant atom is black oval. Host ions are unfilled ovals.

A weak crystal field implies that the electron interaction with other electrons in the atom is much larger than the crystal field. The electron-electron interaction within an atom depends on the Coulombic integral and the exchange integral. The exchange integral was discussed in Chapter 4. However, the exchange dealt with here is of two electrons within the same atom and is not an exchange between electrons on different atoms. The Coulombic operator for two wavefunctions, $\Psi_1$ and $\Psi_2$, is

$$Hc = \tfrac{1}{2} \int \Psi_1^* \Psi_2^* \left( \frac{e^2}{|r_1 - r_2|} \right) \Psi_1 \Psi_2 . \tag{45}$$

It should be mentioned that $\Psi_1$ and $\Psi_2$ in the above equation refer to the wavefunctions for two different orbitals in the same atom [56].

It is difficult to solve Schrodinger's equation for a many electron atom in order to find the wavefunctions, $\Psi_1$ and $\Psi_2$. The radial functions appropriate for the solution to the many electron Schrodinger equation are the Slater integrals, $F_0$, $F_2$, $F_4$, . . . Specific combinations of Slater integrals are defined as the Racah parameters, A, B, and C [52].

$$A=F_0 - 49F_4 \quad (46)$$

$$B=F_2 -5F_4$$

$$C=35\ F_4$$

The exchange and Coulombic integrals may be expressed in terms of Racah parameters A, B, and C. Because the energy of states depends on the Coulombic and exchange integrals, Racah parameters may be used to write the energy of atomic states. For example the energy of the $^2E$ state of $Cr^{3+}$ may be expressed as $-1.8A+7B+4C$ [27].

Tanabe-Sugano diagrams plot the energy of the electronic energy levels that can be associated with octahedral symmetry for a specific number of d electrons, in terms of the dimensionless parameter E/B, against the dimensionless parameter 10Dq/B [56]. In these diagrams B is the Racah B parameter. The Tanabe-Sugano diagrams may be used to predict the energy of electronic transitions of metal ions in an octahedral crystal field [56]. $CdGa_2S_4$ is approximated as a tetrahedral crystal field instead of an $S_4$ crystal field symmetry. Therefore, the use of Tanabe-Sugano diagrams, which are calculated for an octahedral field, needs to be modified. However, a tetrahedral crystal field is very similar to an octahedral field, and there is only one modification. The number of electrons referred to in the diagram must be $d^{10-n}$ rather than $d^n$, where n for $Cr^{2+}$ is 4.

### *6. Polarized absorption*

Often absorption bands depend on the polarization of the incident electromagnetic radiation. For lattice vibrations this dependence is easily understood. From classical mechanics it is known that a three dimensional oscillator will have normal modes of oscillation. Linearly polarized light will have an electric field oscillating in one plane formed by the propagation vectors of the electric and the magnetic fields. As this plane of oscillation coincides with the preferred direction of oscillation for the system, more of the energy will be absorbed. When the linearly polarized light's plane of oscillation is perpendicular to the preferred direction for the system to oscillate, none of the electromagnetic radiation will be absorbed. For electronic transitions the wavefunctions, particularly for the d orbitals, may be orientated in one direction and will absorb electromagnetic radiation most strongly in that direction.

## B. Luminescence of solids

Fluorescence and luminescence are used interchangeably to describe the emission of light by a system. For a solid state system, fluorescence occurs through several processes. Fluorescence studies are sensitive to defect energy levels that are below the energy gap and recombine radiatively. If low energy level defects do not emit, these defects are referred to as nonradiative traps, and will not be seen by fluorescence studies [28]. When excited to a higher state within the band structure, an electron will leave a hole in the lower level of the band structure. As the electron–hole pair is destroyed electromagnetic radiation is emitted in a process called radiative recombination. The band to band transitions may be indirect or direct and will dominate at higher

temperatures. Low temperature luminescence studies may show the energy levels within the band gap of defects [28].

For dopant atoms incorporated into host lattices, fluorescence may be observed from the transitions within the atom's electronic orbitals. The ruby laser is built on such a system. The electronic structure of $Cr^{3+}$ in ruby was discussed above. After excitation is provided to the ruby laser the electrons in chromium's d orbitals are excited from the ground state of $^4A$ to the $^4F$ state. Theelectrons then decay nonradiatively to the $^2E$ level. The crystal fluoresces as the electrons in the $^2E$ level recombine radiatively with the holes left in the ground state.

Several mechanisms exist that will quench fluorescence when more than one defect is present. In the most obvious mechanism, one defect within a crystal may absorb radiation emitted from another defect. It is also possible for phonons to assist in quenching fluorescence from a defect. A defect may fluoresce within a solid and a second defect may then absorb this fluorescence with the creation or annihilation of a phonon. Another mechanism that will quench luminescence of a dopant ion is for the dopant to be involved in an exchange coupled system.

### C. Exchange systems in absorption and luminescence

The effect of the exchange interaction on absorption and luminescence is directly determined by the size of the interaction. The ligand field for a strong exchange coupled system will generally be a weak crystal field. Because the exchange integral will be large, the electron-electron interactions will be greater than the crystal field [27].

When an atom is involved in an exchange system, the absorption bands may be changed from the bands predicted by Tunabe-Sugano diagrams, and the fluorescence may

be quenched. The appropriate Hamiltonian for optical interactions between the electronic states of these two coupled ions will be the Coulombic Hamiltonian. The resulting integral is Eq. (44). For exchange systems the wavefunctions $\Psi_1$ and $\Psi_2$ correspond to the two interacting centers, and not to the electronic wavefunctions of atomic orbitals, as stated before in Eq. 44.

After a Taylor expansion, the Coulombic Hamiltonian will yield a series of terms, including an overlap integral of the following form for the excited state of ion 1, $\varphi_{1e}$; the ground state of ion 1, $\varphi_{1g;}$, the excited state of ion 2, $\varphi_{2e:}$ and the ground state of ion 2, $\varphi_{2g}$ [52].

$$E = \int\left[\phi_{2e}(\vec{r}_1)\phi_{1g}(\vec{r}_2)\right]^* H_c\left[\phi_{2e}(\vec{r}_2)\phi_{1g}(\vec{r}_1)\right]d\vec{r}d\vec{r}_2 \tag{47}$$

Because the two atoms that are interacting may be separated in the crystal by a large distance, at least in crystallographic terms, this overlap integral is generally very small. In the case of superexchange, the overlap integral is between two adjacent atoms and not between the interacting centers. The adjacent atoms are connected to the bridge atoms through molecular bonds, which allow the two defects to exhibit exchange behavior [44].

Exchange interactions can have dramatic consequences on absorption and fluorescence studies of dopant atoms in a crystalline lattice. It has been shown experimentally that a strong interaction may have absorption bands corresponding to the coupled system [48]. One effect of exchange interactions on absorption may be the introduction of new absorption bands that result from the simultaneous excitation of both atoms in the exchange pair. For example, in dimeric $Fe^{3+}$ an exchange interaction has been found to produce an additional absorption band with an energy that is essentially the

sum of the energy of the one center ligand transition [27]. For a weak exchange interaction, the optical spectra are the same as the spectra seen for individual atoms [58].

Exchange interactions influence fluorescence studies mainly by providing a mechanism to quench the fluorescence. If the rate of exchange is faster than the lifetime of the excited state, luminescence may be quenched. If the exchange is between a dopant atom and an atom of the host lattice, the dopant electron may exchange with the host atom in an energy level above the ground state. This exchange would transfer the excited state energy of the dopant atom to an atom in the host lattice, where nonradiative decay may occur. The fluorescence expected from transition within the dopant atom would not be seen.

## D. Experimental results

### *1. Absorption*

The unpolarized absorption of $CdGa_2S_4$, $CdGa_2S_4$:Cr, and annealed $CdGa_2S_4$:Cr showed the presence of many bands. All samples had a large absorption in the visible region. The region of visible absorption in $CdGa_2S_4$ extends to 450 nm. In $CdGa_2S_4$:Cr the region of visible absorption extends to 600 nm. The near IR phonon bands listed in earlier experiments with $CdGa_2S_4$ were seen [49]. However, in the samples the absorption strength of these near IR bands is very weak. Figure 22 illustrates the unpolarized absorption of crystal K3A for the spectral region from 450 nm to 4000 nm. Both $CdGa_2S_4$:Cr and the annealed $CdGa_2S_4$:Cr showed an extension of the visible absorption to approximately 600 nm, as well as absorption bands centered at 1288 nm, 2855 nm, and 3430 nm.

There was no difference in the absorption coefficient of either band between the annealed and unannealed crystals K4 and K4A. There did appear to be a difference between the annealed sample K3A and the unannealed sample K2. However, these crystals did not have light incident on the same face. Because $CdGa_2S_4$ is birefringent, part of the change in absorption peaks for samples K2 and K3A may result in a loss of light that propagates through the sample as the ordinary ray.

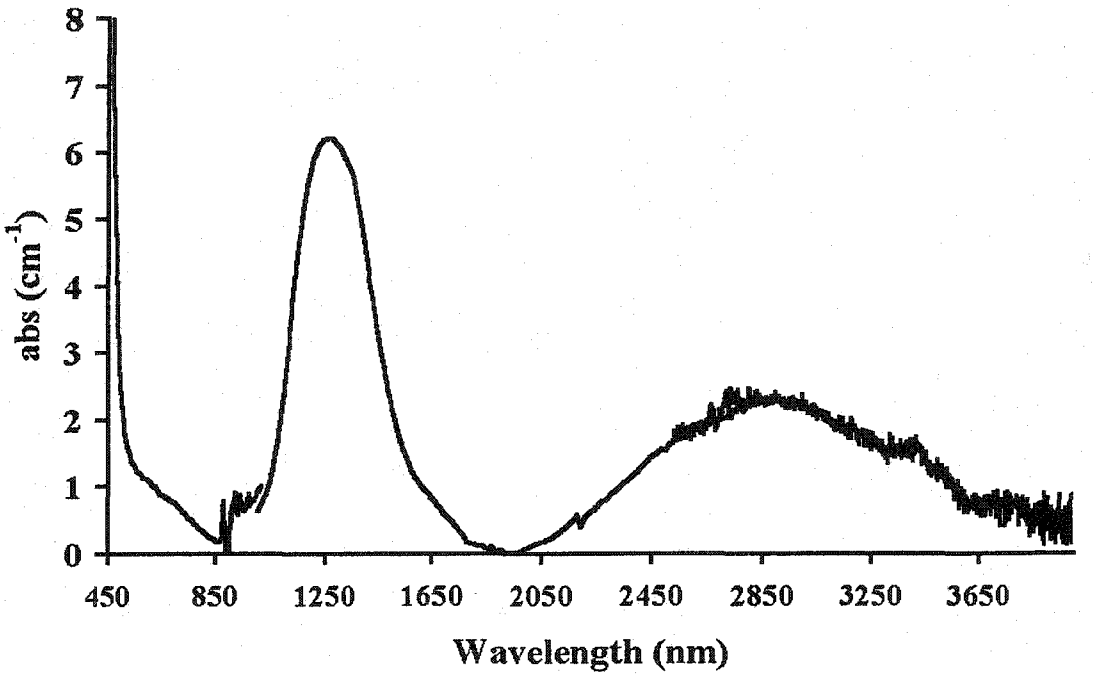


FIG. 22. Absorption of $CdGa_2S_4$:Cr crystal K3A in unpolarized light. The light was incident on an undetermined face.

The compression of the c axis in $CdGa_2S_4$ will reduce the symmetry from tetrahedral to $S_4$. This reduction of symmetry will result in a splitting of states. One result of the splitting of states is a shift that changes the wavelength of absorption slightly from the absorption in a tetrahedral symmetry. The other result of the splitting of states

is that additional bands may occur. However, the additional bands should have energy near the band predicted from the tetrahedral analysis. For $Co^{2+}$ in $CdGa_2S_4$ the splitting energy is approximately 800 $cm^{-1}$ [25]. The energy of the splitting of $Co^{2+}$ in $CdGa_2S_4$ causes a change in the absorption wavelength of 240 nm. Because the energy splitting for chromium in $CdGa_2S_4$ is not known, the values for tetrahedral symmetry are used with the realization that the resulting absorption bands could be shifted slightly by treatment with $S_4$ symmetry.

To understand the possible origins of the absorption bands in $CdGa_2S_4$:Cr, the results were analyzed with ligand field theory by borrowing results from the similar systems of $Co^{2+}$ in $CdGa_2Se_4$ and $Co^{2+}$ in $CdGa_2S_4$. The crystal field splitting, 10Dq, of $Co^{2+}$ in $CdGa_2S_4$ has been determined to equal 3640 $cm^{-1}$ [25]. The crystal field splitting of $CdGa_2S_4$ was determined by using the Racah parameters for $Co^{2+}$ in $CdGa_2Se_4$, $B_{Co2+}$, of 455 $cm^{-1}$ [59]. The energy of the absorption of $Co^{2+}$ in $CdGa_2S_4$ for the transition from $^4A$ to $^4T_1$ is 6200 $cm^{-1}$ [25]. Therefore, the ratio of E/B for $Co^{2+}$ in $CdGa_2S_4$ is

$$\frac{E}{B}=\frac{6200}{455}=13. \tag{48}$$

Using the Tanabe-Sugano diagram for $d^7$, which is appropriate for $Co^{2+}$ in a tetrahedral environment, results in the occurrence of a transition with the ratio of E/B from the ground to the first excited state at a value of Δ/B equal to 8.0. A value of the crystal field splitting, Δ, for $CdGa_2S_4$ can be calculated by multiplying 8.0 times the value of $B_{Co2+}$, 455 $cm^{-1}$.

$$\Delta=(8.0)(455\,cm^{-1})\approx 3640\,cm^{-1}. \tag{49}$$

The crystal field splitting for $CdGa_2S_4$ is in the weak field range, so ligand field theory should be sufficient for describing chromium in $CdGa_2S_4$. Weak field splitting

will favor the high spin complex; and in general, tetrahedral symmetry will be governed by Hund's rule [60]. The ground state electrons will have their maximum multiplicity, which means that $Cr^{2+}$ $CdGa_2S_4$ will have a spin of 2.

There is a difference between the free electron Racah parameters and the Racah parameters of an ion in a solid. There is no value in the scientific literature for the Racah B parameter of $Cr^{2+}$ or $Cr^{3+}$ in $CdGa_2S_4$. The free electron Racah B parameter is used for $Cr^{3+}$, 1030 $cm^{-1}$ [52], as well as the Racah B parameters for free electron $Cr^{2+}$, 830 $cm^{-1}$ [52].

The ratio of the crystal field splitting to the Racah B parameter for $Cr^{2+}$ is about 4. The $d^6$ Tanabe-Sugano diagram used in determining the absorption of $Cr^{2+}$ in $CdGa_2S_4$ is shown in Fig. 23 [61]. A line marked with an asterick has been drawn on the d6 Tanabe-Sugano diagram for this ratio. The value of E/B for the transition from $^5T_2$ to $^5E$ was determined to be 4.5. Multiplying by the B parameter yields a predicted absorption for $Cr^{2+}$ in $CdGa_2S_4$ of 2677 nm, assuming a tetrahedral environment.

Next, the absorption of $Cr^{3+}$ in $CdGa_2S_4$ was analyzed. The $d^7$ Tanabe-Sugano diagram appropriate for $Cr^{3+}$ in a tetrahedral environment is illustrated in Fig. 24 [61]. The ratio of the Racah B parameter for $Cr^{3+}$ to the crystal field splitting for $CdGa_2S_4$ is approximately 3.6. A line marked with an asterick has been drawn on the d7 Tanabe-Sugano diagram at this value. There are two transitions possible within the ground state: $^4T_1$-$^4T_2$, with a wavelength of 3236 nm, and $^4T_1$-$^4A_2$, with a wavelength of 1386 nm. A transition to the first excited state $^4P$ is also possible, and this transition has a wavelength of 485 nm. Because these wavelengths are approximate, it possible that the absorption of $CdGa_2S_4$:Cr at 1288, and 3430 nm is from $Cr^{3+}$. The transition from the ground state,

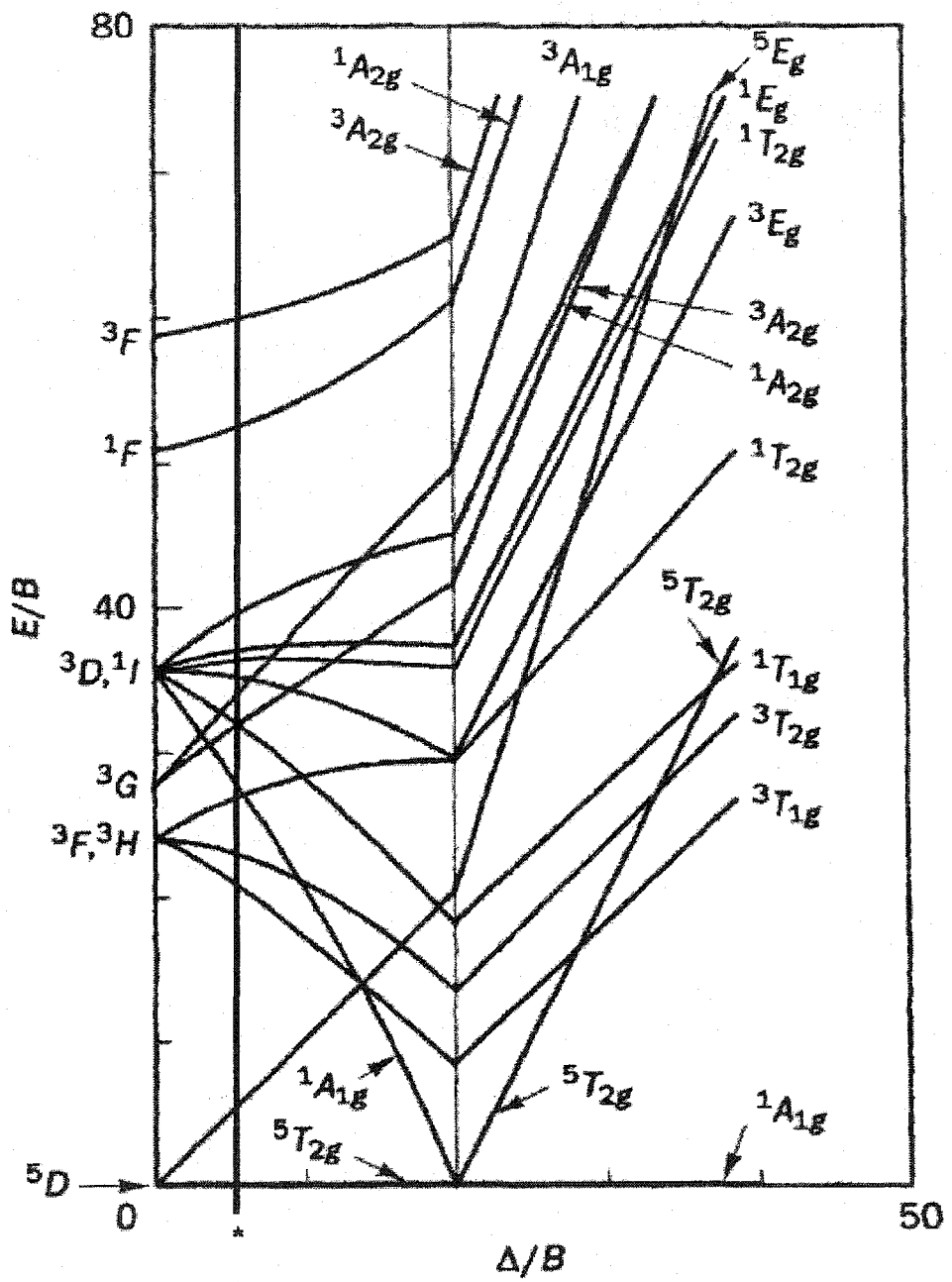


FIG. 23. Tanabe-Sugano diagram for $d^6$ ions in an octahedral environment, or $d^4$ ions in a tetrahedral environment. Line designated by * corresponds to the calculated crystal field splitting of $CdGa_2S_4$.

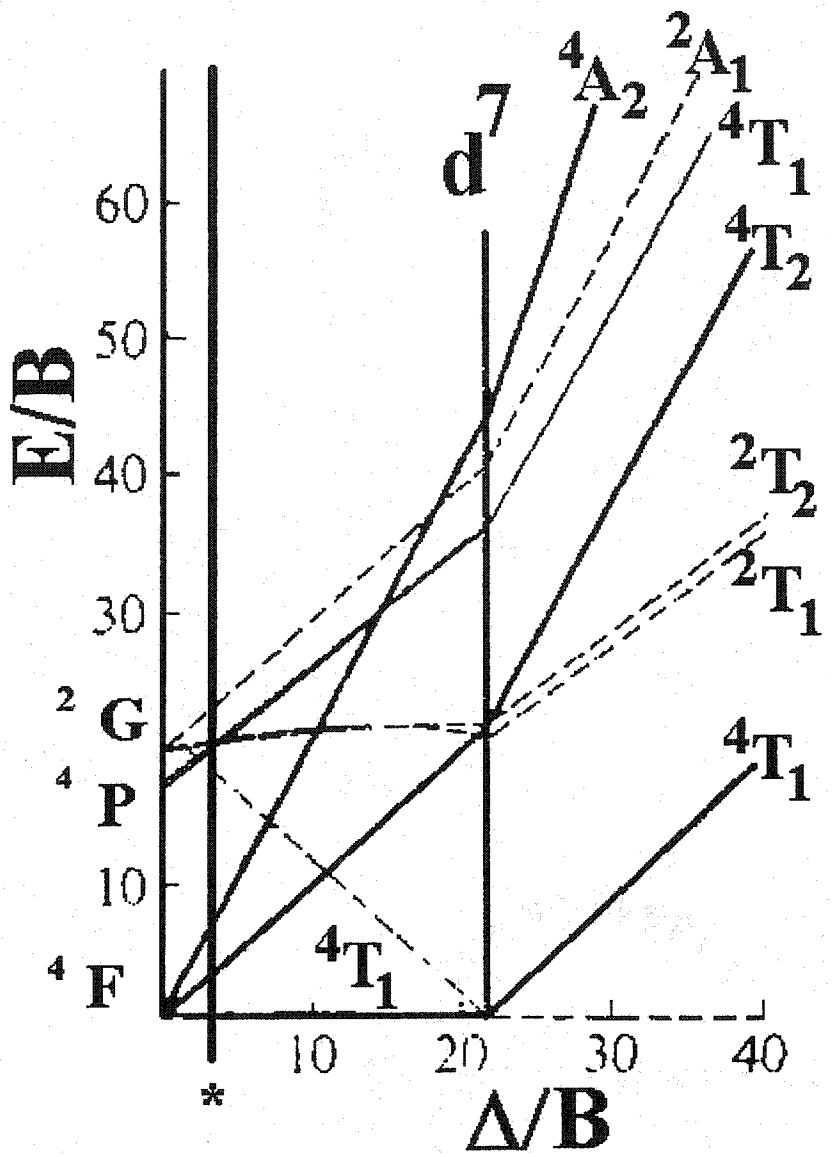


FIG. 24. Tanabe-Sugano diagram for $d^7$ ions in an octahedral environment, or $d^3$ ions in a tetrahedral environment. Line designated by * corresponds to the calculated crystal field splitting of $CdGa_2S_4$.

$^4T_1$, to the first excited state, $^4P$, could also explain the increased region of visible light absorption noted in $CdGa_2S_4$:Cr. The analysis of the absorption bands present in $CdGa_2S_4$:Cr showed that the bands not present in undoped $CdGa_2S_4$ could be assigned to transitions from the chromium ion under the assumption that chromium was incorporated in the lattice as both $Cr^{2+}$ and $Cr^{3+}$. The absorption band centered at 2855nm can be attributed to $Cr^{2+}$ $CdGa_2S_4$. The absorp-tions at 3430 nm, 1288 nm, and the extension of the visible absorption to 600 nm may be attributed to transitions from $Cr^{3+}$ in $CdGa_2S_4$.

Figure 25 illustrates the results for the temperature dependence of unpolarized absorption of $CdGa_2S_4$:Cr. The low temperature spectra of the annealed $CdGa_2S_4$:Cr sample showed a narrowing of the broad line centered at 1288 nm and a disappearance of

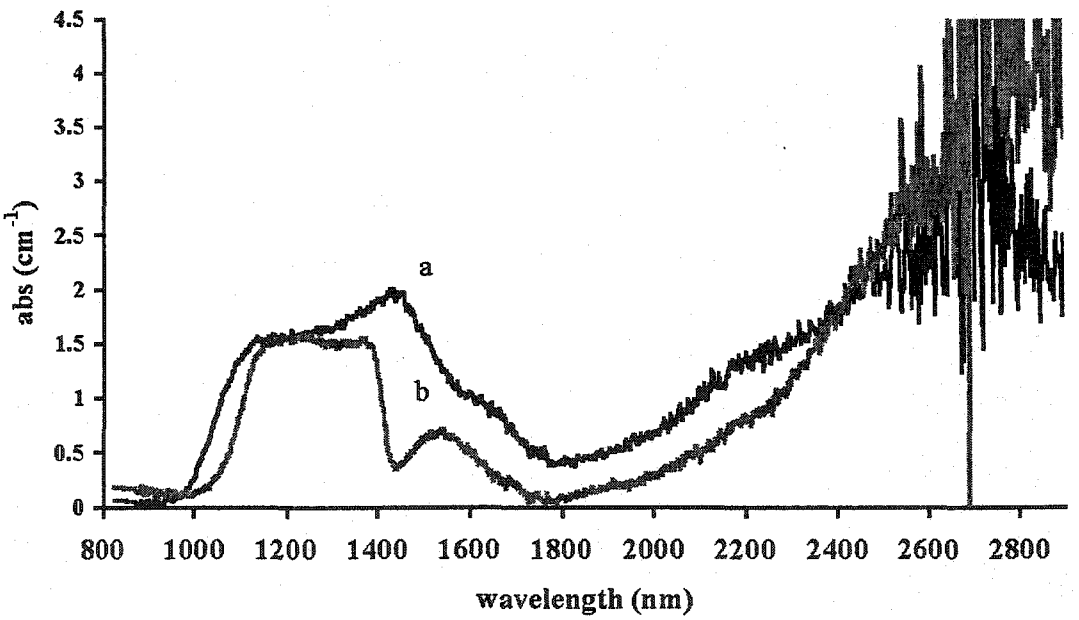


FIG. 25. $CdGa_2S_4$:Cr crystal K3A unpolarized absorption. The spectra were taken at (a) 300 K and at (b) 13 K.

the absorption band at 1420 nm. This type of narrowing is consistent with quenching of phonon states as the temperature of the sample is lowered.

### *2. Polarized absorption*

Figures 26 and 27 show the maximum and minimum absorptions of sample K4A for linearly polarized light. It is known that the strength of absorption bands often depends on the polarization of the incoming radiation. The polarization dependence of the absorption band centered at 1288 nm was studied. There were no polarizers commercially available to study the polarization dependence of the absorption band centered at 2855 nm. The absorption band at 1288 nm in $CdGa_2S_4$:Cr was found to have a maximum intensity when the light was polarized parallel to the (1,-1,0) direction and a minimum intensity when the light was polarized parallel to the (1,1,2) direction.

Figure 28 shows the angular variation of the polarization from the (1,-1,0) direction for the band centered at 1288 nm in the annealed sample, K4A; the unannealed sample, K4; and the undoped sample, Kun. The absorption data are reported for 180° in 15° increments. The absorption coefficient measured at each polarization angle is the same for the annealed and unannealed $CdGa_2S_4$:Cr crystals. The experimental error bars are determined by the uncertainty in the angle of polarization.

### *3. PL*

PL measurements in the IR were made at low temperature, 12 K, and room temperature, 300 K, on $CdGa_2S_4$:Cr. Because $CdGa_2S_4$:Cr is being evaluated for possible use as a laser gain medium, measurements were made with an excitation of 1.56 from an Erbium diode laser and 2.5 μ light from a ZnS:Cr laser at both room temperature and

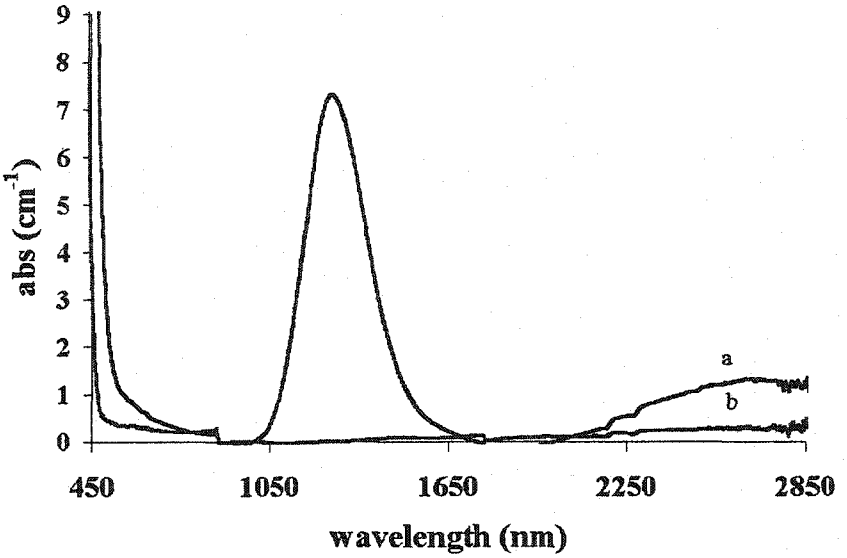


FIG. 26. Absorption of (a) $CdGa_2S_4$:Cr and (b) $CdGa_2S_4$ in light linearly polarized in the (1,-1,0) direction.

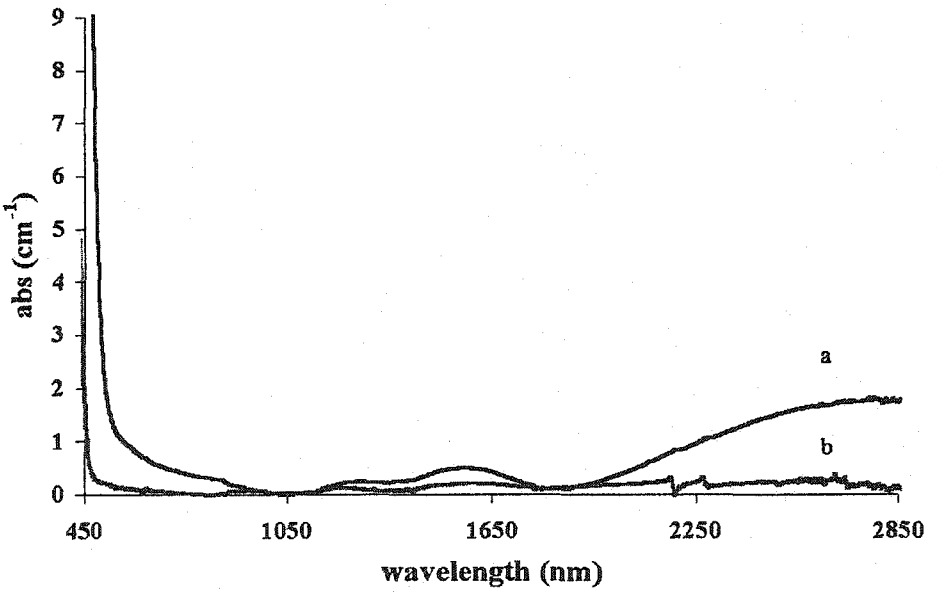


FIG. 27. Absorption of (a) CdGa2S4:Cr and (b) CdGa2S4 in light linearly polarized in the (1,1,2) direction.

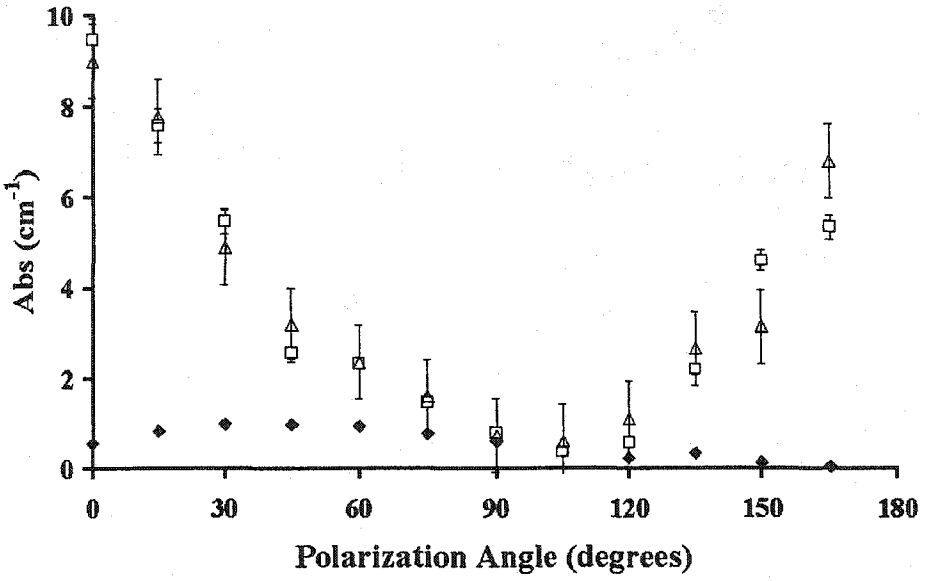


FIG. 28. Polarized absorption of band centered at 1288 nm in $CdGa_2S_4$:Cr and $CdGa_2S_4$. Filled symbols (♦) correspond to undoped $CdGa_2S_4$. Unfilled symbols are absorption for K4A, annealed $CdGa_2S_4$:Cr (Δ) and K4, unannealed $CdGa_2S_4$:Cr (□).

77 K with detectors sensitive to light in the IR region from 1000 to 5000 nm. The measurements at 77 K directed the excitation radiation through a quartz rod. Quartz does not transmit radiation from 2.5 to 2.7 μ and from 3.3 to 4.0 μ. If the sample fluoresces in these wavelength regions the quartz will absorb the emitted radiation. The spectra for excitation at 2.5 μ light at room temperature and low temperature are shown in Fig. 29. At room temperature a diffraction grating of 300 grooves /mm was used. To reduce the signal from the excitation light the low temperature PL illustrated in Fig. 30 used a diffraction grating of 150 grooves/mm.

Essentially the measurements of PL with excitation of 2.5 μ yielded no fluorescence. The PL measurements were also conducted with excitation of 1.5 μ with the same results as excitation at 2.5 μ. Assuming the difference in the region of visible absorption was caused by the transition in a $Cr^{3+}$ ion from the ground to first excited

state, as outlined in the discussion of the absorption data, a PL experiment with excitation of 450 nm was also performed. No fluorescence was observed at room temperature in the

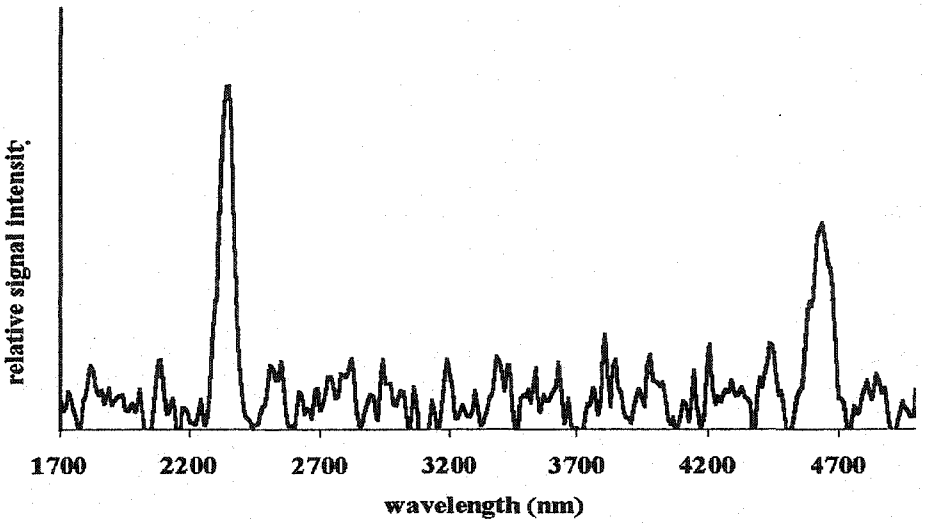


FIG. 29. PL of $CdGa_2S_4$:Cr with excitation of 2500 nm and with a diffraction grating of 300 grooves/mm at 300 K. The peak at 2500 μ corresponds to the excitation wavelength. The peak at 4700 nm corresponds to the second harmonic of the excitation wavelength.

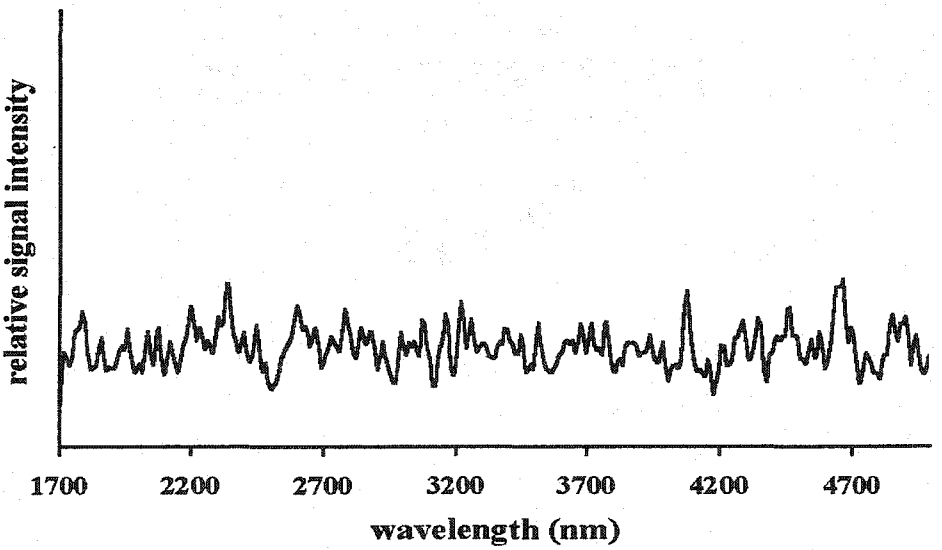


FIG. 30. PL of $CdGa_2S_4$:Cr with excitation of 2500 nm and with a diffraction grating of 150 grooves /mm at 77 K.

region from 500 to 1200 nm. A cryostat was used to lower the temperature to 13 K. The cryostat unit has optical windows of MgF, which will not absorb radiation in the spectral region being used for excitation or detection. No fluorescence was observed from this PL experiment.

Because it is known that $CdGa_2S_4$ has a high concentration of native defects, it is believed that the chromium interacts and transfers energy to these defects in a manner similar to what was seen in $CdGa_2S_4$:In and $CdGa_2S_4$:Ag [22]. To test this theory PL with band to band excitation was performed at room temperature and 77 K. Excitation light energy corresponding to the energy band gap of 3.4 eV, or 354 nm, was used to induce band to band excitation. At room temperature no fluorescence was seen. As shown in Fig. 31, in liquid nitrogen, 77K, fluorescence was found throughout the visible

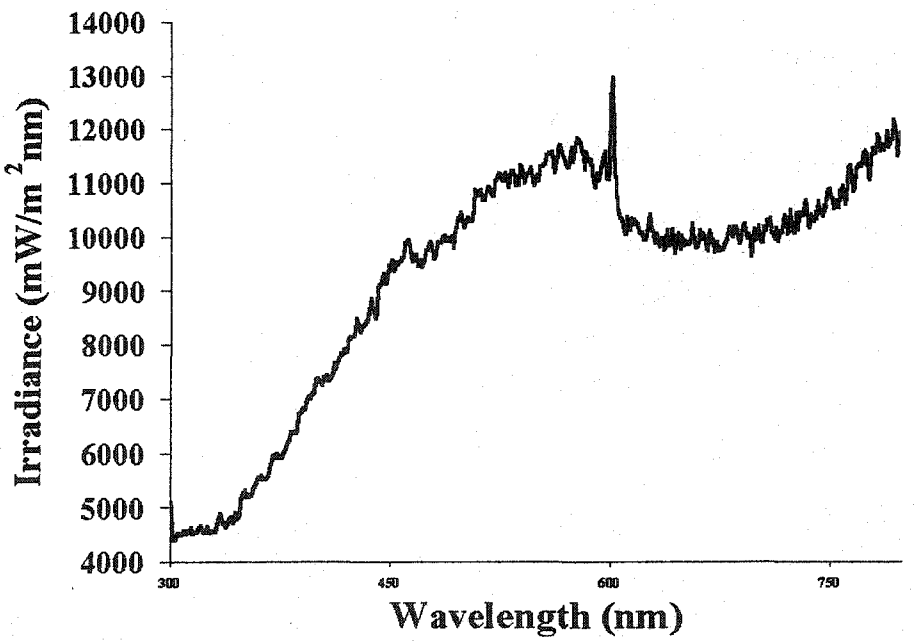


FIG. 31. Fluorescence at 605nmof $CdGa_2S_4$:Cr at 77K.

region of 360 to 700 nm, with a peak at 605 nm. The PL of $CdGa_2S_4$:Cr is virtually identical to the PL of undoped $CdGa_2S_4$, $CdGa_2S_4$:Ag, and $CdGa_2S_4$:In

Because there are many different mechanisms of fluorescence within a compound, the type of fluorescence observed is governed by competition among the mechanisms. Ternary chalcopyrites have been shown to be particularly tolerant of DA pairs [14]. Previous work has shown the dominance of DA recombination mechanisms in fluorescence of $CdGa_2S_4$, $CdGa_2S_4$:In, and $CdGa_2S_4$:Ag. The fluorescence in PL studies of $CdGa_2S_4$:Ag occurred near 600 nm, and was a result of DA pair recombination [22]. The PL studies did not find fluorescence from any absorption band that could be linked to chromium, either as $Cr^{2+}$ or $Cr^{3+}$, in $CdGa_2S_4$ despite the observance of absorption bands that could be attributed to the chromium atom existing in $CdGa_2S_4$ in both charge states. The PL studies did find fluorescence of $CdGa_2S_4$:Cr from band to band excitation near 600 nm. Based on previous work, the fluorescence from band to band excitation is attributed to donor acceptor pair recombination [22].

## E. Discussion

The initial goal of the current study was to determine the suitability of $CdGa_2S_4$:Cr for creating a solid state laser based on transitions within the $Cr^{2+}$ ion. Absorption studies of $CdGa_2S_4$:Cr are consistent with chromium's being incorporated into the lattice as both $Cr^{2+}$ and $Cr^{3+}$. PL studies with $CdGa_2S_4$:Cr did not indicate any fluorescence from within the excited Cr ion. PL studies with band to band excitation did show fluorescence consistent with earlier studies on $CdGa_2S_4$:Ag. Incorporation of chromium into a DA pair system and an exchange interaction may cause the lack of

fluorescence from the Cr ion. Based on the optical studies, $CdGa_2S_4$:Cr does not show promise as a laser active material.

# CHAPTER 6

## SUMMARY

Because no previous work has been done on $CdGa_2S_4$:Cr, several methods were used to investigate the properties of this material. Absorption, PL, TSL, TSC, and Hall mobility studies done on $CdGa_2S_4$, $CdGa_2S_4$:In, $CdGa_2S_4$:Ag, and $CdGa_2S_4$:Co were referenced. Three sets of $CdGa_2S_4$:Cr and $CdGa_2S_4$ crystals were analyzed by using EDXS, XRD, EPR, absorption, and fluorescence measurements. The findings obtained from these measurements represent the first published results of studies done on $CdGa_2S_4$:Cr.

After analyzing the data from the various experiments I reached several conclusions. The defect chalcopyrite $CdGa_2S_4$ grown by different groups exhibits similar spectroscopic properties. Only crystal K1, when analyzed with XRD, did not yield diffraction peaks associated with the known peaks of $CdGa_2S_4$. Several other samples of $CdGa_2S_4$:Cr grown by the same group produced XRD peaks consistent with the defect chalcopyrite structure. It is thought that crystal K1 may have come from a different part of the boule, which did not grow into a defect chalcopyrite structure. The FWHM of diffraction peaks from omega rocking scans varied from 0.06° to 0.1°. Analysis of two theta scans from the defect chalcopyrite crystal $CdAl_2S_4$ showed FWHM similar to those FWHM seen on two theta scans of $CdGa_2S_4$ [62]. EDXS analysis showed stoichiometric variations, particularly in gallium, between the annealed and unannealed crystals. All of

the crystals were varying shades of yellow to topaz. The topaz-colored crystals had a higher content of gallium and chromium than the yellow crystals. An abundance of gallium in $CdGa_2S_4$ causes the crystal to be a pale yellow color [16]. Because topaz is a yellow-brown color, it is thought the topaz color results from the higher chromium content.

Undoped, unexcited $CdGa_2S_4$ did not produce any EPR signal, even with a high concentration of native defects. When receiving band to band excitation, undoped $CdGa_2S_4$ produced an EPR signal. Therefore, the defects in $CdGa_2S_4$ normally exist in a nonparamagnetic state.

Our EPR investigations of $CdGa_2S_4$:Cr focused on the two resonance lines that were present in all EPR spectra. These signals have g values related by a factor of 2. The reason for the factor of 2 relationship between the resonance signals is unclear. The signals have several aspects that do not fit with EPR spectra expected for dilute systems. The angular variation about a single axis and the temperature dependence fit EPR spectra expected for shallow-mass-like acceptors or exchange systems. The resonances analyzed had angular variation about several axes, line width variation, line shape variation, and temperature variations consistent with EPR spectra expected for a strong exchange system with exchange narrowed resonances. There is no particular angular variation for rotation about different axes for exchange coupled systems, so the angular variation of $CdGa_2S_4$:Cr about different axes may be consistent with an exchange coupled system. However, the lack of angular variation in the spectra about different rotation axes is a bit surprising. Comparison with a known standard of phosphorus doped silicon and the assumption of a uniform distribution of centers determined the density of centers for the combined resonances to be on the order of $10^{17}$ to $10^{18}$ defects per $cm^3$.

The chromium incorporated into the crystal lattice did not show a characteristic EPR signal. The EPR signals for $Cr^{3+}$ are well studied, and they should be seen without optical excitation. The EPR signals for $Cr^{2+}$ are less well studied, and it is not surprising for these signals to be absent from the EPR spectra of the crystal.

$CdGa_2S_4$ was found to have a very weak crystal field [25]. The optical absorption showed the presence of one line at 2855 nm that could be caused by $Cr^{2+}$ in a tetrahedral symmetry. Additional lines at 3430 nm, at 1288nm, and near 450 nm could be explained by the absorption of $Cr^{3+}$ in $CdGa_2S_4$. The PL studies with excitation at the absorption bands of chromium did not find any fluorescence. The PL studies with band to band excitation of $CdGa_2S_4$:Cr found fluorescence at 605 nm. Previous PL studies on $CdGa_2S_4$:Ag found fluorescence from DA recombination at 620 nm [22]. The PL studies are consistent with the model proposed earlier for PL of $CdGa_2S_4$, $CdGa_2S_4$:Ag, and $CdGa_2S_4$:In [22]. Fluorescence is produced by DA pair recombination in this model.

Table 5 shows a comparison of EPR signal strength with optical absorption coefficients and chromium doping levels. No correlation was found between the EPR signal and the absorption coefficient for the bands at 1288 nm and 2855 nm. The optical absorption coefficient for the band centered at 2855 nm is based on data taken at 2700 nm.

Because no PL was observed for excitation of $CdGa_2S_4$:Cr by any wavelength that could be associated with the chromium dopant, $CdGa_2S_4$:Cr is not a promising laser gain medium for solid state paramagnetic ion lasers. The EPR spectra can best be explained through exchange theory. However, two aspects of the results remain to be fully reconciled: the factor of 2 relationship between the *g* values of each resonance and the fact that the angular dependence of *g* is the same in all rotation planes. Although these

two observations are not contradictory with exchange theory, it is not yet clear how the observations are incorporated into the exchange theory interpretation. Thus, modifycations or even an alternate theory may be necessary to interpret the data properly.

TABLE 5. Relative number of centers in EPR resonance and absorption coefficient.

| Crystal | Signal Intensity referenced to K2 ($10^{17}$ centers/$cm^{-3}$) | | Optical absorption coefficient, ($cm^{-1}$) | | Doping Level (Cr atoms/$cm^3$) |
|---|---|---|---|---|---|
| | g=6 | g=3 | 1288 nm | 2855 nm | |
| K2 | 1.0±0.50 | 1.0±0.50 | 13.37±1.33 | 4.6± 0.46 | 6.E+19 |
| K3A | 1.35±0.67 | 1.95±0.98 | 27.62±2.76 | 5.0±0.50 | 6.E+19 |
| K4 | 0.87± 0.44 | 1.22 ± 0.61 | 9.47±0.95 | 2.56±0.25 | <6.E+19 |
| K4A | 5.75±2.88 | 3.75±1.88 | 9.00±0.90 | 2.41±0.24 | <6.E+19 |

# CHAPTER 7

# FUTURE WORK

There are many different avenues toward which future work could be directed, some of which depend on the area of interest.

Annealing studies of $CdGa_2S_4$:Cr would provide useful information about the nature of the defects studied which were responsible for the EPR signals studied. Often different defects will not anneal equally. With annealing studies, it may be possible to determine whether the two resonances being studied result from two separate exchange systems or one. Crystal K4A had a complete reduction in one center at 3400 G from annealing. A detailed study of annealing conditions, such as temperature, time, and environment could improve the overall quality of doped $CdGa_2S_4$.

From the standpoint of material science, much work should be done to verify the conclusions. The most obvious need is to perform EPR at several different microwave frequencies. These frequencies should include Q-band (34 Ghz or 1.17 $cm^{-1}$) and, if possible, W-band (94 Ghz or 3.23$cm^{-1}$) EPR [63], because the frequencies may be great enough to bring the EPR spectra of $CdGa_2S_4$:Cr out of the strong exchange regime. Even if the experiment stays in the strong exchange regime, these bands may prove useful to confirm the exchange coupled nature of this defect. The line width of an exchange coupled system has a known functional dependence on the EPR microwave frequency [44]. Additionally, EPR work should also include an analysis of the signal induced from band to band excitation.

Because the exchange coupling constant was derived based on five data points, it would be useful to determine the EPR spectra intensity for more temperatures and lower temperatures. At 4 K the EPR spectra appeared to have a different type of temperature dependence than at higher temperatures.

Magnetic susceptibility measurements should be done to determine the total spin state of $CdGa_2S_4$:Cr. The exchange coupling constant, $J$, may be determined more accurately from temperature variations of the bulk magnetic susceptibility measurements than from the ratio of the total signal intensity of the EPR spectra.

It was noted that $CdGa_2S_4$ has shown traits consistent with ODC. Studies that focus on this aspect of the material should be done, including absolute stoichiometric analysis of crystals grown under different conditions and possibly by different groups and studies of changes in electrical and optical properties that occur after self doping.

Our research has provided much basic information on the structure, defects, and optical aspects of $CdGa_2S_4$:Cr. However, none of the research suggests that $CdGa_2S_4$:Cr is a promising gain medium for lasers. The main work for the future, from an optical standpoint, is in finding a more suitable host for $Cr^{2+}$ to make a solid state laser in the IR regions. The current research of $Cr^{2+}$ in the zinc chalcogenides, ZnS and ZnSe, is proving to be fruitful.

## LIST OF REFERENCES


[1] J.W. Orton, *Electron Paramagnetic Resonance* (London Iliffe Books LTD, London England, 1967).

[2] J. McKay, K. Schepler, and G. Catella, Opt. Let. **24**, 1575 (1999).

[3] G. Wagner, T. Carrig, R. Page, K. Schaffers, J. Ndap, X. Ma, and A. Burger, Opt. Let. **24**, 19 (1999).

[4] L. Deloach, R. Page, G. Wilke, S. Payne, and W. Krupke, IEEE J. Quant. Electron. **32**, 885 (1996).

[5] R. Page, K. Schaffers, L. DeLoach, G. Wilke, F. Patel, J. Tassano, S. Paune, W. Krupke, K. Chen, and A. Burger, IEEE J. Quant. Electron. **33**, 609 (1996).

[6] *Concise Science Dictionary* (Oxford University Press, New York 1987).

[7] C. Davies, *Lasers and Electro-Optics Fundamentals and Engineering* (Cambridge University Press, New York, 1996).

[8] J. I. Pankove, *Optical Processes in Semiconductors* (Dover Publications, New York, 1971).

[9] J. Dziesiaty, M. U. Lehr, P. Peka, A. Klimakow, S. Muller, and H.J. Schulz, Eur. Phys. J. B **4**, 269 (1998).

[10] U. Kaufman, Phys. Rev. B **11**, 2478 (1975).

[11] L. E. Halliburton, and N. C. Giles, J. Appl. Phys. **79**, 556, (1996).

[12] T. Teranishi, K. Sato, and K. Kondo, J. Phys. Soc. Jpn. **36**, 1618 (1974).

[13] H. J. von Bardeleben, A. Goltzine, C. Schwab, and R. S. Feigelson, A. Phys. Lett. **32**, 741 (1978).

[14] S. B. Zhang, S. H. Wei, and A. Zunger, Phys. Rev. Lett. **78**, 4059 (1997).

[15] S. B. Zhang, S.-H. Wei, A. Zunger, and H. Katayama-Yoshida, Phys. Rev. B **57**, 9642 (1998).

[16] R. S. Fiegelson, and R. K. Route, in *Proceedings of the Sixth annual Conference on Ternary and Multinary Compounds*, edited by B.R. Pamplin, N.V. Joshi, and C. Schwab, (Pergamon Press, Oxford England 1984).

[17] L. M. Suslikov, Opt. Spect. **53**, 285 (1982).

[18] A. A. Lavrentyev, B. V. Gabrelian, V. A. Dubeiko, I. Y.. Nikiforov, and J. J. Rehr, J. Phys. Chem. Sol. **63**, 227 (2002).

[19] D. A. Guseinova, T. G. Kerimova, and R. K. Nani, Sov. Phys. Semi. **11**, 670 (1977).

[20] P. Kivits, J. Phys. C: Sol. Sta. Phys. **9**, 605 (1976).

[21] P. Kivits, M. Wijnakler, J. Claassen, and J. Geerts, J. Phys. C **11**, 2361 (1978).

[22] P. Kivits *Thermoluminescence and Thermally Stimulated Conductivity in $CdGa_2S_4$ Including Evaluation and Some Extensions of the Conventional Two Level Model* University of Eindhoven, Eindhoven (1976).

[23] B. F. Levine, C. G. Bethea, and H. M. Kasper, IEEE J. Quant. Elect. 904 (1974).

[24] K. R. Allakhaverdiev, Z. Y. Salaeva,and A. B. Orun, Opt. Comm **167**, 95 (1999).

[25] Y. Kim, C. Kim, and W. Kim, J. Kor. Phys. Soc. **40**, 952 (2002).

[26] A. N. Georgobiani, V. S. Donu, Z. P. Ilyukhina, V. I. Pavlenko, and I. M. Tiginyanu, Sov. Phys. Semi. **17**, 970 (1983).

[27] P. Day, and N. Sanders, in *Physical Methods in Advanced Inorganic Chemistry,edited by* H. A. O. Hill, P. Day , (Interscience Publishers, New York, 1968).

[28] P. Yu, and M. Cardona, *Fundamentals of Semiconductors Physics and Material Properties* (Springer-Verlag, New York 1996).

[29] B. D. Cullity, *Elements of X-ray Diffraction* (Addison-Wesley, Reading Mass, 1978).

[30] P. Villar, and L. D. Calvert, *Pearson's Handbook of Crystallographic Data for Intermetallic Phases*, (American Society for Metals, Metals Park, Oh, 1985).

[31] H. Hahn, G. Franck, W. Klinger, A. Storger, and G. Storger, Z. Anorg. Allg. Chem. **279**, 16 (1956).

[32] F. O. Advodija, S. K. Kim, S. D. Kim, J. S. Song, K. H. Yoon, and B. T. Aho, Sol. En. Mat. Sol. Cell **55**, 225 (1998).

[33] http://plato.stanford.edu/entries/physics-experiment/app5.html.

[34] R. Algers, *Electron Paramagnetic Resonance: Techniques and Applications* (Interscience Publishers, New York, 1968).

[35] J. Weil, J. Wertz, and J. Bolton, *Electron Paramagnetic Resonance Elementary Theory and Practical Application* (Wiley-Interscience New York, 1994).

[36] E.O. Schulz-DuBois, J.E. Geusic, and M. Peter, Bell Sys. Tech. J. **38**, 271 (1959).

[37] R. Title, Phys. Rev. **133**, A1613 (1964).

[38] A.V. Malyshev, Fiz. Tver. Tele. **42**, 29 (2000).

[39] L.S Dang, K.M. Lee, G.D. Watkins, and W.J. Choyke, Phys. Rev. Lett. **43**, 390 (1980).

[40] N. Ashcroft, and N. D. Mermin, *Solid State Physics* (Holt, Rinehart, Winston, New York, 1976).

[41] E. Merzbacher, *Quantum Mechanics 3rd Ed* (John Wiley and Sons, New York, 1998).

[42] O. Madelung, *Introduction to Solid-StateTheory* (Springer-Verlag, New York, 1981).

[43] http://www.tcm.phy.cam.ac.uk/`ajw29/thesis/nodes8.html.

[44] A. Bencini, and D. Gatteschi, *EPR of Exchange Coupled of Systems* (Springer-Verlag, New York, 1990).

[45] F.E. Mabbs, D. Collsion, *Electron Paramagnetic Resonance of d Transition Metal Compounds* (Elsevier, New York, 1992).

[46] K. Morgaki, J. Phys. Soc. Jpn. **19**, 187 (1964).

[47] H. Statz, L. Rimm, M.J. Wever, G.A. Domers, and G.F. Koster, J. Appl. Phys. **32**, (Suppl.) 218 (1961).

[48] P. McCarthy, and H.U. Gudel, Inorg. Chem. **25**, 838 (1985).

[49] S.I. Radautsan, N.N. Syrbu, I. I. Nebola, V.G. Tyrziu, and D.M. Bercha, Sov. Phys. Semi. **11**, 38 (1977).

[50] D.A. Guseinova, T.G. Kerimova,a nd R.K Nani, Sov. Phys. Semi. **11**, 670 (1977).

[51] F.W. Ohrendorf, and H. Haeuseler, Cryst. Res Tech. **34**, 339 (1999)

[52] B. Di Bartolo, *Optical Interactions in Solids* (John Wiley and Sons, New York, 1968).

[53] L.M Suslikov, Z.P. Gadmashi, I.F. Kopinets, Y. Peresh, and V.Y. Slivka, Opt Spectr. **49**, 51 (1980).

[54] J. Reitz, F. Milford, R. Christy, *Foundations of Electromagnetic Theory* (Addison-Wesley, Reading Mass., 1980).

[55] T. Brown, and H. Lemay, *Chemistry: The Central Science* (Prentice-Hall, Englewood Cliffs N.J. 1981).

[56] H. Schlafer, and G. Gilemann, *Basic Principles of Ligand Field Theory* (Wiley-Interscience, New York 1969).

[57] S. Sugano, Y. Tanabe, and H. Kamimura, *Multiplets of Transition Metal ions in Crystals* (Academic Press, New York, 1970).

[58] S. Kremer, Inorg. Chem. **24**, 887 (1985).

[59] C. Kim, T. Cho, J. Kim, W. Kim, and H. Park, Phys. Rev. B. **36**, 9283 (1987).

[60] http://wwwchem.uwimona.edu.jm:1104/courses/C21Jout.html.

[61] http://wwwchem.uwimona.edu.jm:1104/courses/Tanabe-Sugano/ts0.html.

[62] M. Jin, and W. Kim, Appl. Phys. Lett. **70**, 484 (1997).

[63] http://www.bruker-biospin.de/EPR/elexsys/options/options.html.

# NOTE TO USERS

Duplicate page number(s); text follows.

The manuscript was scanned as received.

101-102

This reproduction is the best copy available.

UMI®

Changes:

Changes to value of J reported: need to multiply by k=0.696
changes to max and min spin states.

Outtakes

The ordered defect pair system in $CuInSe_2$ explains three traits which had been noted in $CuInSe_2$ : (1) the tolerance of stoichiometric deviations, (2) the changes in crystal properties through self-doping, (3) the existence of a large number of neutral defects. It was noted during the investigations that $CdGa_2S_4$ exhibits the same three physical properties that were explained in $CuInSe_2$ by ordered defect pairs. $CdGa_2S_4$ is tolerant of stoichiometric deviations. It is known that $CdGa_2S_4$ should be colorless, but few reports of a colorless material appear. Most reported crystals are shades of yellow, which is attributed to excess gallium. The EDXS study also showed variations in composition across the surface for the $CdGa_2S_4$:Cr crystals. Optical studies have shown the properties of $CdGa_2S_4$ may be changed through self doping. Previous fluorescence studies have shown that annealing with sulfur changes the nature of fluorescence [19]. Lastly, it has been shown that these crystals have large numbers of neutral defects [21].

Based on the physical properties of $CdGa_2S_4$ listed above, $CdGa_2S_4$ may be an ordered defect compound.

The TSL and TSC studies by others of $CdGa_2S_4$:Ag showed the presence of a short range interaction between the Ag and one of the traps. The PL of $CdGa_2S_4$:Cr exhibit the same behavior as the PL studies of $CdGa_2S_4$, $CdGa_2S_4$:Ag, and $CdGa_2S_4$:In. The exchange interactions suggested by EPR may provide a mechanism for dopants in $CdGa_2S_4$ to interact with the ordered defect pair system in the crystal.

Notes:

Using Coulombs energy to account for 600nm absorption with effective *charge of* electron=0.2e we find the distance is 0.1 angstrom
using the full charge of the electron we find the distance would be 2.716 Angstoms – half of the a axis

# APPENDIX A

# ANALYSIS OF EPR RESONANCE LINE SHAPE

The EPR resonance lines show great angular variation not only in zero crossings but also in the line width and apparent line shape. We analyzed the EPR line shapes to determine whether the line shapes are Lorentzian or Gaussian. We chose the variable x to represent the distance between the measured magnetic field, B, and the absorption, $B_0$.

$$x=(B-B_0) \tag{A1}$$

An absorption curve defined by a Lorentzian function $Y_L(x)$ will have an amplitude that varies with the magnetic field, B. The functional form of $Y_L(x)$ is defined in Eq. (A2), where c is a constant [1].

$$Y_L(x)=\frac{Y_L(0)}{\left[1+(cx)^2\right]}. \tag{A2}$$

A Gaussian function, $Y_G(x)$, of x is defined as [1]

$$Y_G(x)=Y_G(0)\exp\left(-(cx)^2\right). \tag{A3}$$

Of course, our EPR spectra are first derivative spectra; therefore, so we must look at the derivatives of Lorentzian and Gaussian functions. The first derivative with respect to x of a Lorentzian function is

$$\frac{d}{dx}(Y_L(x))=\left(-\frac{2Y_L(0)cx}{\left[1+(cx)^2\right]^2}\right). \tag{A4}$$

The square root the ratio of x to the absolute value of the derivative of $Y_L(x)$ is

$$\sqrt{\left(\frac{x}{\left|\frac{d}{dx}Y_L(x)\right|}\right)}=\sqrt{\left(\frac{\left[1+(cx)^2\right]^2}{2Y_L(0)c}\right)}=\left(\frac{1}{\sqrt{2Y_L(0)c}}\right)+\frac{(cx)^2}{\sqrt{2Y_L(0)c}}. \tag{A5}$$

If we now redefine a variable y equal to $x^2$, Eq. (A5) is linear in y. Therefore, a plot of with Eq. (A5) verses $x^2$ will be linear.

The first derivative of $Y_G(x)$ is

$$\frac{d}{dx}\left(Y_G(x)\right) = -2cxY_G(0)\exp\left(-(cx)^2\right). \tag{A6}$$

The square root the ratio of x to the absolute value of the derivative of $Y_G(x)$ is

$$\sqrt{\left(\frac{x}{\left|\frac{d}{dx}Y_G(x)\right|}\right)} = \sqrt{\left(\frac{1}{2cY_G(0)\exp(-(cx)^2)}\right)} = \left(\frac{1}{\sqrt{2Y_L(0)c}}\right)\exp((cx)^2). \tag{A7}$$

If we now redefine a variable y equal to $x^2$, Eq. (A7) is exponential in y. Therefore, a plot of with Eq. (A7) versus $x^2$ will be exponential.

Figure A1 shows the shape of a Lorentzian and Gaussian absorption curve. The line shape of our EPR resonances was analyzed by plotting the following function of the applied magnetic field, (B); the zero crossing of the resonance, ($B_0$); and the amplitude of the first derivative line at the applied magnetic field [Y(B)],

$$\left[\left(B-B_0\right)\Big/Y(B)\right]^{1/2} \tag{A8}$$

versus $(B-B_0)^2$ [44]. From our derivation above, we know this plot yields a straight line for a first derivative Lorentzian absorption and an exponential for a first derivative Gaussian absorption.

Figure A2 shows the line shape analysis of the EPR data at the minimum line width. Figure A2 clearly shows a Lorentzian nature of the line shape. Figure A3 shows a line shape analysis of the EPR spectra at the maximum line width. Figure A3 is Lorentzian shaped near the origin and has Gaussian nature away from the origin. This type of line shape is expected for an exchange coupled system's EPR resonance lines at the widest line width. After review of the line shape analysis plots for data taken every $15^{\circ}$ over $180^{\circ}$ range, we feel the line shape is Lorentzian near the origin. The line shapes became increasingly more Gaussian in nature as the line widths became wider. This change in line shape is consistent with the line shape expected from exchange coupled systems.

## LIST OF REFERENCES

[1] J. Weil, J. Wertz, and J. Bolton, *Electron Paramagnetic Resonance Elementary Theory and Practical Application* (Wiley-Interscience New York, 1994).

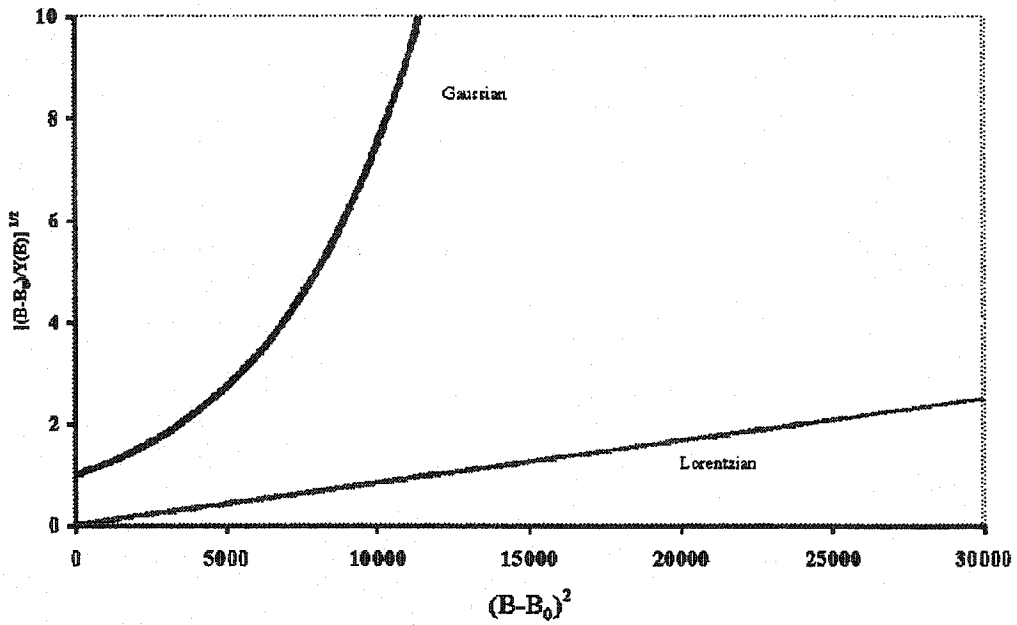


FIG. A1. Line shape analysis of Gaussian and Lorentzian functions. The Gaussian function is 25exp(-(0.02(B-1118))2). The Lorentzian function is 25,000/(1+ (0.07(B-1118))2).

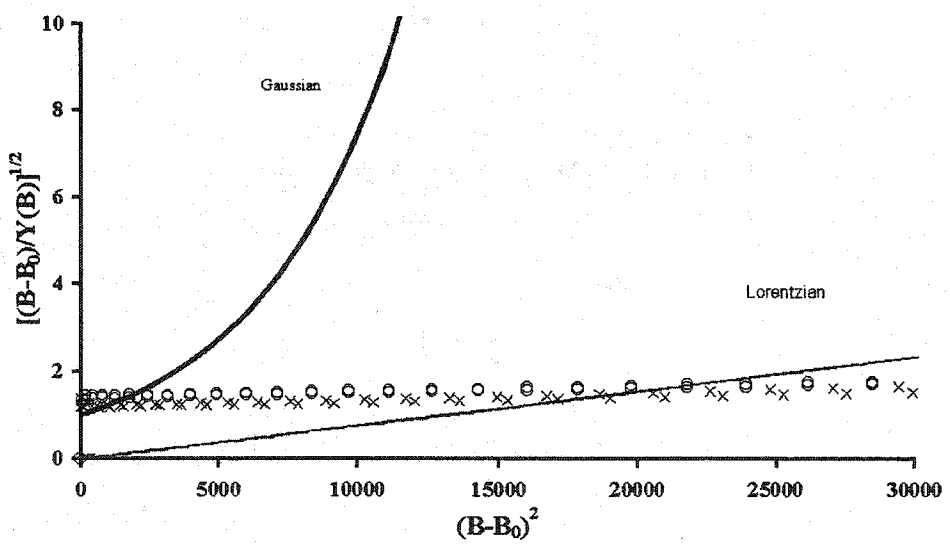


FIG. A2. Line shape analysis of doped crystal from BAE 15° from (3,1,6,) where the line width is narrowest. The g=3 resonance line is represented by x. The g=6 resonance line is represented by o. Lorentzian and Gaussian reference lines are labeled.

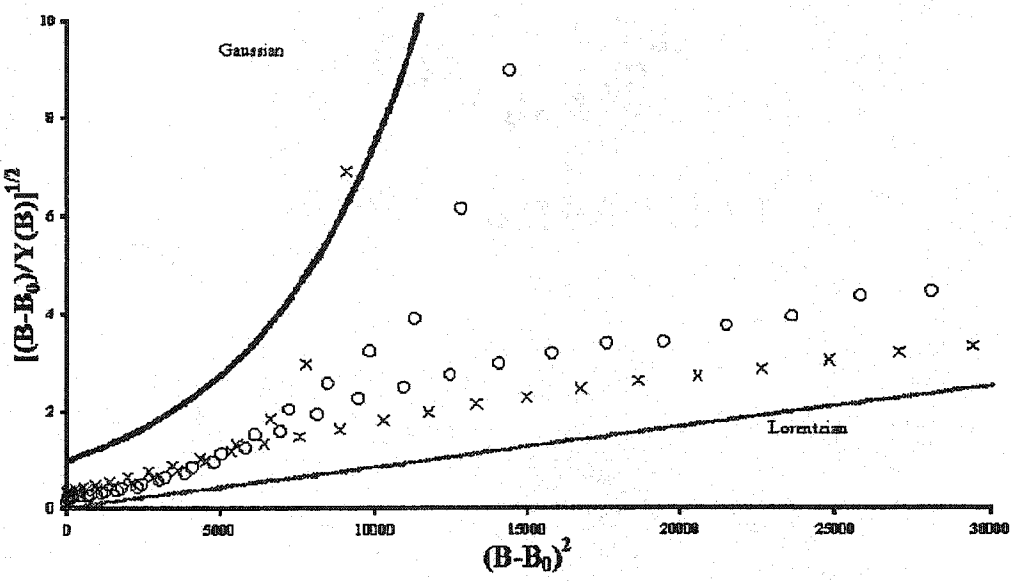


FIG. A3. Line shape analysis of doped crystal from BAE 120° from (3,1,6), where the line width is widest. The g=3 resonance line is represented by x. The g=6 resonance line is represented by o. Lorentzian and Gaussian reference lines are labeled.

# APPENDIX B

# CALIBRATION OF FLUORESCENCE INSTRUMENT

The fluorescence system was calibrated with a tungsten halogen lamp manufactured by Oriel Instruments and of known output. The lamp output may also be calculated at a specific wavelength by the equation

$$I = \lambda^{-5} * \exp(41.82596 - 4987.82311/\lambda) * (0.63615781 + (899.44990/\lambda) - (761258.64/\lambda^2) + (316259570/\lambda^3) - (65779226000/\lambda^4) + (5352141400000/\lambda^5)) \quad \text{(B1)}$$

The irradiance spectrum was normalized by integrating the spectrum over the wavelengths for which data were collected. Next we divided the spectra by the constant N.

$$\int I(\lambda) d\lambda = N \quad \text{(B2)}$$

Therefore, the integral of the irradiance is one. A trapezoid rule was to integrate the irradiance. Both the system calibration and expected irradiance data spectra must be normalized.

After the spectra are normalized, the expected irradiance at a wavelength is compared with the actual irradiance measured at that wavelength. The ratio of the expected to measured irradiance will then give a calibration constant of the fluorescence system for every wavelength used in the measurement.

**GRADUATE SCHOOL**
**UNIVERSITY OF ALABAMA AT BIRMINGHAM**
**DISSERTATION APPROVAL FORM**
**DOCTOR OF PHILOSOPHY**

**Name of Candidate** Melinda Johnson

**Graduate Program** Physics

**Title of Dissertation** Electron Paramagnetic Resonance and Optical Studies of CdGa2S4:Cr

**I certify that I have read this document and examined the student regarding its content. In my opinion, this dissertation conforms to acceptable standards of scholarly presentation and is adequate in scope and quality, and the attainments of this student are such that she may be recommended for the degree of Doctor of Philosophy.**

**Dissertation Committee:**

| Name | | Signature |
|---|---|---|
| Mary Ellen Zvanut | **, Chair** | |
| Robin D. Griffins | | |
| Joseph G. Harrison | | |
| Sergey B. Mirov | | |
| Hanno T. Tohver | | |
| Charles C. Watkins | | |

**Director of Graduate Program** Kumar Vohra

**Dean, UAB Graduate School**

**Date** 6/21/2003